2009

Mitigation of impact vibrations using impedance mismatch in cylindrical structures

Sachiko Sueki
University of Nevada Las Vegas

MITIGATION OF IMPACT VIBRATIONS USING IMPEDANCE MISMATCH IN CYLINDRICAL STRUCTURES

by

Sachiko Sueki

Bachelor of Science
Nihon University
1998

Master of Science
Arizona State University
2003

A dissertation submitted in partial fulfillment of
the requirements for the

Doctor of Philosophy in Civil and Environmental Engineering
Department of Civil and Environmental Engineering
Howard R. Hughes College of Engineering

Graduate College
University of Nevada, Las Vegas
December 2009

UNLV
UNIVERSITY OF NEVADA LAS VEGAS

THE GRADUATE COLLEGE

We recommend that the dissertation prepared under our supervision by

Sachiko Sueki

entitled

Mitigation of Impact Vibrations Using Impedance Mismatch in Cylindrical Structures

be accepted in partial fulfillment of the requirements for the degree of

Doctor of Philosophy in Engineering
Civil and Environmental Engineering

Samaan G. Ladkany, Committee Chair

Brendan J. O'Toole, Committee Co-Chair

Barbara Luke, Committee Member

Aly Said, Committee Member

Douglas Reynolds, Graduate Faculty Representative

Ronald Smith, Ph. D., Vice President for Research and Graduate Studies
and Dean of the Graduate College

December 2009

ABSTRACT

Mitigation of Impact Vibrations Using Impedance Mismatch in Cylindrical Structures

by

Sachiko Sueki

Dr. Samaan G. Ladkany, Examination Committee Chair
Professor of Civil and Environmental Department
University of Nevada, Las Vegas

Dr. Brendan J. O'Toole, Examination Committee Co-Chair
Associate Professor of Mechanical Department
University of Nevada, Las Vegas

The focus of this work is to study the phenomenon of material impedance mismatch to determine its effect on the mitigation of high frequency accelerations in projectile and long bar structures within linear ranges of materials. In this study, the acceleration responses of structures with various materials and material combinations were studied experimentally, numerically and by the Finite Element Analysis (FEA). Air-gun tests conducted by the US Army Research Laboratory were modeled using FEA to simulate the acceleration pulse and shock waves experienced by artillery components during a launch. After the prototype of projectile was selected, further studies were conducted experimentally and computationally using wave tracing techniques to understand the effect of impedance mismatch on the high frequency axial acceleration response to an impact loading.

Electronic devices for sensing, control and actuation have become standard components of "smart" structural systems to enhance their structural response adaptively and effectively. Such devices are being incorporated in military vehicles and weapon

systems. The reliability of these sensing devices under extreme loading conditions need much improvement since they are sensitive to high frequency vibrations.

Experimental results suggest that high frequency accelerations in layered cylindrical structures could be reduced compared either in frequency, magnitude or both to those in homogeneous cylinders if a reflected wave from the end of the projectile does not interfere with the applied impact force. Computational studies using FEA verified the experimental results of our interference hypothesis. Further, wave tracing results obtained using equations of wave propagations in a layered structure supported both computational and experimental results.

Our research was extended in two directions. One is the potential usage of new material types known as material foams in projectiles. Results show that mitigation can be obtained using metal foams if they do not get crushed completely under impact loads. Similarly, impedance mismatch concepts were considered using steel, concrete and wood for potential civil engineering applications. The results showed that the potential to reduce accelerations in hybrid building exists through the use of impedance mismatch if steel covers or joints are placed at the end of concrete beams.

TABLE OF CONTENTS

LIST OF FIGURES

LIST OF TABLES

LIST OF SYMBOLS

A	Cross-sectional area or surface area
c	Wave speed in one dimension
c_{Al}	Wave speed of Aluminum in one dimension
e	The base of the natural logarithm
E	Young's modulus
F_0	The maximum force
$F(t)$	Force function
j	The complex notation
k	The index for the computed set of discrete frequency components
K	Stiffness of a system
l	The index for the computational step of the Fourier transform
L	Length of a structure
m	Mass of a system
n	The time sample index or a number of periods
N	Number of samples being considered
p	The power term in the equation for the fast Fourier transform
t	Time
t_1	Impact duration
u	Displacement in x direction
W	$e^{-j2\pi/N}$, The term used in the equation for the Fast Fourier transform
x	Deformation
x_1	The grater of two amplitudes of a wave

x_n	The amplitude at n periods away from x_1
$\dot{x}$	Velocity
$\ddot{x}$	Acceleration
$X(n)$	The discrete set of time samples that defines the wave form to be transformed
$X(k)$	The set of Fourier coefficients obtained by the DFT of $x(n)$
Z	Impedance of a material
δ	The logarithmic decrement
ζ	The damping ratio
θ	Real number
μ	Poisson's ratio
ξ	Wave amplitude
ρ	Density of a material
σ_y	Yield strength
τ	Period
ω	Natural frequency
[]	Matrix notation
{}	Vector notation

ACKNOWLEDGEMENTS

I express my sincere gratitude to my advisor and committee chair, Dr. Samaan G. Ladkany, for his support and help throughout the course of my study. I would also like to extend sincere gratitude to Dr. Brendan J. O'Toole for serving as a committee co-chair and his kind support. I would also like to express my gratitude to my research committee members, Dr. Douglas Reynolds, Dr. Barbara Luke and Dr. Aly Said.

I sincerely acknowledge Army Research Laboratory for the financial support of this study through the Soldier's Future Force Electronics Reliability and Survivability Technology Program, cooperative agreement number DAAD19-03-2-0007. I would also like to equally acknowledge the civil and environmental engineering department and graduate college for supporting my study as a graduate assistant.

I greatly appreciate all the professors, especially Dr. Nader Ghafoori, who gave me constant and kind supports and encouragements. Finally, I would like to acknowledge all my friends who are always there to cheer me up. I would also like to extend my gratitude to administrative staffs and folks at UNLV for their kind help and support.

At the end, I would like to express my warm appreciation to my beloved parents, Masahiko and Mieko Sueki, and sister, Hiroko Iizuka for their encouragement, sacrifice, and unconditional support.

CHAPTER 1

INTRODUCTION

The research investigates a new concept to mitigate impact vibrations. In order to reduce propagation of vibrations from a structure, material impedance mismatch using different materials is introduced in a structure. In this research, the concept of mitigation of impact vibrations within linear ranges of materials is investigated using a projectile and a long bar as a structure. However, the outcome of this research can be applied to any structures to reduce propagation of vibrations.

1.1 Background and Outline

A word "projectile" refers to generic artillery which is distinguished from small arms. The projectile in this study is similar to the one used in the US Army Research Laboratory's air-gun tests to study suitability and survivability of future artilleries or smart projectile components. A smart projectile has electronic devices which guide, navigate and control trajectory. However, high accelerations induced during muzzle exit may be a source of electronic component failure in smart projectiles. As mentioned by Frost and Costello (2004) and Wilson et al. (2004), an electronic component of a smart projectile must withstand high-g loads during lunch. In general, electronic devices in a smart projectile must be small, economical and sustainable under high-g loading. In order to increase the impact tolerance of the electronic devices, the current accepted methods are generally a combination of stiffening and damping elements (Steinberg, 2000). However, as Veprik and Babitsky (2000) pointed out, the methods can not protect the electronic devices from high frequencies which typically contain resonant frequencies for

sensitive internal components. Therefore, it is important to find new ways to reduce high frequency vibrations from projectiles in order to protect the electronic devices.

Previously, Chen and Gurtin (1973) showed analytically that the amplitude of a wave is reduced at the interface of a layered composite material when a material of lower impedance is placed before higher impedance. Similarly, Solaroli et al. (2003) reported that the wave propagation attenuates over certain frequency bands using the periodic stiffness discontinuities in a relatively long shell. By periodically adding rings around the shell, the impedance changes occur as a result of periodic discontinuities in the stiffness. They pointed out that it is possible to obtain desired attenuation of wave propagation by periodically adjusting the impedance. These attenuations may be explained based on the wave reflection and transmission at a boundary. As described by Wasley (1973), Harrison and Nettleton (1997), and Blackstock (2000), when a wave passes through solid materials and meets interface of layers, a part of the wave is reflected from the boundary and the rest is transmitted through based on differences in impedance. If the impedance mismatch could be implemented in a smart projectile, it might help to reduce unwanted high frequency vibrations to protect its electronic devices. However, under what conditions the attenuation phenomenon works is not clearly known. Also, implementing the impedance mismatch in a projectile hasn't been studied so far. Therefore, in this research, the effects of the impedance mismatch are studied to reduce the accelerations.

At US Army Research Laboratory (ARL), air-gun tests have been used to simulate the acceleration pulse and shock waves experienced by artillery components during a launch. When a projectile exits from a muzzle, it experiences a high pressure change, which causes high-g force to the projectile. According to Bouland and Chowdhury (2005),

the air gun test simulates its desired acceleration pulse caused by high-g force during a muzzle exit through the impact of a projectile with an energy-absorbing mitigator. Electronic devices are mounted on the end of a projectile during the tests. In this study, finite element analysis of air-gun tests on a projectile is conducted to predict the acceleration response in a projectile. In addition, the design of experimental projectiles for the air-gun tests is also sought and discussed (Chapter 2). Furthermore, experiments are also conducted to verify the simulation results (Chapter 3). Since a facility for air-gun tests is not readily available, experiments are conducted by applying an impact at the end of a projectile. Therefore, more finite element analyses are conducted to verify the experimental results (Chapter 4). The results are examined from the point of view of reducing accelerations and discussed the phenomena by tracing waves in structures. These results are reported in Chapter 5. At the end of this study, a potential usage of new material type known as metal foams is examined to mitigate vibrations in a projectile. According to Radford et al. (2005), metal foams have superior energy absorbing capacity and have been considered in many applications for absorbing impacts and shocks. In Chapter 6, metal foams are examined to test their usefulness in reducing the vibration compared to solid materials using the same impedance mismatch concept. The concepts are also applied to commonly used building materials (steel, concrete and wood) and the results are reported in Chapter 7. Finally, the conclusions are given in Chapter 8.

1.2 Literature Review

1.2.1 Vibration Problem

Vibrations occur due to movement of objects during machine operations, collisions, and noise among others. The vibration may cause damage to mechanical systems and structures. For instance, excessive vibrations can cause undesirable motions, misalignments and disconnection of screws which lead to a faulty performance of a machine or device. Vibrations can also cause variable stresses which lead to damage or failure due to fatigue in structures such as cracking and wearing (Osiński, 1998). Fraser and Gureghian (1993) also pointed out that electronic devices, especially those having high performance capability, are sensitive to mechanical shocks and vibrations. Similarly, high accelerations induced during muzzle exit may be a source of electronic component failure in smart projectiles. The mitigation of such vibration problems is concerned in this study.

1.2.2 Vibration Damping

There are many ways to damp vibrations in structures such as active, passive and active-passive damping. Active control involves use of certain active elements such as speakers, actuators and microprocessors to produce out-of-phase signals to electronically cancel disturbances (Rao, 2003). All other methods that do not include a real-time active algorithm can be grouped under the passive control option. In semi-active methods, active controls are used to enhance damping properties of passive elements. Examples include controllable fluids such as Electro-Rheological (ER) and Magneto-Rheological (MR) fluids (Guan et al., 2006 and Song et al. 2006), and Active Constrained Layer Damping (ACLD) in which the traditional constraining layer is replaced with a smart

material (Rao, 2003). The passive damping, in general, is simple to implement and cost effective, requiring no on-line control (Tomlinson, 2001). Sometimes just changing the system's stiffness or mass to alter the resonance frequencies can reduce the unwanted vibrations as long as excitation frequencies do not change (Rao, 2003). However, in most cases, vibrations need to be dissipated by using damping materials such as viscoelastic materials (metals and polymers) and shape-memory alloys (SMA's). SMA's provide damping through the magnetomechanical mechanism where energy dissipation is caused basically by hysteresis motion of the magnetic domain boundaries (Chung, 2001). The use of material characteristics to control vibrations could be called material damping whereas the other type of category is system damping. System damping includes damping at the supports, boundaries, joints and interfaces.

1.2.3 Damping in Projectile

In order to implement a damping system to reduce vibrations in projectiles, the system must be simple and robust. Therefore, passive damping which is simple and does not require on-line control might be the best option among the three damping techniques for mitigation of acceleration in projectiles.

Previously, Solaroli et al. (2003) studied the attenuation of wave propagation in a relatively long shell where stiffness was changed periodically by adding rings around the shell. They concluded that, as a result of impedance changes generated by the periodic discontinuities in the stiffness, the wave propagation attenuates over certain frequency bands. Impedance is calculated based on material density and wave speed. Similarly, Toso and Baz (2004) studied wave propagation characteristics using periodicity, variable geometry and material properties in a long object. They concluded that the differences in

geometry significantly affect the wave propagation. In the same study, they also tested functionally graded materials (FGM) and suggested that they can be employed in applications where the geometry of a structure has a constraint in order to improve the attenuation of wave propagation. FGMs are used to produce components featuring engineered gradual transitions in microstructure and/or compositions. Li et al. (2001) also studied FGMs and layered materials. Their loading condition was such that the maximum pressure was comparable to the representative armor impact event and large enough to ensure the plastic deformation within the structure. The duration of the impact was chosen not to interfere with the effect of reflections from the other end of the surface. The computational results showed that the high tensile stress was caused by the interaction between wave reflections from the free end and the interface in the layered cylindrical specimen. They concluded that interfaces play crucial roles in dynamic problems, and sharp or discontinuous interfaces in layered composites may have strong values in structural design.

1.2.4 Layered Composite Materials

An advantage of layered composite materials is that materials can have low density with resistance to impacts, which can not be provided by monolithic materials. Reviews by Bert (1985) and Abrate (1991 and 1994) suggest that most of the research on the laminated composites is concentrated in the damage resistance and tolerance aspects or usage in lightweight armor to defeat projectiles. Therefore, to prevent failure of laminated composites, stress wave propagation in the composites has been the main consideration by a number of researchers.

Lundergan and Drumheller (1971) investigated stress wave propagation in a laminated composite, experimentally as well as analytically. Experiments were conducted by applying a square stress pulse into the composite made of thin layers of Epon 828 (epoxy resin) and stainless steel. Particle velocity was measured at the end of the composites and stress was calculated based on the velocity measurements. They concluded that the reduction of the peak amplitude of the stress is dependent on the width of the input stress pulse, but the bulk of the reduction of the stress is attributed to reflections of the stress wave at the extreme left and right boundaries of the composites.

Oved et al. (1978) studied early time wave propagation applying high stress in a layered composite made of thin layers of PMMA (acrylic glass) and copper. Their experiment showed a definite resonance behavior in stress wave propagation.

Chandra et al. (2002) studied a simplified multi-layered system analytically and concluded that the shock stress wave rise-time is significantly affected by the scattering characteristics resulting from an impedance mismatch in the interfaces. If there is a significant impedance mismatch, most of the energy in the wave is dissipated in internal reflections. Therefore, a stress wave increases gradually if a tensile release wave does not interrupt the wave. They also studied the effect of a number of layers. When a impedance mismatch is not significant, the rise time of a stress wave will be reduced as the number of layers increases.

Zhuang et al. (2003) conducted experiments in layered composites extensively to study effects of loading amplitude, interface impedance mismatch and the number of interfaces in stress wave propagation. The experiment had specimens made of two materials chosen from polycarbonate, aluminum alloy, stainless steel or glass. The

specimens were layered such that low impedance material came first in the path of the stress wave. The ratio of high to low impedances in specimens ranged from 7.5 to 23. They concluded that increasing the number of interfaces in a layered composite without changing the total mass increases in slope gradient and amplitudes of oscillations in a stress wave. They also reported that when impedance mismatch is high, the magnitude and duration of oscillations on the stress profiles increases. However if an applied impact is high (velocity of the impacted plate was 1050 m/s, which generate more than 3 GPa stress), the amplitudes of oscillations of the stress are about the same regardless of differences in impedance mismatch.

Tasdemirci et al. (2004) studied the stress distribution within layered composite materials and suggested that the stress distribution within samples was quite inhomogeneous and that the stresses were highest in the region of the layered composite interface. They also examined the use of rubber interlayer between the two major structural layers. The results showed that rubber reduces the maximum stress level in each layer and the stress distributions within each layer are rapidly varying in space.

Tasdemirci and Hall (2007) recently studied the effect of material combinations using ceramic, aluminum and copper which have significant differences in their impedances. Their experimental and computational work demonstrated that the impact on multi-layer materials can produce severe stress inhomogeneities at interfaces as well as serious stress gradients within the layers themselves. They pointed out that since different materials have different yield stresses, elastic moduli and strain hardening exponents, wave propagation in multi-layer materials is significantly more complex than in monolithic materials. They also pointed out that the plastic deformation of materials can significantly

affect their response to wave propagation, evantually leading to homogeneous stress distribution within the components.

As described by Wasley (1973), Harrison and Nettleton (1997), and Blackstock (2000), when a wave passes through solid materials and meets an interface of two layers, a part of the wave is reflected from the boundary and the rest is transmitted through, based on differences in impedance. Basic analytical expression of stress wave propagation was described simply based on this phenomenon. For instance, Beddoe (1965) mathematically expressed stress wave propagation in a rod having different cross-sectional areas in terms of simple reflection and transmission coefficients, and the source stress wave. Similary, Chiu (1970) solved stress wave propagation in an elastic bar with discontinuities using finite-difference approximations. These stress wave propagation expressions did not have the effect of wave dispersion and damping. Barker (1971) included a dispersive effect in his theoretical model of a plate laminate composite as a direct analogy with viscosity effect. His results showed that the model predicts the overall transient wave profile well but the oscillatory nature of the wave profile is missing. Ting and Mukunoki (1979) pointed out that the models developed so far are limited only to the case of long wavelength conditions such that average wave properties are meaningful. By replacing a layered medium by an equivalent-linear homogeneous viscoelastic medium, they could predict the transient response at any point in the layered medium. They further studied their theory to extend to a finite layered medium (Mukunoki and Ting, 1980). Recently, Han and Sun (2001) studied wave front decay and spatial attenuation based on viscoelastic analogy of a periodically layered elastic medium. They showed that a higher

impedance mismatch between the two constituent materials leads to a higher spatial attenuation of waves trailing the wave front and to a larger wave front decay.

Chen and Gurtin (1973) analytically studied the one-dimensional stress wave in terms of acceleration for a layered composite material. They pointed out that an acceleration wave of the laminated elastic composite behaves like a viscoelastic material at the interfaces. When lower impedance is placed before the material of higher impedance, amplitude of the wave reduces at the interface. They also argued that viscosity of the material is of little importance since most of the relaxation is due to the laminations when considering the layered composite material.

There is almost no literature on acceleration responses in layered composites. However, from the past research in layered composites and as described by Newton's second law, it is clear that layered composites whose interfaces have high impedance mismatch change their acceleration response.

1.3 Theoretical Background

1.3.1 Wave Propagation

Wave propagation needs to be considered only under certain loading conditions. Depending on loading rate, the response of elastic solids subjected to an applied force will be different. For instance, inertial effects are excluded when a force is applied slowly to attain equilibrium of the stress field throughout the entire medium. However, inertial effects must be considered when a force of sufficient amplitude is applied for very short periods of time, or is changing rapidly. Inertia forces are usually considered when strain rate are more than the order of 1 s^{-1} (Wasley, 1973).

Wave propagation occurs when waves travel through a medium in any way. When a medium is affected by a local excitation such as rapid impulsive loading, the local excitation of a medium is not instantaneously detected at a distance from the region of the excitation. It takes time for a disturbance to propagate from its source to the next position. This phenomenon of propagation of disturbances is usually referred as wave propagation (Arduino et al., 2000).

1.3.2 Wave Speed

These categories of waves are defined based on the direction of movement of individual particles of the medium relative to the traveling direction of the waves: transverse, longitudinal and surface waves. A transverse wave is a wave in which particles of the medium move in a direction perpendicular to the direction of wave propagation. A longitudinal wave is a wave in which particles of the medium move in a direction parallel to the main wave movement. A surface wave propagates along the interface between different media. How fast a wave travels depends on the mechanical properties of the medium and expressed as a wave speed, c.

When an impulsive force is applied at the end of an elastic prismatic bar, stress waves travel through the bar. If the pressure induced is less than the material yielding strength, the material exhibits elastic behavior. Under this condition, the speed of longitudinal waves in an elastic prismatic bar, c, depends on the elastic restoring force and inertia. In one dimensional case, the speed of waves can be calculated by the following equation;

$$c = \sqrt{E/\rho} \qquad \text{Equation 1.1}$$

Table 1.1 Elastic wave speeds for several materials (after Stronge, 2000)

Material	ρ (kg/m^3)	E (kN/mm^2)	μ	c (m/s)
Aluminum alloy	2,700	70	0.34	5092
Brass	8,300	95	0.35	3383
Copper	8,500	114		3662
Lead	11,300	17.5	0.45	1244
Steel	7,800	210	0.31	5189
Glass	1,870	55		5300
Granite	2,700		0.22	3120
Limestone	2,600		0.33	4920
Perspex			0.4	2260

where, E is young's modulus and ρ is density of the elastic prismatic bar. This equation is derived from the axial equation of motion and Hooke's law. Elastic wave speeds for several materials are shown in Table 1.1 (Stronge, 2000).

1.3.3 Wave Reflection and Transmission

As a longitudinal wave pulse approaches a fixed end, the velocity at the fixed end must vanish while the stress is doubled. Therefore, the reflected wave pulse travels with the same speed and amplitude as the incident wave, but with the same sign. On the other hand, as a wave pulse approaches a free end, the stress normal to the surface must be zero. Therefore, the reflected wave pulse propagates with the same speed and amplitude as the incident wave, and with the opposite sign.

When a wave encounters a boundary which is neither fixed nor free but somewhere in between, part of the wave is reflected from the boundary and part of the wave is transmitted across the boundary. The exact behavior of reflection and transmission

depends on the material properties on both sides of the boundary. One important property is the characteristic impedance of the material. The characteristic impedance of a material, Z, is the product of mass density, ρ, and wave speed, c; $Z = \rho c = \sqrt{\rho E}$ per unit area. If a wave with amplitude ξ_1 in medium 1 encounters a boundary with medium 2, the amplitudes of the reflected and transmitted waves are respectively determined by following equations (Blackstock, 2000).

$$\xi_r = \frac{Z_2 - Z_1}{Z_1 + Z_2}\xi_1 \qquad \text{Equation 1.2}$$

$$\xi_t = \frac{2Z_2}{Z_1 + Z_2}\xi_1 \qquad \text{Equation 1.3}$$

However, if there is also a change in cross-sectional area, A, at a boundary in addition to material changes, impedance is calculated by $Z = \rho c A = \sqrt{\rho E}\, A$ (Harrison and Nettleton, 1997). Then, the amplitudes of the reflected and transmitted waves are determined using same equations described above with this impedance. Note that as Kolsky (1963) pointed out the above theory is based on an assumption that the wave travels in a medium without dispersion.

1.3.4 Fast Fourier Transforms

Analysis using the Fourier transforms is a mathematical technique used to obtain both the frequency-domain magnitude and the phase from a time-domain waveform. The classic mathematical approach to Fourier analysis cannot be used if the waveform cannot be mathematically formulated. However, a random waveform such as the one obtained from an impulse can be sampled and digitized using a data acquisition system such as an oscilloscope. In this case, the discrete Fourier transform (DFT) can be used to transform the digitized waveform. Using the complex form of the Fourier series to describe the

randomly obtained and digitized wave form in a mathematical formulation, keeping in mind Euler's principal equation,

$$e^{\pm j\theta} = \cos\theta \pm j\sin\theta \qquad \text{Equation 1.4}$$

the DFT can be expressed as the following equation (Ramirez, 1985).

$$X(k) = \sum_{n=0}^{N-1} x(n) e^{-j2\pi kn/N} \qquad \text{Equation 1.5}$$

This equation is used to transform a time series of samples to a series of frequency-domain samples. The inverse DFT allows to transform a series of frequency-domain samples computed by the DFT back to a series of time-domain samples. The inverse DFT is expressed as following equation.

$$x(n) = \frac{1}{N} \sum_{k=0}^{N-1} X(k) e^{j2\pi kn/N} \qquad \text{Equation 1.6}$$

The variables used in DFT and inverse DFT equations have the following definitions:

N = number of samples being considered,

n = 0, 1, 2, …, N-1 (the time sample index),

k = 0, 1, 2, …, N-1 (the index for the computed set of discrete frequency components),

$x(n)$ = the discrete set of time samples that defines the waveform to be transformed,

$X(k)$ = the set of Fourier coefficients obtained by the DFT of $x(n)$,

e = the base of the natural logarithm,

$j = \sqrt{-1}$ (the symbol of complex notation),

θ = any real number.

Computing the DFT is essentially a repetitive task as expressed in the DFT series equation. A commonly used algorithm of DFT is the fast Fourier transform (FFT). The

major advantage of the FFT is the speed with which it analyzes large numbers of waveform samples. If the DFT is computed without using the FFT, N^2 operations are needed to transform N samples into the frequency-domain data while the FFT needs only $N \log_2 N$ operations. The FFT uses the matrix factorization process which introduces zeros into the factored matrices. If we let

$$W = e^{-j2\pi/N} \qquad \text{Equation 1.7}$$

Equation 1.2 can be rewritten as

$$X(k) = \sum_{n=0}^{N-1} x(n) W^{kn} \qquad \text{Equation 1.8}$$

or in matrix form

$$\{X(k)\} = [W^{kn}]\{x(n)\} \qquad \text{Equation 1.9}$$

By applying the matrix factorization process, Equation 1.6 can be calculated by following two equations.

$$\begin{aligned} x_l(n) &= x_{l-1}(n) + W^p x_{l-1}(n + N/2^l) \\ x_l\left(n + N/2^l\right) &= x_{l-1}(n) - W^p x_{l-1}(n + N/2^l) \end{aligned} \qquad \text{Equation 1.10}$$

where,

$l = 1, 2, \ldots, \log_2 N$,

p is determined by following steps:

(i) Write index n in binary form with γ bits.

(ii) Slide the binary number γ-l bits to the right and fill in the newly opened bit position on the left with zeros.

(iii) Reverse the order of the bits. This bit-reversed number is the term p.

Note that when l is equal to 1, $x_0(n)$ is the discrete set of time samples, $x(n)$. When l reaches to the final step, $\log_2 N$, a time series of samples, $x(n)$, are transformed to a series of frequency-domain samples, $X(k)$. Detailed description of the FFT algorithm can be found in Brigham (1974).

In this research, time-domain samples are generally shown as time in seconds versus acceleration in m/s^2. By using FFT, the time-domain samples are transferred to frequency-domain, magnitude versus frequency in Hz. The magnitude in FFT results has same unit as time-domain samples, m/s^2.

Bibliography

Abrate, S. (1991). Impact on laminated composites materials, *Applied Mechanics Reviews*, 44, 155-190.

Abrate, S. (1994). Impact on laminated composites: Recent advances. *Applied Mechanics Reviews*, 47, 517-544.

Arduino, P., Miller, G. and Ogunrinde, A. (2000). An Introduction to the theory of wave propagation in layer media, basic concepts. Retrieved at April 16, 2008 from http://gmiller.ce.washington.edu/DrLayer/theory/T-Basic-Concepts.html.

Barker, L. M. (1971). A model for stress wave propagation in composite materials. *Journal of Composite Materials*, 5, 140-162.

Beddoe, B. (1965). Propagation of elastic stress waves in a necked rod. *Journal of Sound and Vibration*, 2, 150-166.

Bert, C. W. (1985). Research on dynamic behavior of composite and sandwich plates – IV. *The Shock and Vibration Digest*, 17, 3-15.

Blackstock, D. T. (2000). *Fundamentals of physical acoustics*. New York: John Wiley & Sons, Inc.

Bouland, A. and Chowdhury, M. R. (2005). Analytical Simulation and Verification of Air Gun Impact Testing. *Army Research Laboratory*, ARL-TR-3559.

Brigham, E. O. (1974). *The fast Fourier transform*. Englewood Cliffs: Prentice-Hall, Inc.

Chandra, N., Chen, X., and Rajendra, A. M. (2002). The effect of material heterogeneity on the shock response of layered systems in plate impact tests. *Journal of Composites, Technology and Research*, 24, 232-238.

Chen, P. J. and Gurtin, M. E. (1973). On the propagation of one-dimensional acceleration waves in laminated composites. *Journal of Applied Mechanics*, 40, 1055-1060.

Chiu, S. S. (1970). Difference method for multiple reflection of elastic stress waves. *Journal of Computational Physics*, 6, 17-28.

Chung, D. D. L. (2001). Review: Materials for vibration damping. *Journal of Materials Science*, 36, 5733-5737.

Fraser, J. W. and Gureghian, R. S. (1993). Controlling shock and vibration in electronic products. *Mechanical Engineering*, 115, 82-84.

Frost, G. W. and Costello, M. F. (2004). Control authority of a projectile equipped with an internal unbalanced part. *Army Research Laboratory*, ARL-CR-555.

Guan, X. C., Dong, X., Guo, P. and Ou, J. P. (2006). Vibration control and magnetostrictive composite materials. *Proceedings of SPIE – the international society for optical engineering*, 6169, 61690Q1-61690Q9.

Han, C. and Sun, C. T. (2001). Attenuation of stress wave propagation in periodically layered elastic media. *Journal of Sound and Vibration*, 243, 747-761.

Harrison, H. R. and Nettleton, T. (1997). *Advanced engineering dynamics*. New York: John Wiley & Sons, Inc.

Kolsky, H. (1963). *Stress waves in solids*. New York: Dover Publications, Inc.

Li, Y., Ramesh, K. T. and Chin, E. S. C. (2001). Dynamic characterization of layered and graded structures under impulsive loading. *International Journal of Solids and Structures*, 38, 6045-6061.

Lundergan, C. D. and Drumheller, D. S. (1971). Propagation of stress waves in a laminated plate composite. *Journal of Applied Physics*, 42, 669-675.

Mukunoki, I. and Ting, T. C. T. (1980). Transient wave propagation normal to the layering of a finite layered medium. *International Journal of Solids and Structures*, 16, 239-251.

Osiński, Z. (Eds.). (1998). *Damping of vibrations*. Rotterdam, Netherlands: A. A. Balkema.

Oved, Y., Luttwak, G. E. and Rosenberg, Z. (1978). Shock wave propagation in layered composites. *Journal of Composite Materials*, 12, 84-96.

Radford, D. D., Deshpande, V. S. and Fleck, N. A. (2005). The use of metal foam projectiles to simulate shock loading on a structure. *International Journal of Impact Engineering*, 31, 1152-1171.

Ramirez, R. W. (1985). *The FFT, fundamentals and concepts*. Englewood Cliffs, New Jersey: Tektronix, Inc.

Rao, M. D. (2003). Recent applications of viscoelastic damping for noise control in automobiles and commercial airplanes. *Journal of Sound and Vibration*, 262, 457-474.

Solaroli, G., Gu, Z., Baz, A. and Ruzzene, M. (2003). Wave propagation in periodic stiffened shells: spectral finite element modeling and experiments. *Journal of Vibration and Control*, 9, 1057-1081.

Song, G., Sethi, V. and Li, H. N. (2006). Vibration control of civil structures using piezoceramic smart materials: A review. *Engineering Structures*, 28, 1513-1524.

Steinberg, D. S. (2000). *Vibration analysis for electronic equipment* (3rd ed.). New York: John Wiley & Sons, Inc.

Stronge, W. J. (2000). *Impact Mechanics*. New York: Cambridge University Press.

Tasdemirci, A., Hall, I. W. and Gama, B. A. (2004). Stress wave propagation effects in two- and three-layered composite materials. *Journal of Composite Materials*, 38, 995-1009.

Tasdemirci, A. and Hall, I. W. (2007). The effects of plastic deformation on stress wave propagation in multi-layer materials. *International Journal of Impact Engineering*, 34, 1797-1813.

Ting, T. C. T. and Mukunoki, I. (1979). A theory of viscoelastic analogy for wave propagation normal to the layering of a layered medium. *Journal of Applied Mechanics*, 46, 329-336.

Tomlinson, G. R. (2001). SD2000 state of the art review: damping. In D. J. Ewins & D. J. Inman (Eds.), *Structural dynamics @ 2000: current status and future directions* (pp. 369-388). England: Research Studies Press LTD.

Toso, M. and Baz, A. (2004). Wave propagation in periodic shells with tapered wall thickness and changing material properties. *Shock and Vibration*, 11, 411-432.

Veprik, A. M. and Babitsky, V. I. (2000). Vibration protection of sensitive electronic equipment from harsh harmonic vibration. *Journal of Sound and Vibration*, 238, 19-30.

Wasley, R. J. (1973). *Stress wave propagation in solids, an introduction*. New York: Marcel Dekker, Inc.

Wilson, M. J., Hall, R. A. and Ilg, M. (2004). ONBORD (On-board Navigation of Ballistic ORDnance): Gun-launched munitions flight controller. *Army Research Laboratory*, ARL-TR-3210.

Zhuang, S., Ravichandran, G. and Grady, D. E. (2003). An experimental investigation of shock wave propagation in periodically layered composites. *Journal of the Mechanics and Physics of Solids*, 51, 245-265.

CHAPTER 2

FINITE ELEMENT ANALYSIS OF AIR-GUN TEST

In order to study the mitigation of accelerations in a projectile using the impedance mismatch concept, simulation studies were conducted by modeling the U.S. Army Research Laboratory air-gun tests (Chowdhury and Tabiei, 2003 and Bouland and Chowdhury, 2005). These tests have been used to simulate the acceleration pulse and shock waves experienced by artillery components during a launch. The test makes it possible to investigate the survivability of individual artillery components for less than the cost of an actual field test. The air-gun test achieves its desired acceleration pulse through the impact of a projectile with an energy-absorbing mitigator (an aluminum honeycomb mitigator). The projectile is propelled by compressed gas into the aluminum honeycomb mitigator which crushes to absorb the energy of the impact (Figure 2.1). The remaining energy is then transferred to a large momentum exchange mass (MEM) which is displaced by the inertial force of the system. This deceleration process gives the desired acceleration pulse without breaking the projectile. The projectile is cylindrical with a hollow part, a solid part (plate) where the recording equipment is placed and a box at the end where the sensitive electronic devices are placed. Detailed description of the

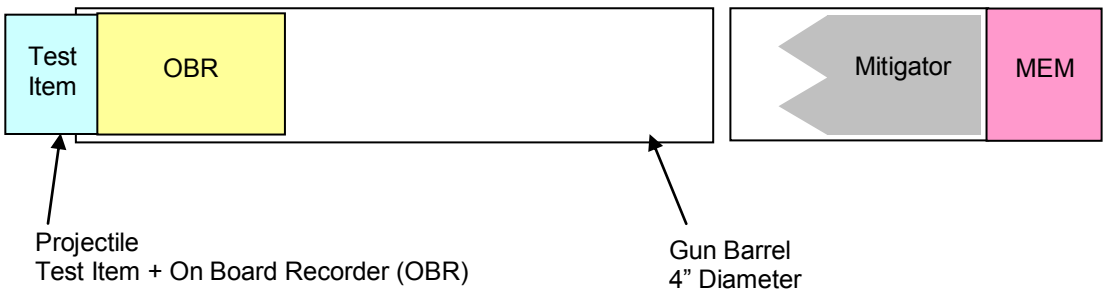

Figure 2.1 Schematic setup of the air-gun test (after Bouland and Chowdhury, 2005).

air-gun tests can be found in Chowdhury and Tabiei (2003) and Bouland and Chowdhury (2005).

In our research, two software programs, LS-DYNA (LSTC, 2006) and UM-GUI (Baz, 2006) are used to simulate the air-gun tests. Extensive study of finite element models of air-gun tests using LS-DYNA has been reported by Chowdhury and Tabiei (2003) and Karpanan (2005). Therefore, the finite element models in this research were constructed based on the previous results and used to configure a projectile which reduces the impact acceleration at the end of the projectile where mitigation is desired. UM-GUI is a specialized explicit finite element code based on a damped spring mass system used to calculate the dynamic response of the projectile upon impact with the honeycomb mitigator. The impact force is calculated based on the impact speed of the projectile and the experimental strain rate results of the honeycomb mitigator (Bouland and Chowdhury, 2005). The code is simplified in that its projectile model has a limited number of finite elements and does not contain a model of the honeycomb mitigator or the MEM.

2.1 LS-DYNA Model Setup

2.1.1 Geometry and Mesh Generation of the Air-Gun Test Model

As shown in Figure 2.2, a projectile, a honeycomb mitigator and a momentum exchange mass (MEM) are modeled using refined finite meshes with the aid of Altair HyperMesh software (Altair, 2004). A total of 32,792 elements were used to model the system, consisting of 14,496 elements for the projectile, 18,040 for the honeycomb mitigator and 256 for the MEM. All the components are meshed using an eight-node solid hexahedron element except for the tip of the honeycomb where a six-node

pentahedron is used. In the computational process, one-point Gaussian quadrature is used to carry out the volume integration and constant stress solid element type is used (LSTC, 2003 and Hallquist, 2006).

2.1.2 Defining Material Properties

The projectiles in our study may be made of aluminum or combinations of aluminum

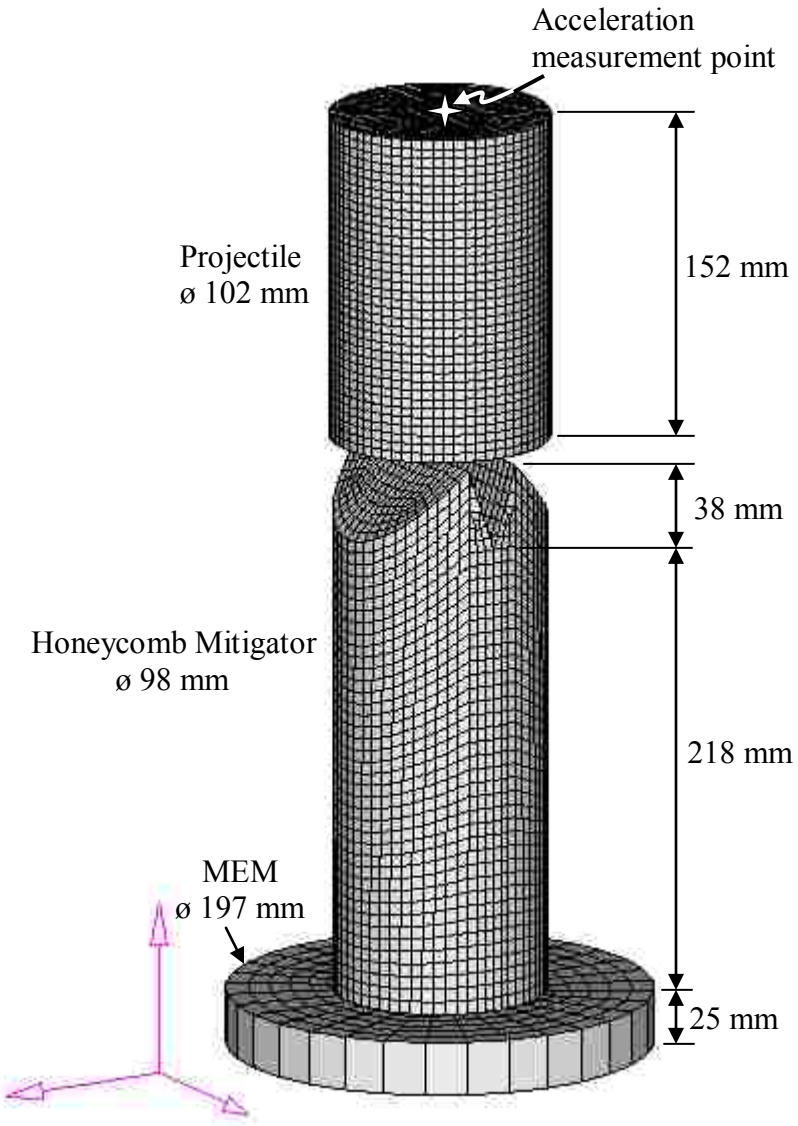

Figure 2.2 The finite element model of air-gun test.

Table 2.1 Material Properties

		Density	Young's Modulus	Poisson's Ratio	Yield Strength	Wave Speed	Impedance
		ρ (kg/m^3)	E (GPa)	μ	σ_y (MPa)	c (m/s)	Z (kg/m^{2}s)
Projectile	Aluminum	2700.0	70.00	0.33	250.00	5091.8	1.37E+07
	Polycarbonate	1200.0	2.30	0.35	62.00	1384.4	1.66E+06
Mitigator	Al Honeycomb	608.7	11.38	0.00	N/A	N/A	N/A
MEM	Steel	41506.4[a]	210.00	0.30	N/A	N/A	N/A

[a]Value is modified in order to make MEM same weight as the reported experiment

and polycarbonate. The honeycomb mitigator is made of aluminum. The momentum exchange mass is made of steel. These materials are described below. Table 2.1 summarizes material properties used in the model.

2.1.2.1 Projectile

The projectile used in the simulation conducted by Bouland and Chowdhury (2005) was made of steel and aluminum. Szymanski (2004) used a projectile made of aluminum to conduct the air gun tests. In this dissertation, aluminum was selected as the baseline material. Polycarbonate is selected as the second material based on its significantly low impedance compared to aluminum, its strength, availability, ease of fabrication, and low cost. Both aluminum and polycarbonate are defined in the finite element models using *MAT_PLASTIC_KINEMATIC in LS-DYNA excluding strain-rate effects. Note that the projectile under an air-gun test must stay unbroken and intact and therefore the materials should be in elastic ranges.

2.1.2.2 Honeycomb Mitigator

Honeycomb material could be defined using several different material cards in LS-DYNA solver. Some of the cards such as *MAT_HONEYCOMB and *MAT_MODIFIED_HONEYCOMB require anisotropic material properties in order to

model real anisotropic behavior (LSTC, 2003). Orthotropic material cards are also available such as *MAT_CRUSHABLE_FOAM and *MAT_MODIFIED_CRUSHABLE_FOAM. Chowdhury and Tabiei (2003) modeled an aluminum honeycomb mitigator using two material cards, *MAT_MODIFIED_HONEYCOMB and * MAT_CRUSHBLE_FOAM in LS-DYNA, and concluded that both material models led to reasonable predictions. They also mentioned that the strain rate sensitivity must be accounted for in these simulations. Wu and Jiang (1997) reported that the average dynamic crush strength was found to be of the range 1.33 – 1.74 of that obtained under quasi-static loading conditions. Also, they found that the crush strength was proportional to the initial striking velocity of the projectile. Karpanan (2005) modeled the honeycomb mitigator using the LS-DYNA solver cards, *MAT_CRUSHABLE_FOAM and *MAT_MODIFIED_CRUSHABLE_FOAM and concluded that *MAT_MODIFED_CRUSHABLE_FOAM, which includes the strain rate effects, matches the reported experimental values fairly well.

In this research, a honeycomb material is modeled using *MAT_MODIFIED_CRUSHABLE_FOAM as isotropic material including strain rate effects. There are two reasons this material card is selected. First the anisotropic material properties of a honeycomb mitigator are not available. The second, this research is focused only on axial movement of accelerations. Therefore, the isotropic material card with strain rate effects is chosen.

A stress-strain curve of the honeycomb mitigator is constructed based on Lu and Hinnerichs (2001) test data as shown in Figure 2.3. They conducted the compressive test under quasi-static and high loading rate (14 ft/s) which translated into strain rate of 112 s^{-}

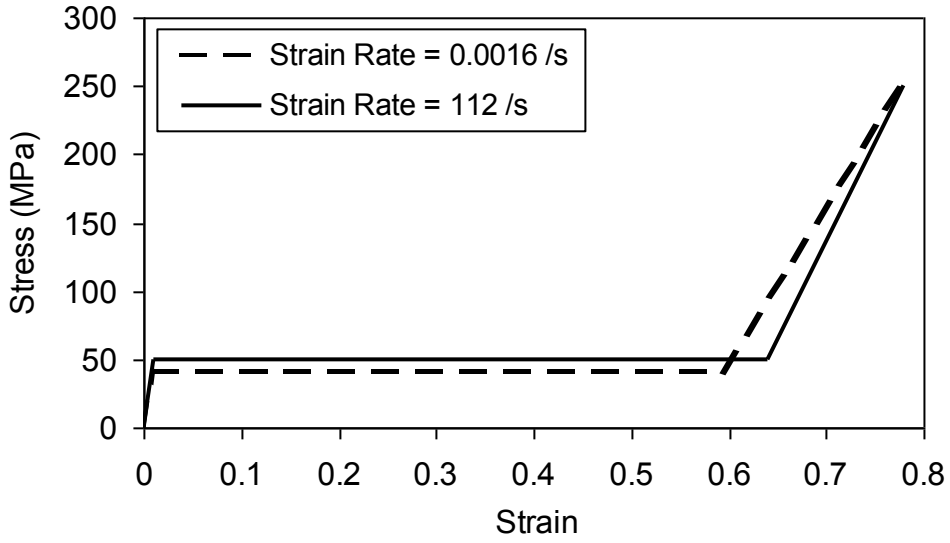

Figure 2.3 Stress-strain curve of aluminum honeycomb used for the air-gun model.

[1]. The honeycomb that was used for testing was manufactured by Hexcel (CR-8-LC-1/8-5052-006-R2) and its density was 608.7 kg/m^3 with the theoretical "full compaction" volumetric strain of 0.78. The crush strengths in axial direction under Quasi-static and high rate were reported as 40.54 and 49.44 MPa with crush efficiencies of 59.2 and 63.9 %, respectively. Young's modulus of the honeycomb reported by Hexcel (1999) was 11.38 GPa.

2.1.2.3 Momentum Exchange Mass

The momentum exchange mass is made of steel and used as a secondary energy-absorbing device in order to take momentum away from the crushed mitigator. Therefore, momentum exchange mass is defined using *MAT_RIGID. The density of the steel is modified in the finite element analysis in order that the momentum exchange mass has the same weight and mass as that used by Chowdhury and Tabiei (2003) in their

experiments. Note that the exact shape of the momentum exchange mass is not a critical factor for the simulation.

2.1.3 Projectile Configurations

As mentioned earlier, two material types, aluminum and polycarbonate, are used to model projectiles. In the first case, three types of material order combinations are considered in our study. The first type of a projectile is made of aluminum only and named as 'All Al' (Figure 2.4 and Figure 2.5a). The second type of the projectile which is named as 'Al & Poly' is made of aluminum and polycarbonate in alternate layout and aluminum at both ends (Figure 2.5b). The third type of a projectile is also made of aluminum and polycarbonate in alternate layout but with polycarbonate ends. The third type of the projectile is named as 'Poly & Al' (Figure 2.5c). Overall dimensions of the projectiles are kept the same. Note that all projectiles have different weights as shown in Table 2.2.

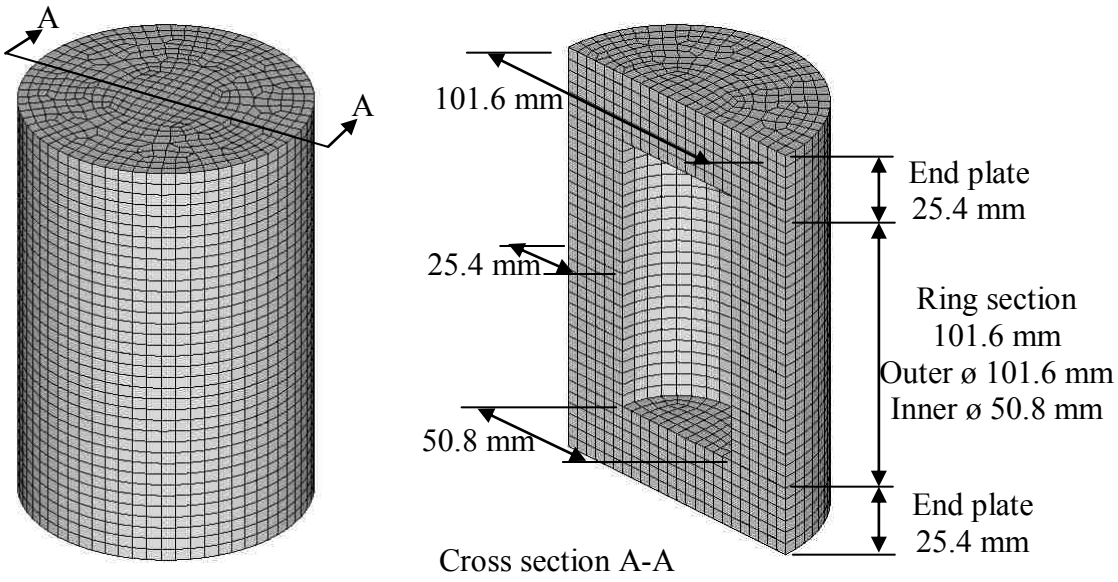

Figure 2.4 Dimensions of a projectile.

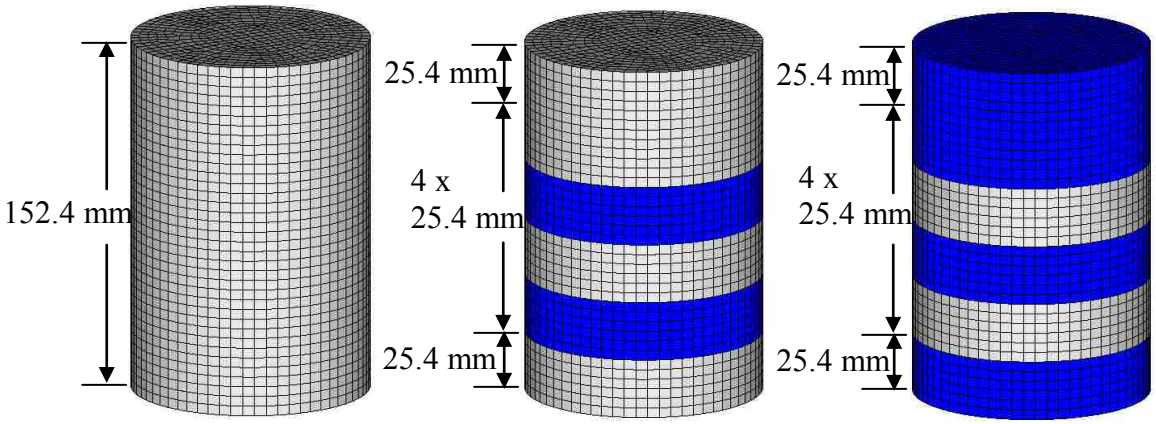

(a) All Al (b) Al & Poly (c) Poly & Al

Figure 2.5 Three kinds of a projectile model for the effect of layering order, gray and blue colors represent aluminum and polycarbonate sections, respectively.

Table 2.2 Weight of the projectiles

	All Al	Al & Poly	Poly & Al
Total Weight (kg)	2.78	2.31	1.70

In the second case, the effect of the number of interfaces is considered. As shown in Figure 2.6, one, two and four layers of polycrbonate rings are inserted in a projectile. The projectile with one layer of polycarbonate is named as 'Al & 1 Poly', two layers is named as 'Al & 2 Poly' and four layers is named as 'Al & 4 Poly'. In order to keep other conditions constant, thickness of each ring is adjusted and overall dimension and weight of projectiles are kept the same. Note that Figures 2.5 (b) and 2.6 (b) with two different names are the same projectile ('Al & Poly' and 'Al & 2 Poly').

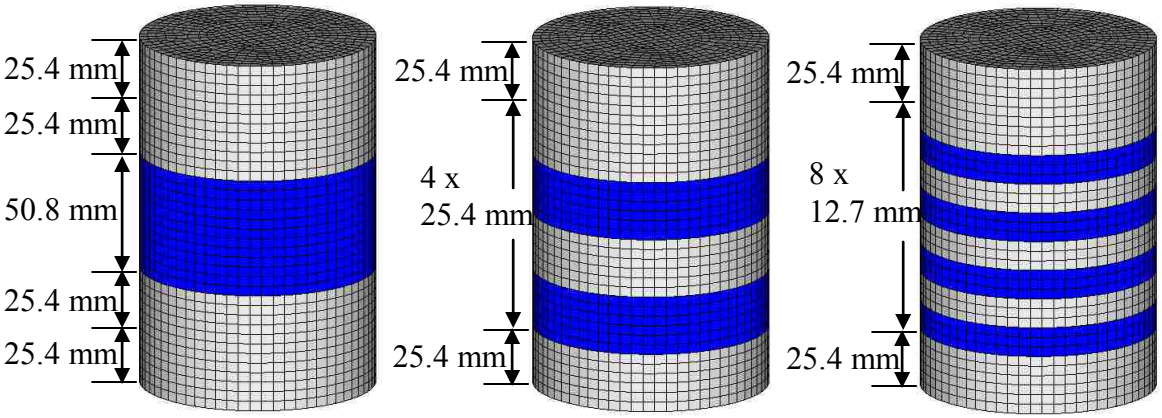

(a) Al & 1 Poly (b) Al & 2 Poly (c) Al & 4 Poly

Figure 2.6 Three kinds of a projectile model for the effect of number of layers, dark and light color represent polycarbonate and aluminum sections, respectively.

2.1.4 Miscellaneous

In all the models, a projectile impact velocity of 80 m/s is used and defined as an initial velocity of the projectile. The impact velocity is chosen based on the experimental results shown in Chowdhury and Tabiei (2003).

Contact surfaces between the projectile, the aluminum honeycomb and the MEM are defined as compression-only surfaces. There is no contact surface or elements defined between aluminum and polycarbonate parts of a projectile. Nodes between two different materials are shared in the finite element model.

2.2 UM-GUI Model Setup

Since the UM-GUI model is a specialized code to calculate the dynamic response of a projectile in the air-gun test, user input options are limited. The user can define dimensions, materials, impact velocities and a maximum frequency response to be

calculated. Figure 2.7 shows the defined axisymmetric model of the projectile. Dimensions and materials of the projectile are set to the same values as in the LS-DYNA model. Properties and dimensions of the honeycomb mitigator and MEM are internally defined to the same values as in LS-DYNA model. The detailed descriptions of each component of the air-gun test are found in the previous section. The projectile configurations used in UM-GUI model are the three types discussed in the first case previously (Figure 2.5).

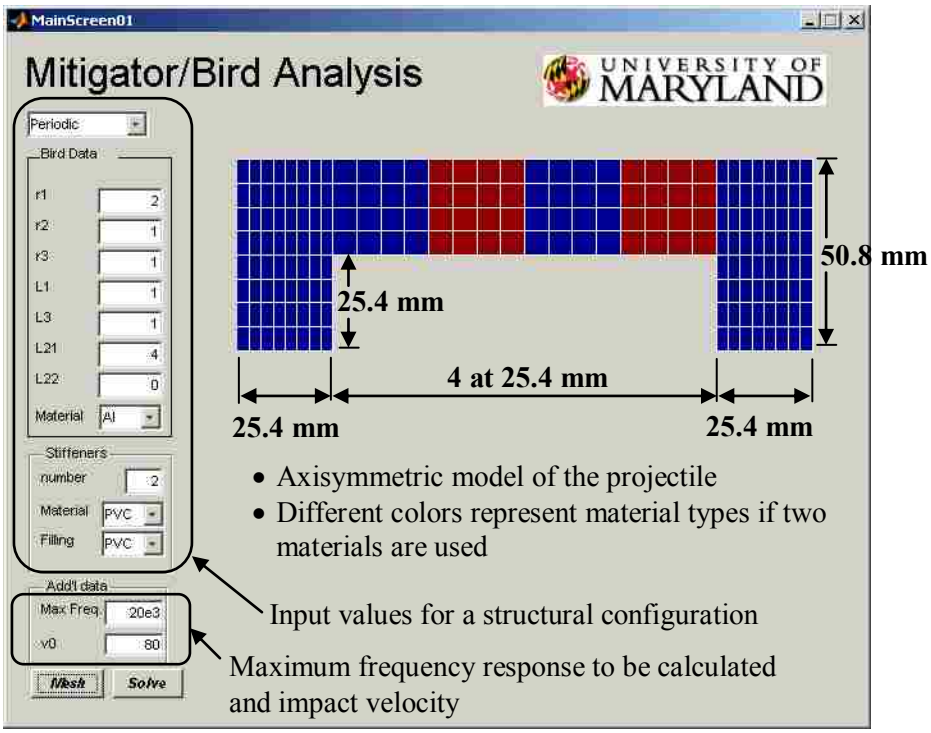

Figure 2.7 Modeled projectile in UM-GUI model.

2.3 Results

2.3.1 Results of LS-DYNA Model

2.3.1.1 Effect of Layering Order

Figure 2.8 shows the force curves that three projectiles ('All Al', 'Al & Poly' and 'Poly & Al' projectiles) experienced by colliding with the honeycomb mitigator with 80 km/sec impact velocity. 'All Al' is the projectile made of aluminum only, and 'Al & Poly' is the projectile made of aluminum and polycarbonate in alternate order and aluminum at both ends. 'Poly & Al' is the projectile also made of aluminum and polycarbonate in alternate order but with polycarbonate ends. As shown in Table 2.2, each projectile has a different weight therefore the force experienced by each projectile is also different.

Figure 2.9 shows the time domain response results of the ar-gun models of 'All Al',

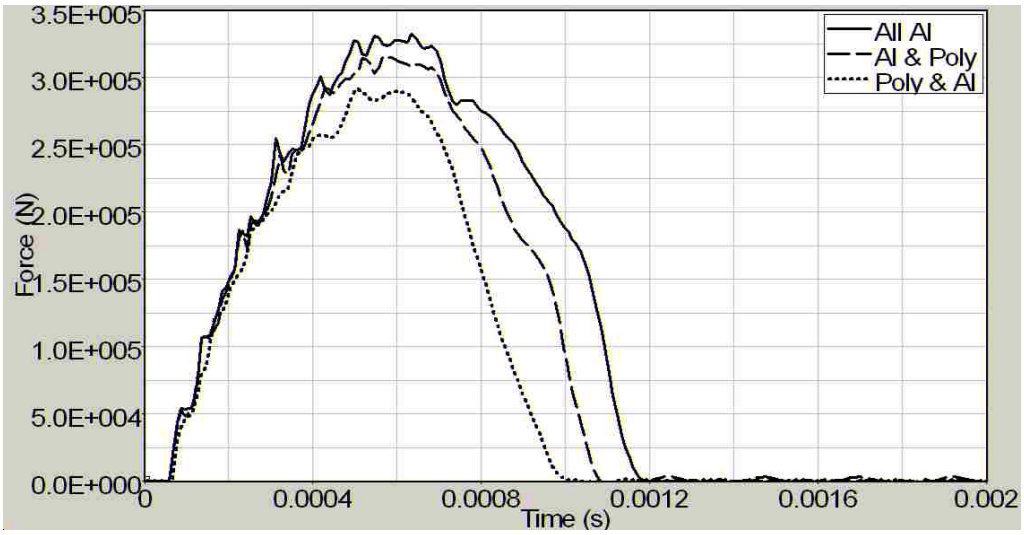

Figure 2.8 Force curves for the aluminum (All Al), the aluminum and polycarbonate (Al & Poly), and the polycarbonate and aluminum (Poly & Al) projectiles from the LS DYNA model.

'Al & Poly' and 'Poly & Al' projectiles, while Figure 2.10 shows their response in the frequency domain, using the Fast Fourier Transform (FFT). The impact accelerations are measured at the central point on the back of the projectile as shown in Figure 2.2.

By inserting the polycarbonate layers in the middle of the projectile, the time domain response shows a reduction in magnitude of the high speed oscillations (Figure 2.9a).

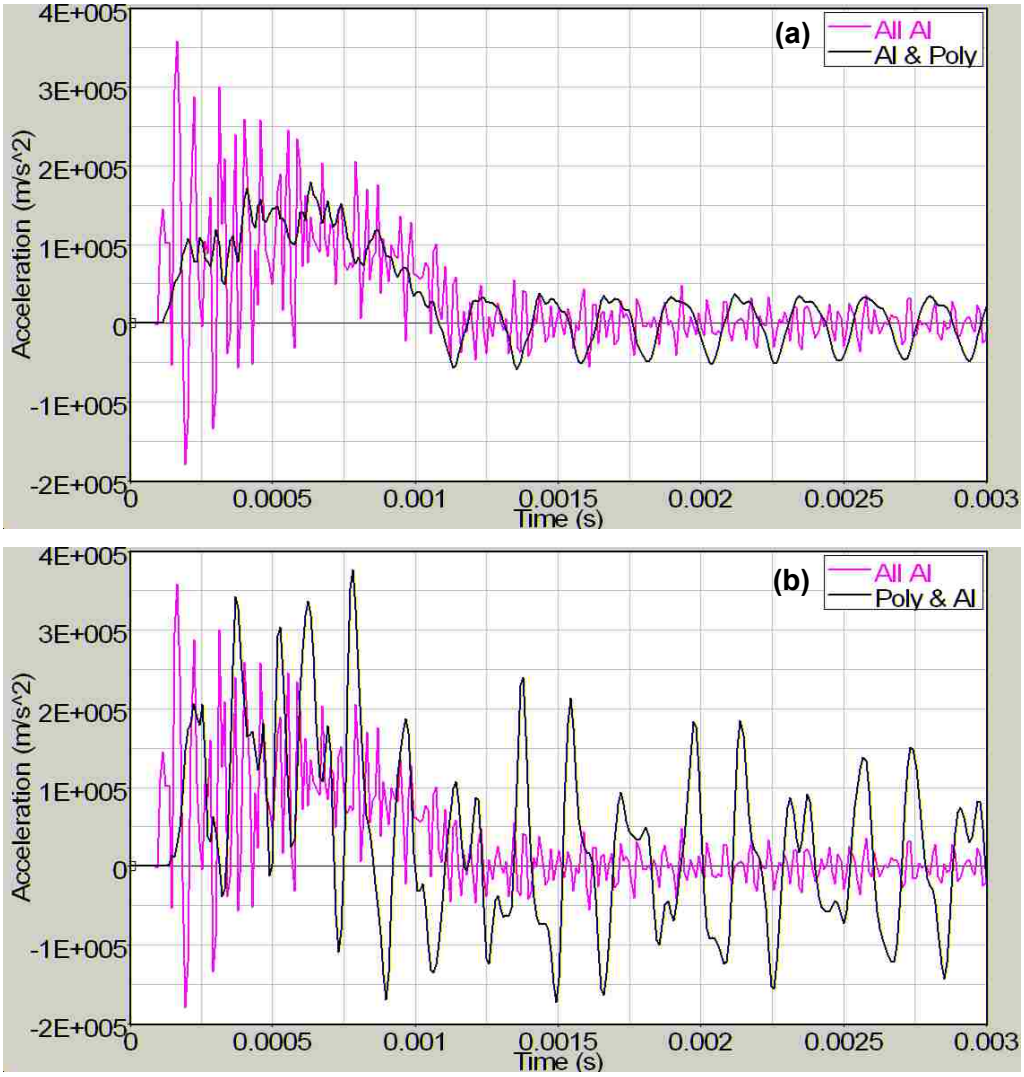

Figure 2.9 Time domain response results of aluminum (All Al), aluminum and polycarbonate (Al & Poly), and polycarbonate and aluminum (Poly & Al) projectiles from the LS-DYNA model.

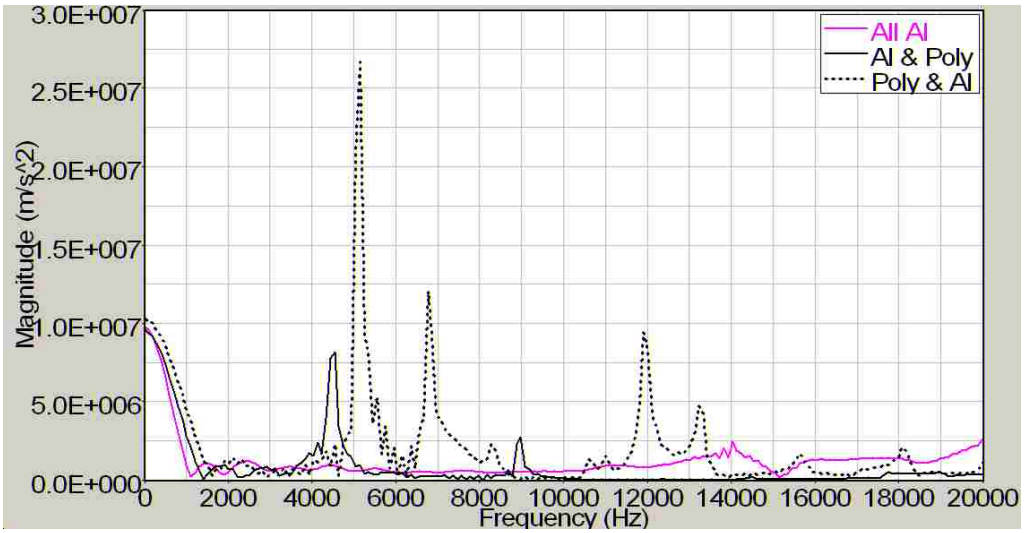

Figure 2.10 Frequency domain response of the aluminum (All Al), the aluminum and polycarbonate (Al & Poly), and the polycarbonate and aluminum (Poly & Al) projectiles from the LS-DYNA model.

Also, the peak of the FFT response curve shifts to a lower frequency which is less damaging to the electronic devices in the projectile (Figure 2.10). When the end plates are changed to polycarbonate and even if there is a polycarbonate layer at the middle of the projectile, the high speed oscillations of the acceleration response curve do not reduce as much as in 'Al & Poly' projectile (Figure 2.9b). The peak of the FFT response curve is shifted to lower frequencies than that in the 'All Al' projectile. However higher frequencies are also observed in 'Poly & Al' projectile compared to 'Al & Poly' projectile.

2.3.1.2 Effect of Number of Layers

Figure 2.11 shows the force curves which are experienced by the projectiles in the second case configurations ('Al & 1 Poly', 'Al & 2 Poly' and 'Al & 4 Poly') colliding with the honeycomb mitigator at 80 km/sec impact velocity. 'Al & 1 Poly' has one layer of polycarbonate at the middle, 'Al & 2 Poly' has two layer of polycarbonate and 'Al & 4

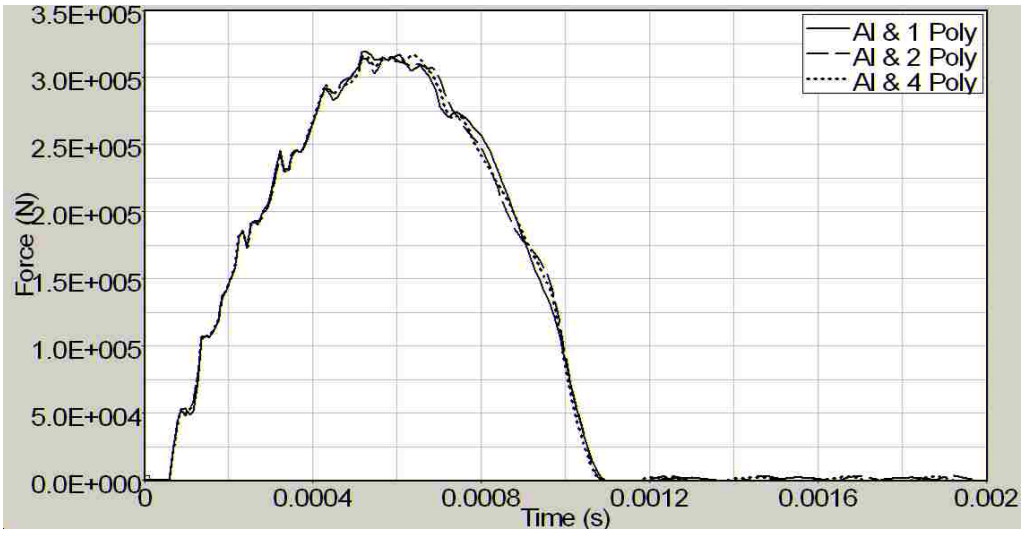

Figure 2.11 Force curves for one (Al & 1 Poly), two (Al & 2 Poly) and four (Al & 4 Poly) polycarbonate layer projectiles from the LS-DYNA model.

Poly' has four layer of polycarbonate. Since all projectiles have the same weight, the force experienced by each projectile is also almost the same.

Figure 2.12 shows the time domain response results of the air-gun models of the second case projectiles, while Figure 2.13 shows their response in the frequency domain using the FFT. When number of polycarbonate layers is increased from one to two, the acceleration in the projectile shows fewer oscillations (Figure 2.12a). When the layers of polycarbonate are further increased to four, no significant differences in acceleration oscillations are detected. However, if we take a closer look, time domain response seems to show higher frequency oscillations when there are four layers compared to two layers of polycarbonate (Figure 2.12b). As shown in frequency domain response (Figure 2.13), the one layer polycarbonate projectile has the peaks at the lowest and the highest frequencies among the three different projectiles. As a number of polycarbonate layers increases, the lowest frequency of the peak increases. However, the highest frequency of

the peak for the four layer polycarbonate projectile occurs at a higher frequency than that of the two layer polycarbonate projectile, which is an undesired result.

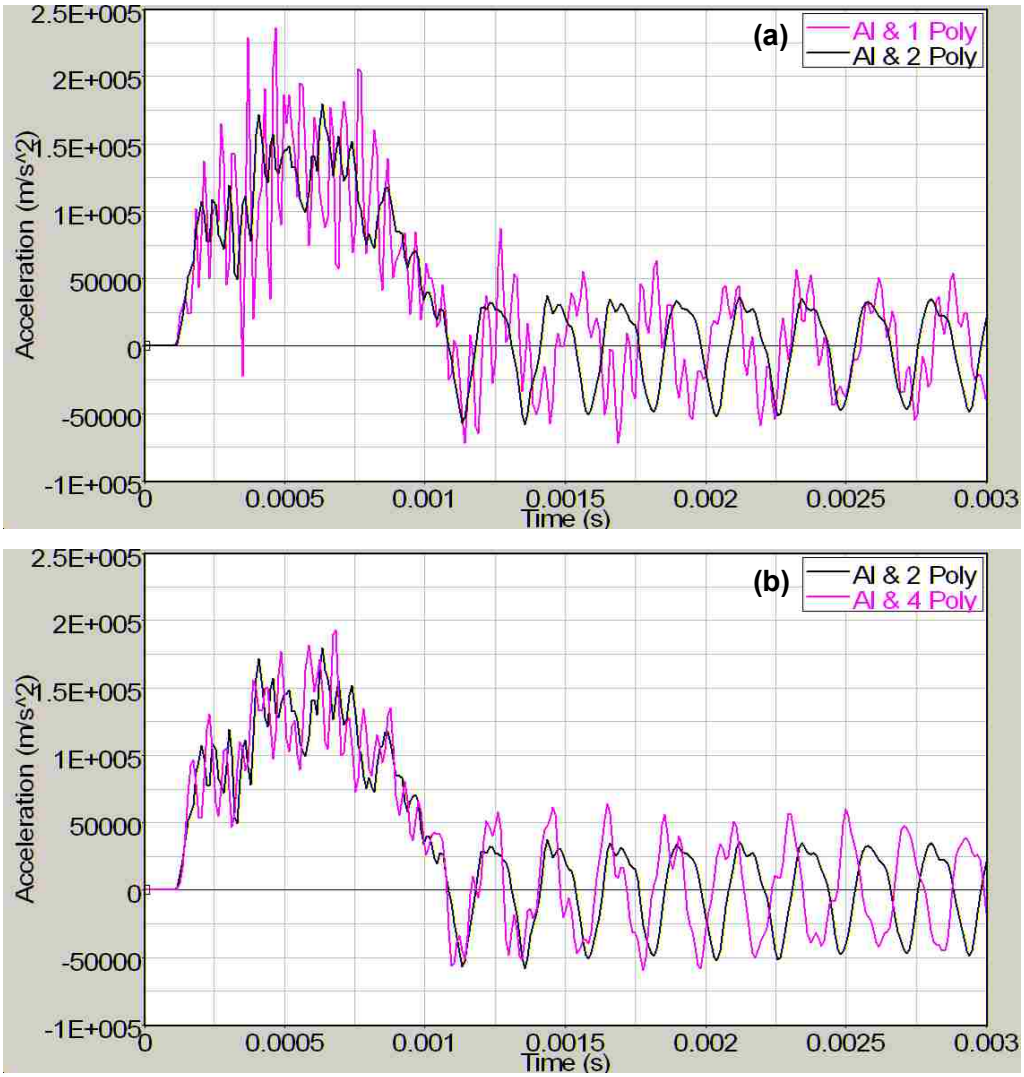

Figure 2.12 Time domain response results of one (Al & 1 Poly), two (Al & 2 Poly) and four (Al & 4 Poly) polycarbonate layer projectiles from the LS-DYNA model.

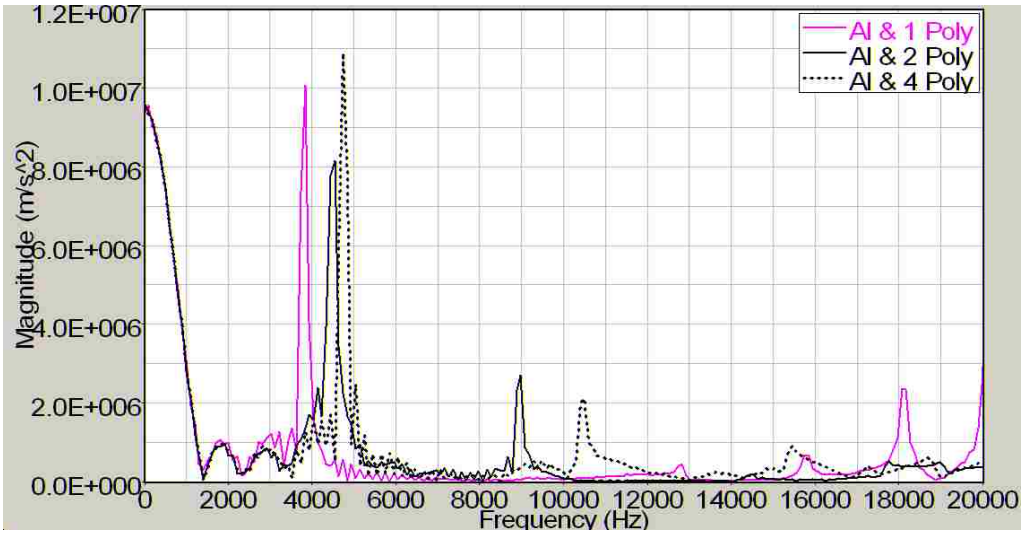

Figure 2.13 Frequency domain response of one, two and four polycarbonate layer projectiles from the LS-DYNA model.

2.3.2 Results of UM-GUI Model

Figure 2.14 shows the force curves that are calculated based on the configuration (the first case) of the projectiles with 80 km/sec impact speed and the experimental strain rate of the honeycomb mitigator. Due to the differences in the weight (Table 2.2), the force experienced by each projectile is different.

Figure 2.15 shows the time domain response results of the air-gun models of 'All Al', 'Al & Poly' and 'Poly & Al' projectiles. Figure 2.16 shows their response in the frequency domain, using the Fast Fourier Transform (FFT). 'All Al' and 'Al & Poly' projectiles do not show significant differences and both acceleration curves show only small oscillations. However, 'Al & Poly' projectile has a slightly higher maximum acceleration compared to 'All Al' even though 'Al & Poly' projectile has less applied impact force (Figure 2.15a). 'Poly & Al' projectile shows significant oscillations and the highest maximum acceleration compared to the other two projectiles (Figure 2.15b).

While ‘Poly & Al’ projectile has the least applied impact force, significantly large magnitude and many peaks of FFT response are observed for ‘Poly & Al’ projectile compared to the other two projectiles (Figure 2.16). ‘Al & Poly’ projectile has the peaks at both the lowest and the highest frequencies among the three projectiles.

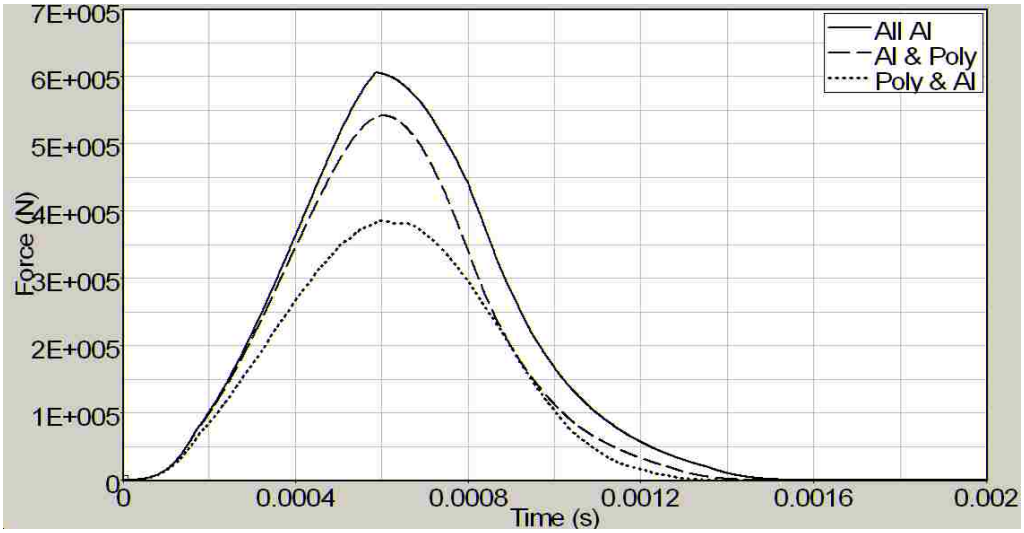

Figure 2.14 Force curves for the aluminum (All Al), the aluminum and polycarbonate (Al & Poly), and the polycarbonate and aluminum (Poly & Al) projectiles in UM-GUI model.

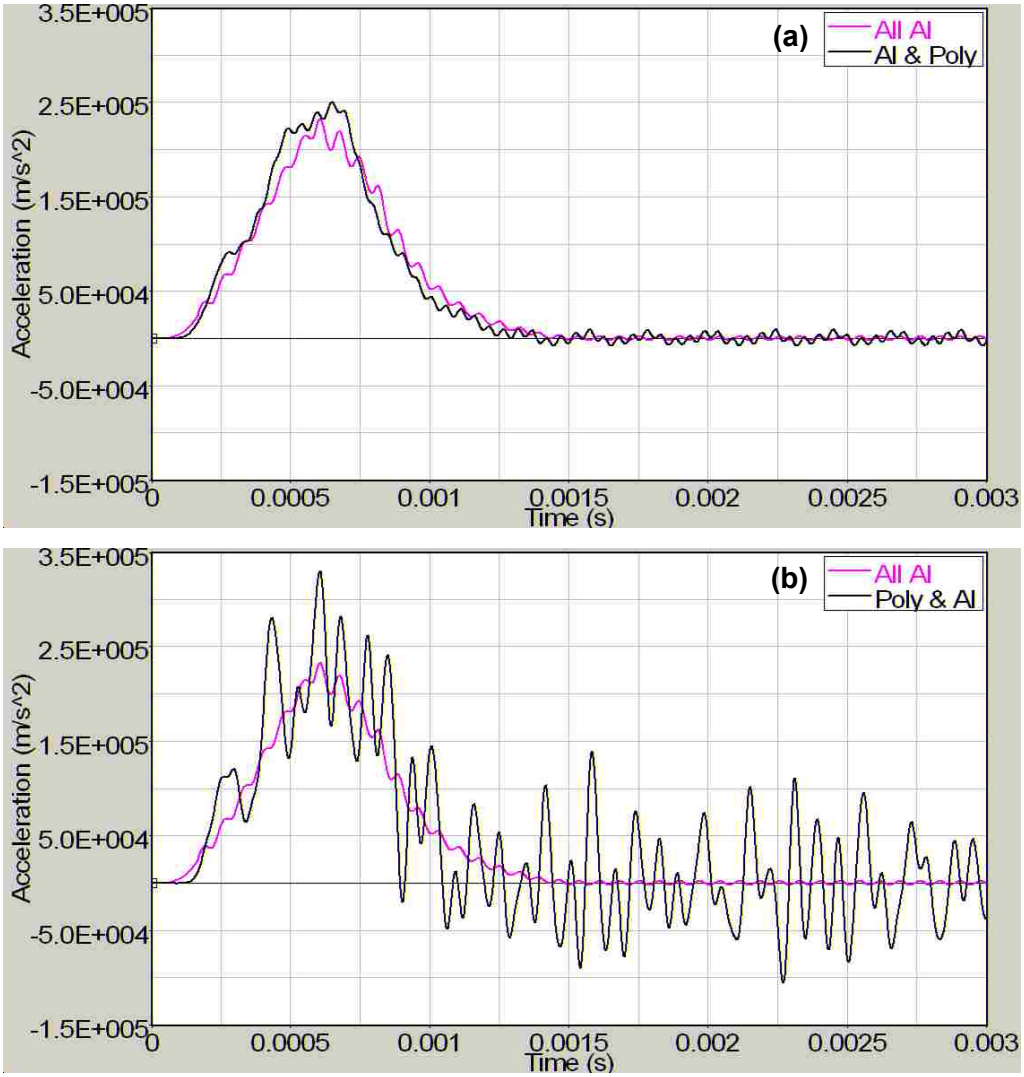

Figure 2.15 Time domain response results of the aluminum (All Al), the aluminum and polycarbonate (Al & poly), and the polycarbonate and aluminum (Poly & Al) projectiles from UM-GUI model.

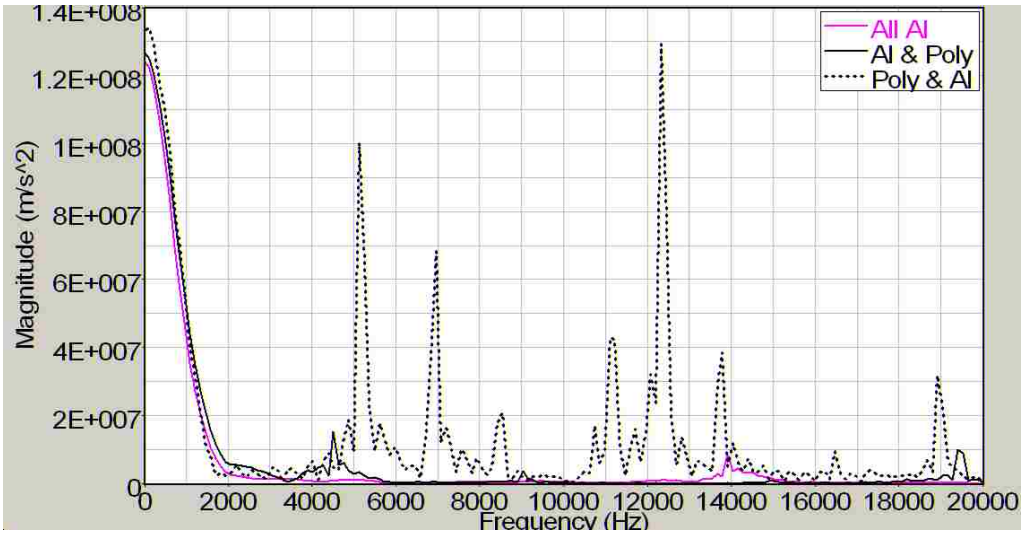

Figure 2.16 Frequency domain response of aluminum (All Al), aluminum and polycarbonate (Al & Poly), and polycarbonate and aluminum (Poly & Al) projectiles from UM-GUI model.

2.4 Discussion

Two different models, LS-DYNA and UM-GUI, are used to simulate air-gun tests. Their results do not exactly match but overall trends show similarities. When the force curves experienced by the projectiles are compared between two models, curves from UM-GUI are smooth compared to LS-DYNA. UM-GUI is a simplified finite element code with fewer numbers of elements than LS-DYNA; this may have partially contributed to the differences in results.

'Al & Poly' projectile shows high frequency vibration mitigation. However, when the polycarbonate end plates are used (Poly & Al), the acceleration response does not reduce as many high frequency oscillations as in 'Al & Poly' projectile. Also, when the polycarbonate end plates are used instead of aluminum, the maximum magnitude of acceleration increases compared to the other two projectiles. These trends are observed from both LS-DYNA and UM-GUI results.

When the number of polycarbonate layers is increased from two to four, high frequency oscillations seem to increase instead of the intended acceleration mitigations. The peaks at the lowest frequencies shift to higher frequencies by increasing the number of polycarbonate layers. However, this is not the case for the peaks at highest frequencies (observed up to 20,000 Hz). 'Al & 1 Poly' projectile has the highest peak among three projectiles than four layers and two layers. Due to this peak, 'Al & 1 Poly' projectile oscillates more than the other two projectiles (two and four layers). This is followed by 'Al & 4 Poly' projectile.

Bibliography

Altair Engineering, Inc. (2004). Altair HyperWorks 7.0 [computer software]. Troy, Michigan.

Baz, A. (2006). UM-GUI: Mitigator/Bird Analysis [computer software]. University of Maryland.

Bouland, A. and Chowdhury, M. R. (2005). Analytical simulation and verification of air gun impact testing. *Army Research Laboratory*, ARL-TR-3559.

Chowdhury, M. R. and Tabiei, A. (2003). Development of an air gun simulation model using LS-DYNA. *Army Research Laboratory*, ARL-TR-3016.

Hexcel Corporation (1999). HexWebHoneycomb Attributes and Properties. Retrieved November, 29, 2007, from http://www.hexcel.com/Products/Downloads/Brochures

Karpanan, K. (2005). Finite Element Analysis of a projectile during gun launch. Thesis, University of Nevada, Las Vegas.

Hallquist, J. O. (Comp.). (2006). LS-DYNA Theory manual. Livermore, California.

Livermore Software Technology Corporation (2003). *LS-DYNA Keyword user's manual*, Version 970, Livermore, California.

Livermore Software Technology Corporation (2006). LS-DYNA [computer software]. Livermore, California.

Lu, W. and Hinnerichs, T. (2001). Crush of high density aluminum honeycombs. *Proceedings of 2001 ASME International Mechanical Engineering Congress and Exposition*, AMD-Vol. 251, New York, NY, 203-211.

Szymanski, E. A. (2004). Acquiring Data for the Development of a Finite Element Model of an Airgun Launch Environment. *Army Research Laboratory*, ARL-MR-581.

Wu, E. and Jiang, W. (1997). Axial crush of metallic honeycombs. *International Journal of Impact Engineering*, 19, 439-456.

CHAPTER 3

EXPERIMENTAL INVESTIGATIONS

As discussed in Chapter 2, the results of the air-gun test simulations showed that the wave speed mismatch helped to reduce accelerations of the projectile if materials were in certain configuration. In order to verify the concept of mitigation of vibration in a projectile using impedance mismatch, experiments are conducted. However, since air-guns are not readily available for tests, experiments are conducted using an impact hammer.

3.3 Experimental Setup

Experiments are conducted by applying an impact at one end and measuring accelerations on the other end of a suspended structure as shown in Figure 3.1. Two

Figure 3.1 Experimental Setup.

different types of structures, projectile and long bar, are used for the experiments, a detailed description of the projectile and the long bar is given in Section 3.1.2. The projectile is suspended by ropes at two ends with the help of metal bands and the long bar is simply suspended by ropes at two ends. Suspension length of approximately 1 m is used to reduce the resistance to structure's movement from the ropes.

3.3.1 Method and Equipment

As shown in Figure 3.2, the following equipment is used.

(a) Impact hammer, PCB 086D05

(b) Accelerometer, PCB 352C22

(c) Accelerometer, Dytran 3200B

(d) Oscilloscope, Yokogawa DL750

(e) Hand Held Shaker, PCB 394C06

Figure 3.2 Pictures of all the equipments used; (a), (b) & (e): courtesy of PCB Piezotronics, Inc. (c): courtesy of Dytran Instrument, Inc. (d): courtesy of Yokogawa Electric Corporation.

- an impulse hammer with hard and medium tips
- an accelerometer
- a hand held shaker
- a data acquisition system

In order to apply an impact, PCB 086D05 impulse hammer with hard or medium tips is used (Figure 3.2a). The impulse hammer is calibrated measuring the acceleration at one end of the solid metal cylinder weighing 18.00 kg by applying the impact at the other end of the cylinder. Accelerations are measured using PCB 352C22 or Dytran 3200B accelerometers depending on the acceleration response. Accelerometers are calibrated using a hand held shaker PCB 394C06 which generates the operating frequency of 159.2 Hz and the acceleration output of 1 g. The accelerometer, PCB352C22, has a sensitivity of approximately 10 mV/g and measurement ranges of ± 4,900 m/s^2 while Dytran 3200B accelerometer has a sensitivity of approximately 0.05 mV/g and measurement ranges of ± 686,000 m/s^2. Both accelerometers have their frequency range up to 20,000 Hz. The PCB394C06 accelerometer is attached to a structure using thin layer of beeswax and the Dytran 3200B accelerometer is stud-mounted on a structure. The impulse hammer has a sensitivity of 0.23 mV/N and maximum load of 22,000 N. The data is recorded using an oscilloscope (Yokogawa DL750) by connecting the accelerometer and the impulse hammer through a current source power unit (Dytran 4103C). Acceleration responses are recorded at every 5 μs and frequency domain responses are calculated by the Fast Fourier Transform (FFT) using the software, Altair Hyperview from the recorded time domain response. Final results of time domain response are filtered using a low-pass filter to exclude frequencies above the accelerometer frequency range. The frequency used for

filtering is noted in the figures since cutoff frequency is decided based on the accelerometer frequency range as well as the maximum excitation frequency of each structure.

Once acceleration responses are obtained, logarithmic decrements of structures are calculated using the following equation.

$$\delta = \frac{1}{n} \ln \frac{x_1}{x_n} \qquad \text{Equation 3.1}$$

where, δ is a logarithmic decrement, x_1 is the greater of two amplitude and x_n is the amplitude at n periods away from x_1. The damping ratio, ζ, is then expressed as the following equation using the logarithmic decrement (Thomson, 1993).

$$\zeta = \frac{1}{\sqrt{1 + \left(\frac{2\pi}{\delta}\right)^2}} \qquad \text{Equation 3.2}$$

3.3.2 Experimental Structures

Two different types of test structures are used to conduct the experiments. First, projectiles similar to the air-gun simulations are built and used to conduct the experiments. Next, long bars are used to make the test objects.

3.3.2.1 Projectile

Similar to the air-gun model projectiles described in Chapter 2, 101.6 mm diameter and 152 mm long projectiles are built for the experiments. The projectiles are made of aluminum sections or aluminum and polycarbonate sections. Each projectile is made of two end plates and four rings at the middle which are assembled by six-9.525 mm diameter bolts preloaded with 21 N-m or 34 N-m torque. Both end plates have 101.6 mm

diameter and are 25 mm thick, and each ring has the outside diameter of 101.6 mm, the inside diameter of 50.8 mm and is 25 mm thick.

Figure 3.3 shows three different layer configurations used for conducting the experiments. The first configuration, 'All Al', is made of all aluminum parts (Figure 3.3a). The second configuration, 'Al & 1 Poly', has one layer of polycarbonate at the middle of the structure (Figure 3.3b). Finally, the last configuration, 'Al & 2 Poly', has two layers of polycarbonate between aluminum parts. The first type of projectile is made of aluminum only, which is named as 'All Al' (Figure 3.3a). Figure 3.4 shows the

(a) All Al

(c) Al &1 Poly

(b) Al & 2 Poly

Figure 3.3 Schematic projectile and each plate used to build the projectile.

dimensions and various components of the projectile. All the projectiles are constructed in the same manner using two end plates and four rings.

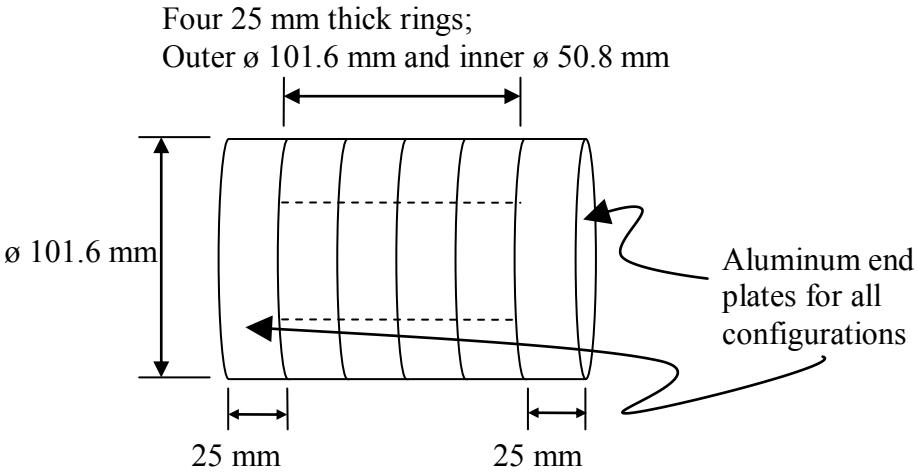

Polycarbonate Ring | Aluminum End Plate | Aluminum Ring

Figure 3.4 Schematic projectile and each plate used to build the projectile.

3.3.2.2 Long Bar

A long experimental structure is built to study acceleration response without the interference between an applied impact wave and reflected wave. The long bar is built using three components fastened by a 5/16-24 thread as shown in Figure 3.5. There are two layer configurations. In the first case, 'Al-Al-Al', all three parts of the structure are made of aluminum. In the second case, 'Al-Nylon-Al', the center part of the structure is made of nylon while ends are made of aluminum. Note that nylon has similar wave speed and density to polycarbonate. The dimensions of each bar are listed in Table 3.1.

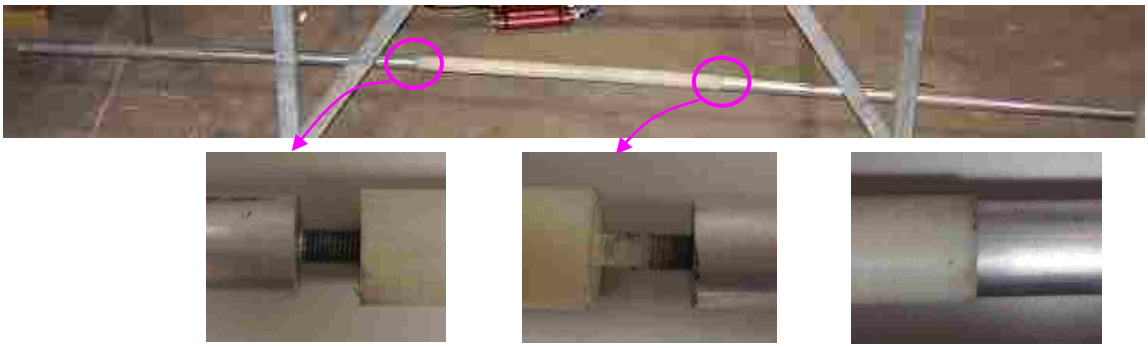

Figure 3.5 The long projectile made of aluminum and nylon and its connections.

Table 3.1 Dimensions of the long structure components

	Part 1	Part 2		Part 3
	Aluminum	Aluminum	Nylon	Aluminum
Length (mm)	718	521	514	692
Diameter (mm)	22.5	22.5	25.1	22.5
Weight (kg)	0.761	0.555	0.288	0.746

3.4 Results

3.4.1 Projectile

The experimental results of the projectile tests are shown in Figures 3.6 to 3.9. Three different configurations were used to investigate the acceleration response under two different impact tips. Additionally, two different bolt tensions (21 N-m and 34 N-m torque) were used to study the effect of bolt tensions to acceleration responses.

As clearly seen in Figure 3.6, applied impact of each structure has identical forces. The peak magnitudes of applied force using the hard and medium tips were approximately 10,000 and 3,800 N, respectively. The impact durations are approximately 0.2×10^{-3} seconds for the hard tip and 0.6×10^{-3} seconds for the medium tip. The experimental results obtained using these two forces are chosen because of the similar impulses.

Figure 3.7 shows the FFT responses of all the configurations up to a frequency of 10,000 Hz. There were no observable peaks in the FFT response beyond 10,000 Hz. Therefore, the time domain responses shown in Figures 3.8 and 3.9 were filtered at cutoff frequency of 10,000 Hz.

Figure 3.8 show acceleration responses obtained applying the hard tip impact to the structure fastened with bolt tension 21 and 34 N-m torque. Figure 3.9 shows acceleration response obtained by applying the medium tip impact fastened with 21 and 34 N-m torque. All four figures show that 'All Al' had the lowest magnitude of accelerations followed by 'Al & 1 Poly'. The highest magnitude of acceleration was observed in 'Al & 2 Poly'.

The applied torque to fasten the bolts did not show much effect on the magnitude of acceleration response. However, the peak in FFT response shifted to higher frequency for all the layer cases when torque was increased from 21 N-m to 34 N-m (Figure 3.7). The peak values were observed approximately at 7,400 Hz, 5,300 Hz and 5,800 Hz in 'All Al', 'Al & 1 Poly' and 'Al & 2 Poly' with 21 N-m torque, respectively. Similarly, 'All Al', 'Al & 1 Poly', and 'Al & 2 Poly' with 34 N-m torque showed peaks at 9,000 Hz, 5,700

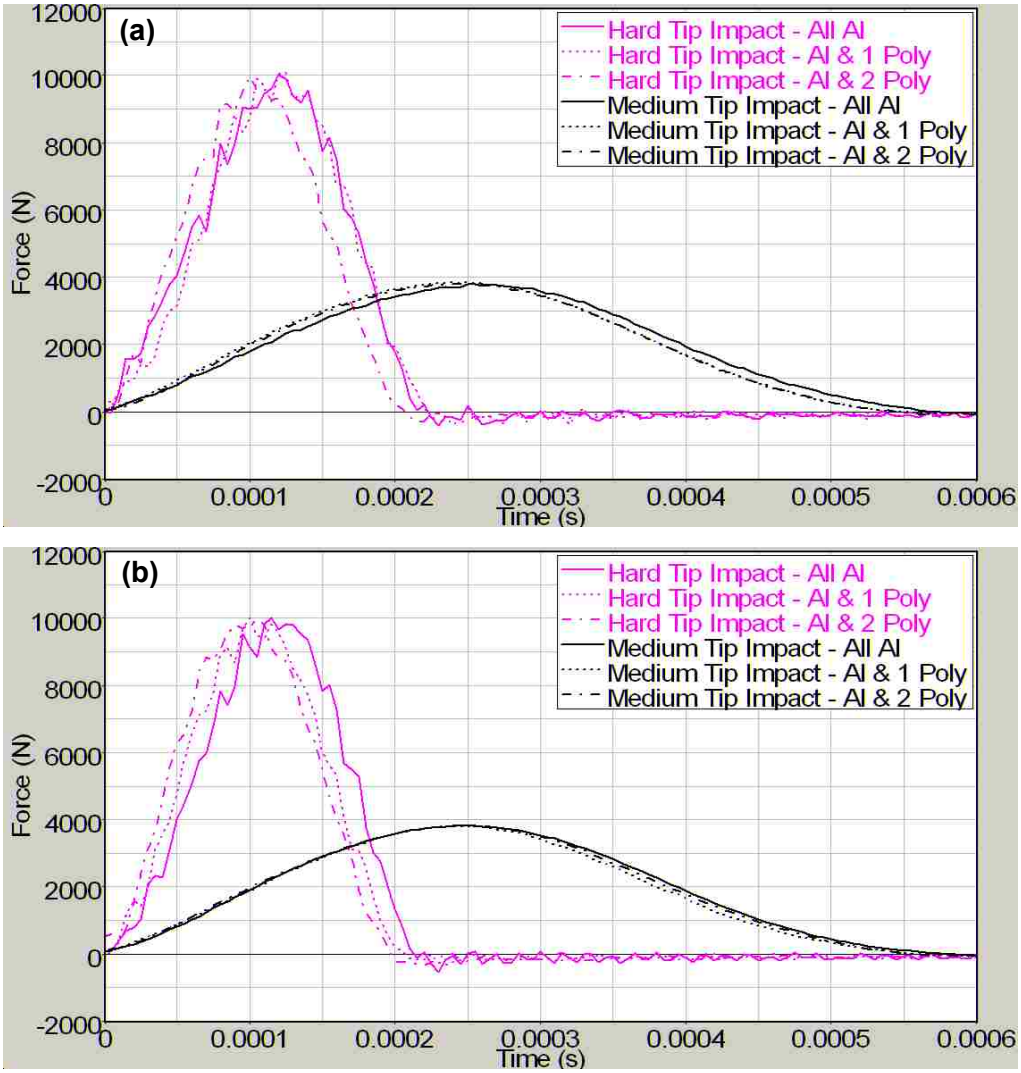

Figure 3.6 Applied impact forces on experimental projectiles fastened with bolt torque of (a) 21 N-m and (b) 34 N-m.

and 6,300 Hz. These peaks were observed for both hard and medium tip impact cases. Even if a different torque was used to fasten the structure, the lowest excitation frequency was always observed in 'Al & 1 Poly' followed by 'Al & 2 Poly' and 'All Al'.

Magnitude of the peaks in the FFT response did not show a consistent trend. For the hard tip impact, the largest magnitude of the peak was observed in 'Al & 2 Poly' followed by 'Al & 1 Poly' and 'All Al' for both 21 and 34 N-m torque cases. However,

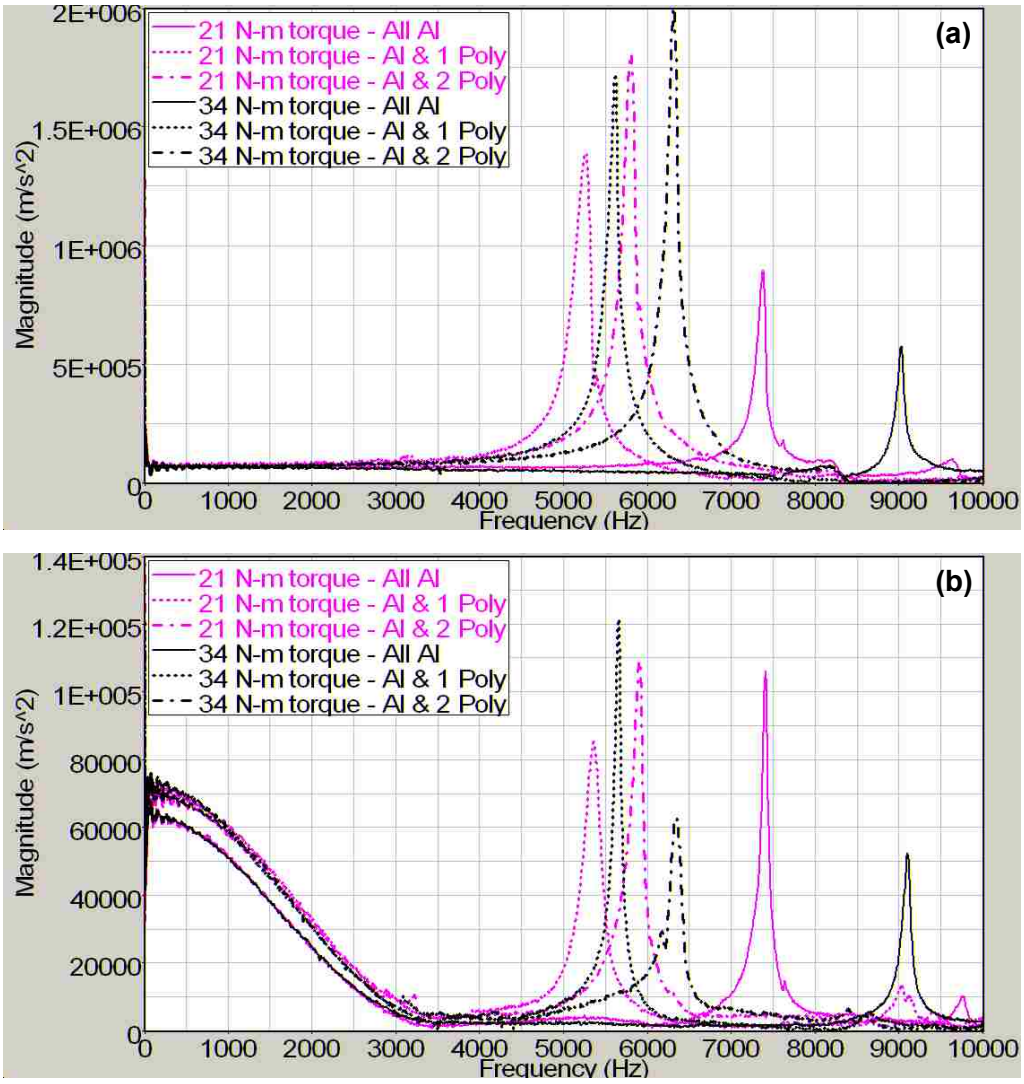

Figure 3.7 Experimental results of FFT responses of the experimental projectiles under impact loading using (a) hard and (b) medium tip impacts.

for the medium tip impact, the largest magnitude of the peak was observed in 'Al & 2 Poly' for 21 N-m torque case and 'Al & 1 Poly' for 34 N-m torque case. For both torque cases, the magnitude of the peak for 'All Al' was smaller than the one for 'Al & 2 Poly'.

Table 3.2 shows the logarithmic decrements and the damping ratios of all the projectile configurations. The logarithmic decrements are calculated using two

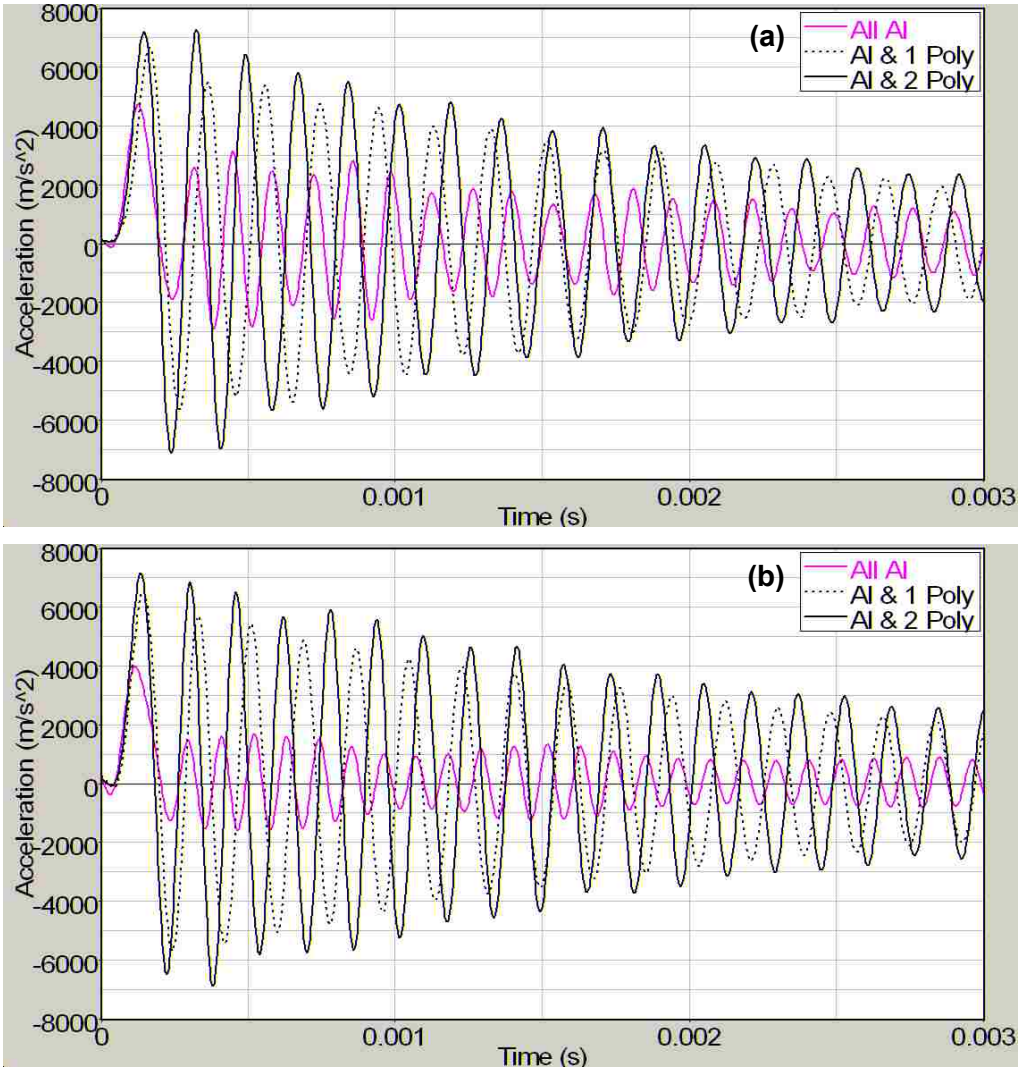

Figure 3.8 Experimental results of acceleration response of the projectiles under impact loading using the hard tip with (a) bolt tension of 21 N-m and (b) bolt tension of 34 N-m. 10,000 Hz cutoff frequency is used for low-pass filter.

amplitudes taken between 0.001 and 0.005 seconds. A number of periods included within this time interval was approximately 20 to 40 depending on the projectile configurations.

The lowest damping ratio was observed in 'All Al' followed by 'Al & 1 Poly' and 'Al & 2 Poly'. The differences between one material projectile (All Al) and two material projectiles (Al & 1 Poly or Al & 2 Poly) were significant. However, differences between

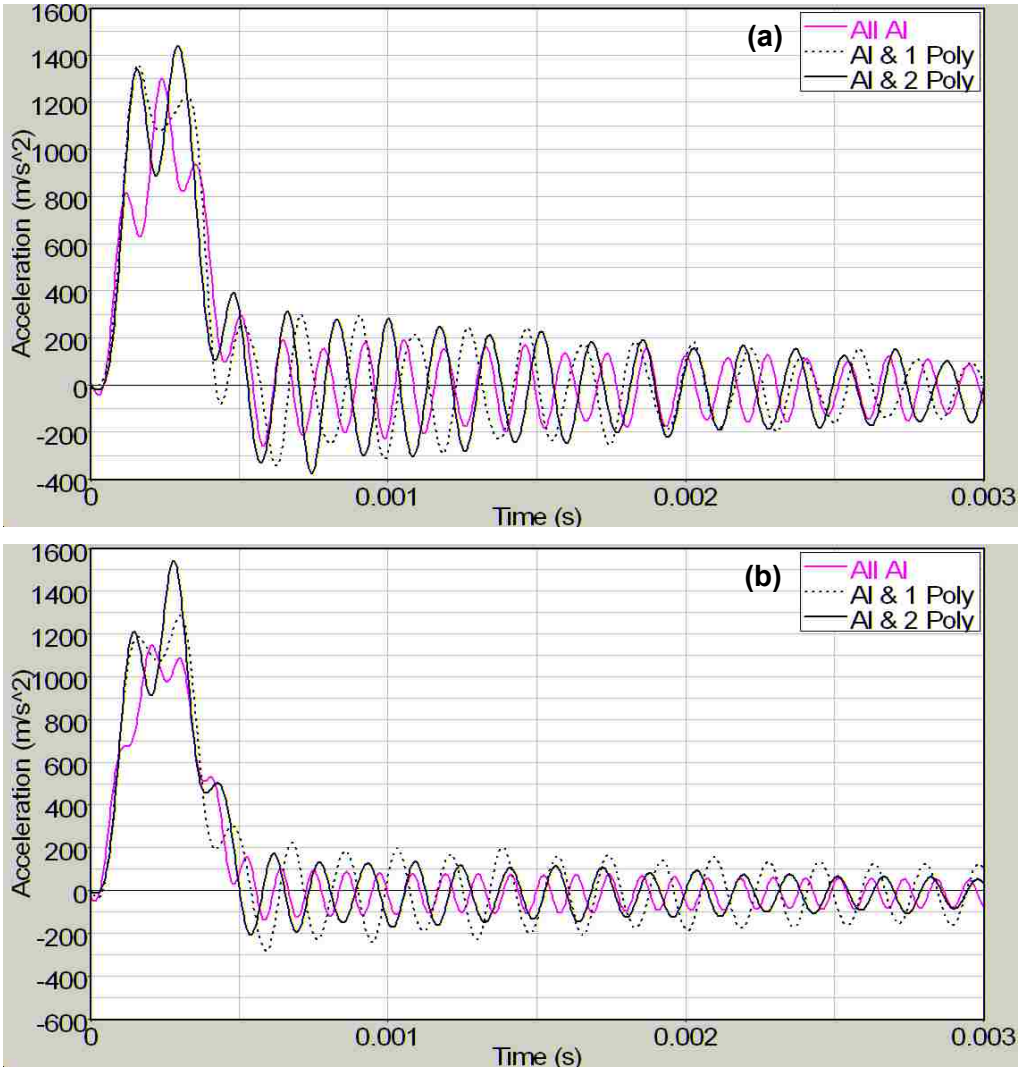

Figure 3.9 Experimental results of acceleration response of the projectiles under impact loading using the medium tip with (a) bolt tension of 21 N-m and (b) bolt tension of 34 N-m. 10,000 Hz cutoff frequency is used for low-pass filter.

Table 3.2 Logarithmic decrements and damping ratios of the projectiles

	Bolt Torque	All Al	Al & 1 Poly	Al & 2 Poly
Logarithmic Decrement	21 N-m	0.0366	0.0963	0.0976
	34 N-m	0.0304	0.0552	0.0566
Damping Ratio	21 N-m	0.0058	0.0153	0.0155
	34 N-m	0.0048	0.0088	0.0090

the two material projectiles (Al & 1 Poly or Al & 2 Poly) were minor. The order of the damping ratio was same for both projectiles assembled using 21 N-m and 34 N-m bolt torques. However, when the bolt torque was increased from 21 N-m to 34 N-m, the damping ratio was reduced.

3.4.2 Long Bar

Figures 3.10 through 3.12 show the experimental results obtained from the long bars. Similar to the projectile cases, two different forces, hard and medium tip impacts, were applied. The hard and medium tip impacts had magnitudes of approximately 5,300 and 2,100 N, respectively (Figure 3.10).

The acceleration of the hard tip impact shows that the long bar made of all aluminum (Al-Al-Al), had slightly higher acceleration than the bar made of aluminum and nylon (Al-Nylon-Al; Figure 3.11a). The maximum acceleration of 'Al-Al-Al' was about 49,000 m/s^2, while the maximum acceleration of 'Al-Nylon-Al' was approximately 23,000 m/s^2. This difference was more prominent for the medium tip impact cases (Figure 3.11b). The maximum accelerations were approximately 11,000 m/s^2 for 'Al-Al-Al' and 3,000 m/s^2 for 'Al-Nylon-Al'. The acceleration results were filtered at 5,000 Hz based on the peaks observed in FFT responses (Figure 3.12). Unlike the FFT response observed in the

projectile, the highest peak in FFT response obtained from the hard and medium tip impacts appeared at different frequencies as shown in Figure 10. The 'Al-Al-Al' configuration had the highest peak at 3,900 Hz for hard and 2,454 Hz for medium tips, while 'Al-Nylon-Al' configuration had highest peaks at 3,546 Hz for hard and 421 Hz for medium tips. For both impact cases, 'Al-Nylon-Al' showed the highest peak at lower frequency than that of 'Al-Al-Al'.

Table 3.3 shows the logarithmic decrements and the damping ratios of 'Al-Al-Al' and 'Al-Nylon-Al'. The logarithmic decrements are calculated using two amplitudes taken between 0.02 and 0.07 seconds. A number of periods within this time interval was approximately 100 to 200 depending on the long bar configurations. The logarithmic decrement of 'Al-Al-Al' has slightly higher than that of 'Al-Nylon-Al'. However, the damping ratios obtained from these logarithmic decrements were exactly same for 'Al-Al-Al' and 'Al-Nylon-Al'.

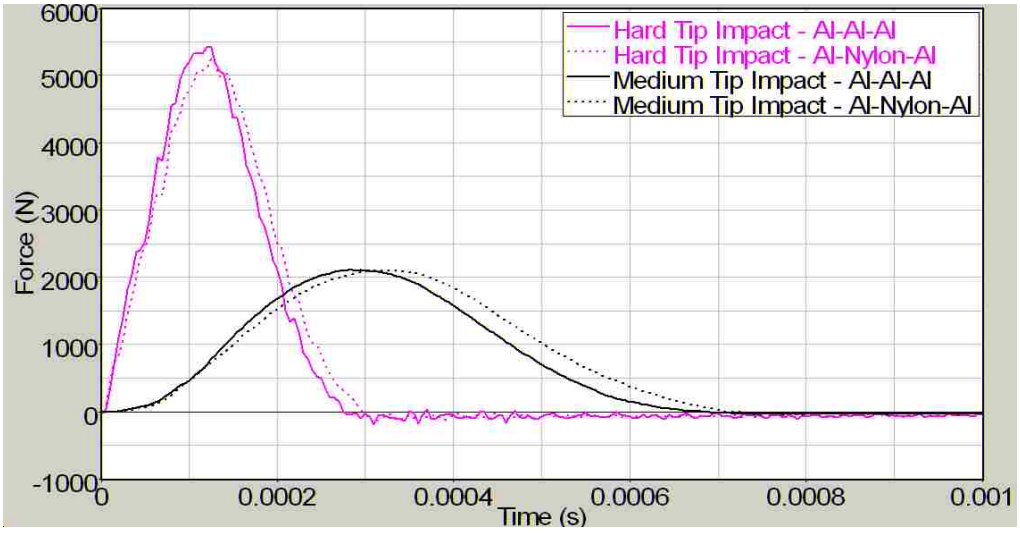

Figure 3.10 Applied impact forces on experimental long structures.

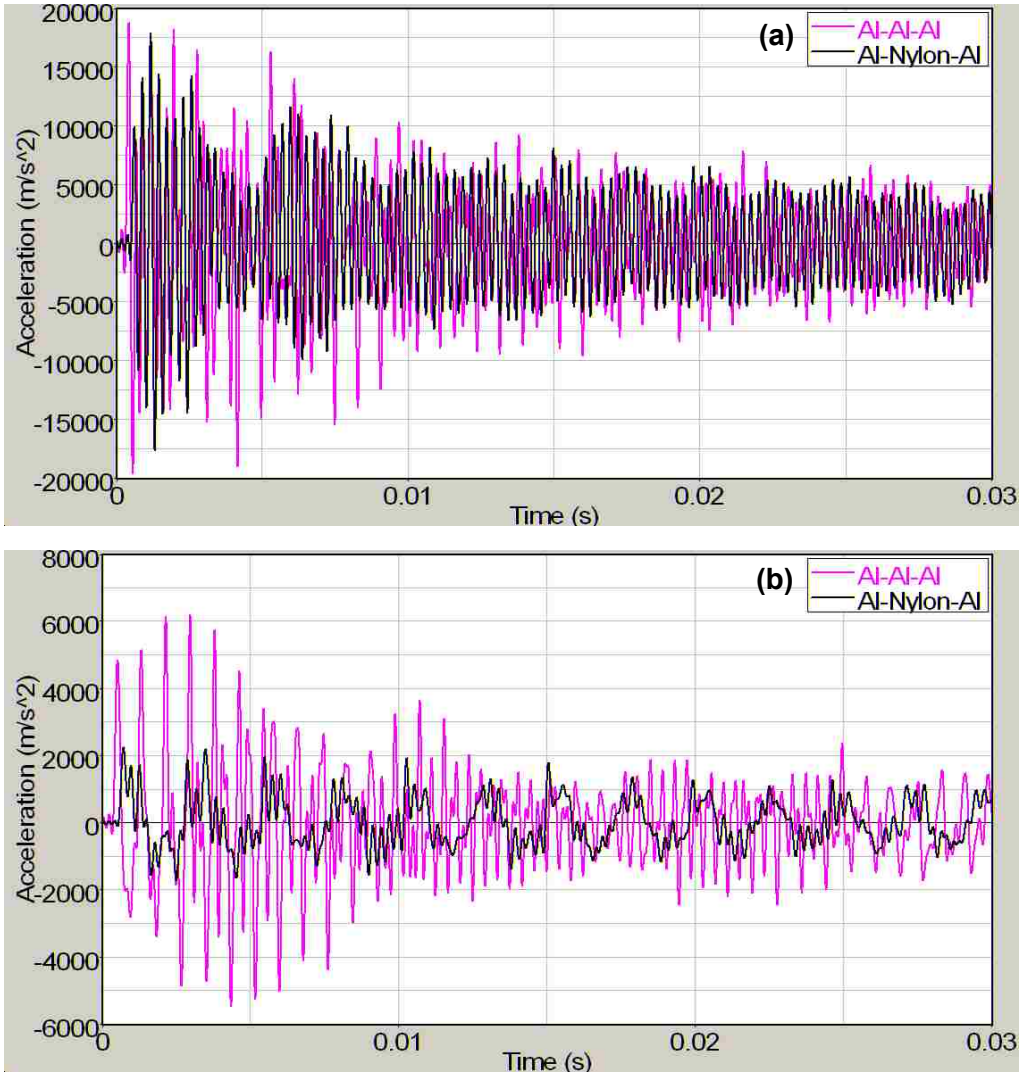

Figure 3.11 Experimental results of acceleration responses of long structures under impact loading using (a) hard and (b) medium tip impacts. 5,000 Hz cutoff frequency is used for low-pass filter.

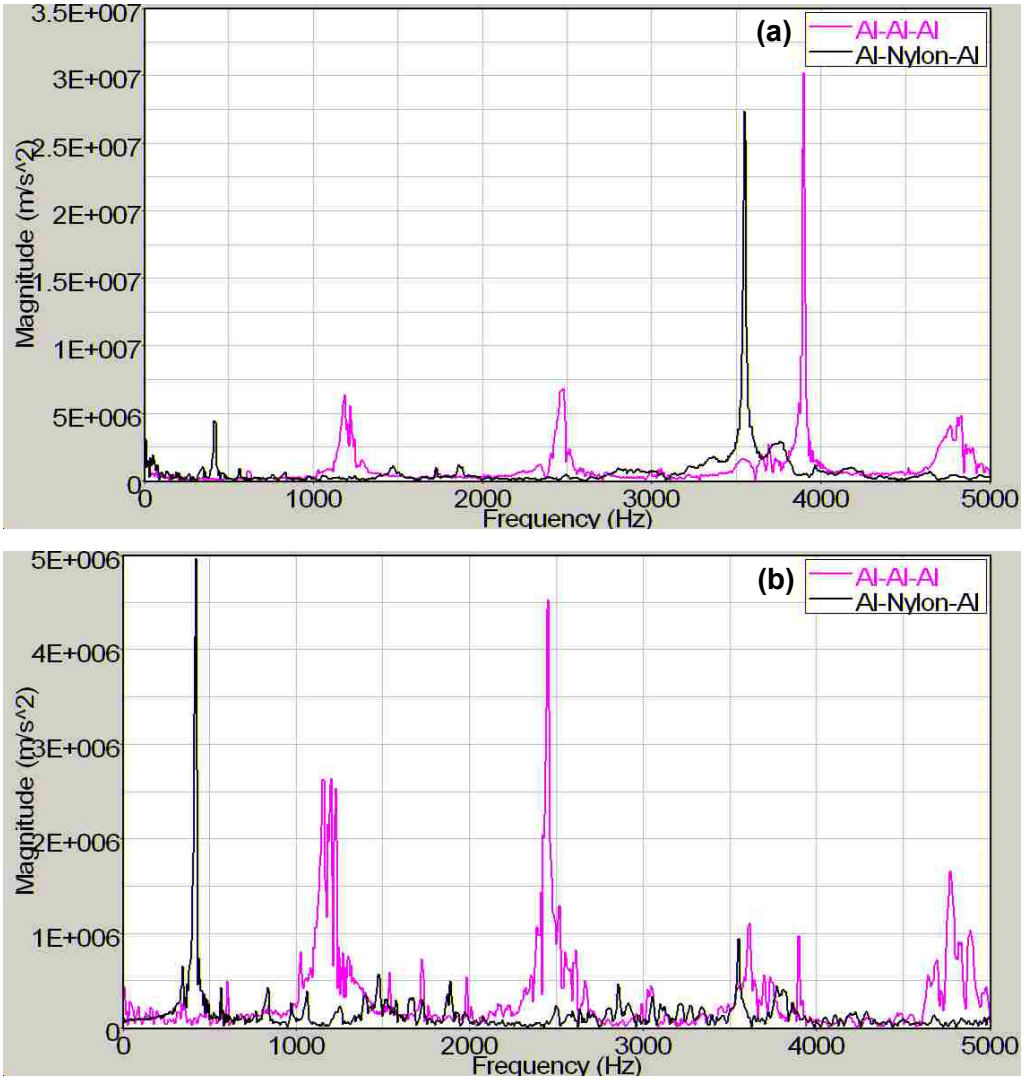

Figure 3.12 Experimental results of FFT responses of long structures under impact loading using (a) hard and (b) medium tip impacts.

Table 3.3 Logarithmic decrements and damping ratios of the long bars

	Al-Al-Al	Al-Nylon-Al
Logarithmic Decrement	0.0085	0.0084
Damping Ratio	0.0013	0.0013

3.5 Discussion

In the experimental investigation of the acceleration response, two different types of structures, projectiles and long bar, are used. In the projectile, there are three different layer configurations, 'All Al', 'Al & 1 Poly' and 'Al & 2 Poly'. The order of maximum magnitude of acceleration response of three different configurations at the end of the structures should be 'All Al' followed by 'Al & 1 Poly' and 'Al & 2 Poly' based on the air-gun simulation results. This order of acceleration responses is also predicted by a well known phenomenon that propagating wave gets split at interface depending on differences in impedance. Since 'All Al' does not have any interface, the entire acceleration wave passes through the structure while 'Al & 1 Poly' reduces the acceleration wave once and 'Al & 2 Poly' twice at their interfaces. However, the experimental results showed otherwise. 'All Al' had the lowest acceleration followed by 'Al & 1 Poly' and 'Al & 2 Poly'. This was true for all the torque and impact tip cases in the projectile.

On the other hand, the long bar showed results as expected. When there is an interface within the structure (Al-Nylon-Al), the acceleration was reduced compared to the structure without an interface (Al-Al-Al). This contradiction might be related to length of structures and impacts. After wave starts traveling and reaches at the other end of the structure, it does not stop there but comes back to the original point where the impact is applied. If the length of the structure is short or impact duration is long, the returning wave might be quick enough to interfere with the applied impact. In that case, the interference might cause an increase in acceleration wave. In the projectiles, 'All Al', 'Al & 1 Poly' and 'Al & 2 Poly' have wave propagation time of one lap (going from one

end to the other end and coming back to the original point where the impact is applied) of about 0.06×10^{-3}, 0.14×10^{-3} and 0.14×10^{-3} seconds, respectively, while the durations of impact are 0.2×10^{-3} seconds for hard and 0.6×10^{-3} seconds for medium tip impacts. Therefore, all the combinations have interference between the applied impact and the propagating acceleration wave. In contrast to the projectiles, all the combinations of the long bars and the impacts do not have any interference between the applied impact and the propagating acceleration wave. Wave propagation time of one lap is about 0.76×10^{-3} seconds for 'Al-Al-Al' and 1.28×10^{-3} seconds for 'Al-Nylon-Al', while the durations of impact using the hard and medium tips are 0.3×10^{-3} and 0.6×10^{-3} seconds, respectively. Li et al. (2001) reported similar phenomena in their wave stress analysis in layered composite material.

The damping ratios of the projectiles are higher than that of the long bars. This might have been due to the assemble conditions of the structures. The projectile is made of plates and assembled with six bolts while each part of the long bar is threaded into the other part. When bolt torques are increased from 21 N-m to 34 N-m, the damping ratios decreased for all the projectile configurations. This is because friction between plates is reduced by increasing bolt torques. On the other hand, each part of the long bar is fastened with the others and the connection surface is much smaller compared to the projectile. Therefore, friction between parts in the long bars is less compared to the projectile, which resulted in lower damping ratios.

Bibliography

Li, Y., Ramesh, K. T. and Chin, E. S. C. (2001). Dynamic characterization of layered and graded structures under impulsive loading. *International Journal of Solids and Structures*, 38, 6045-6061.

Thomson, W. T. (1993). *Theory of vibration with applications* (4th ed.). New Jersey: A Simon & Schuster Company.

CHAPTER 4

COMPUTATIONAL VERIFICATIONS

In chapter 2, the air-gun simulations are reported and the experiments are conducted to verify the impedance mismatch concept and reported in chapter 3. However, the experiments are conducted using an impact hammer, which is not same condition as the air-gun simulations. Therefore, computational verifications of the experiments are conducted and reported in this chapter. In this study, LS-DYNA (Livermore, 2006) is used to conduct the computational verifications using refined finite meshes with the aid of Altair HyperMesh software (Altair, 2004).

Furthermore, an effect of applied impact force on acceleration responses of the structures is studied using the experimental simulation model and reported in this chapter.

4.1 Model Setup

4.1.1 Simulation of Experimental Condition

Two different types of cylindrical structures which are similar to those used in the experiments are modeled using the software, Altair HyperMesh (Figure 4.1). 14,496 and 17,952 eight-node solid hexahedron elements are used for the short and long cylindrical structures, respectively. Accelerations are then computed at the center node of one end by applying impact forces at nine center nodes of the other end using the finite element software, LS-DYTNA. The impact forces used in the models are obtained from the experiments. One-point Gaussian quadrature is used to carry out the volume integration and constant stress solid element type is used in the computational process based on substantial savings in computer time (Livermore, 2003 and Hallquist, 2005).

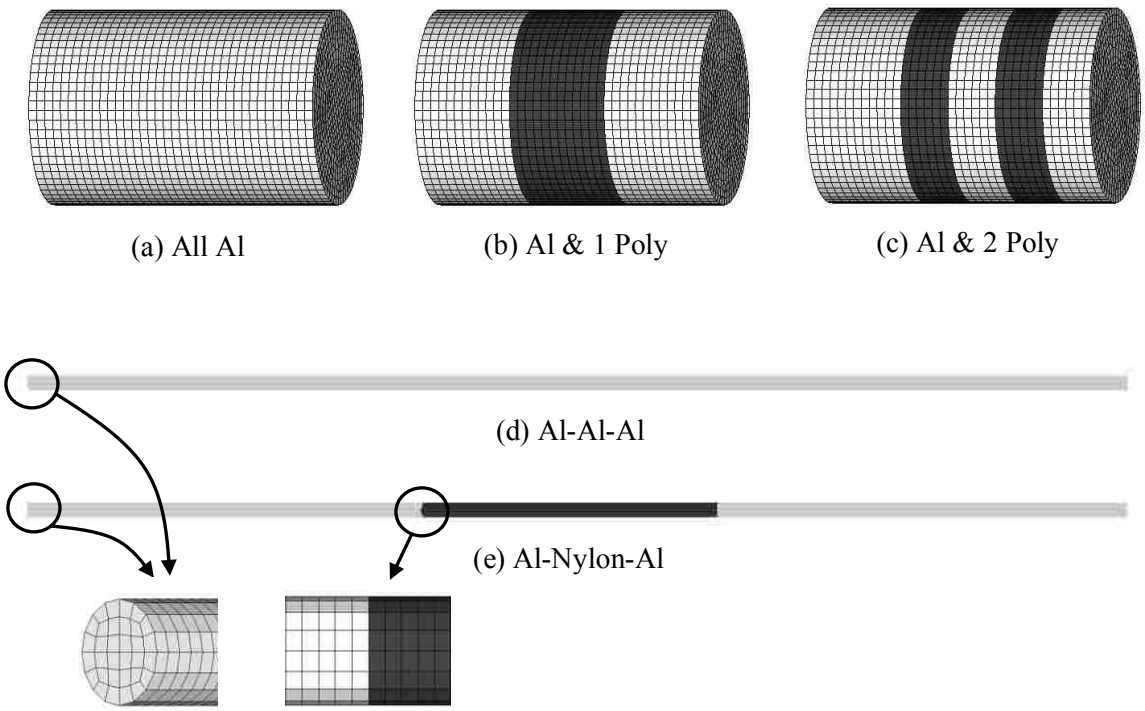

Figure 4.1 Simulation models of the projectiles (figures a, b and c) and long bars (figures d and e). Different colors represent different materials; (a) a projectile made of aluminum only (b) a projectile made of aluminum and one layer of polycarbonate at the middle (c) a projectile made of aluminum and two layers of polycarbonate (d) a long bar made of aluminum only (e) a long bar made of aluminum and nylon at the middle.

The computational study follows the same configurations as the experiments. The model uses shared nodes between two different materials unlike the experimental structures which are detachable. Material properties used in the model are tabulated in Table 4.1. Note that the density of each material is modified to match with the weight of the experimental structures since the model uses simplified structures such as no bolts and no minor differences in dimensions. As shown in Figure 4.1e, "Al-Nylon-Al" model does not include diameter differences between aluminum and nylon parts unlike in the experimental structure. This was simplified to reduce computational time since there was

Table 4.1 Material properties used in the computational study

Structure	Material	Density[a] ρ (kg/m3)	Young's Modulus E (GPa)	Poisson's Ratio μ	Yield Strength σ_y (MPa)	Impedance Z (kg/m^{2}s)
Projectile	Polycarbonate	1848.5	4.27	0.35	62.0	2.81E+06
	Aluminum	3168.1	68.00	0.33	250.0	1.47E+07
Long Bar	Aluminum	2761.7	68.00	0.33	250.0	1.37E+07
	Nylon	1435.0	1.90	0.35	62.4	1.65E+06

[a]Modified density to match with the weight of experimental structure

only a minor change in acceleration response when the larger diameter effects are included.

Acceleration responses are output at every 5 μs which is the same as the recording interval of the experiments. Frequency domain responses are calculated by the Fast Fourier Transform (FFT) using the software, Altair Hyperview from the time domain response. Final results of time domain response are filtered using a low-pass filter. The frequency used for filtering is noted in the figures since cutoff frequency changes, depending on the structure type.

4.1.2 Effect of Applied Impact Forces

Different magnitudes of impact forces with variations in impact durations are used to study an effect of applied impact force on acceleration responses of the cylindrical structures. The different impact forces are applied as a half sine curve at the end of the short and long structural models. One primary focus of this study is the impact duration. By increasing the impact duration, an applied impact may interfere with the wave reflected back from the other end of the structure. The acceleration response affected by the interference between an applied impact and returning wave is studied. As reported by

Berman (2003), time resolution of loading function affects the response results showing a significant transient at each point in the input function. Therefore, an interval of input forces is determined by trial and error to assure time resolution does not affect the response. Impacts applied to the structures have the exact same impulses. This was achieved by altering the magnitude of impact forces based on the impact duration. The models used in this study duplicate the projectile and long bar used in the experimental simulation including the boundary conditions. Detailed description of applied impulses is given in the results section.

4.2 Results

4.2.1 Simulation of Experimental Condition

4.2.1.1 The Projectiles

Computational results of the projectile using the impact force obtained from the experiments are shown in Figures 4.2 and 4.3. Since projectiles were modeled with shared nodes between two different materials, effect of the bolt torque forces cannot be included in the model. Therefore, the force curve obtained experimentally using the structure fastened by 21 N-m torque are used to compute acceleration responses.

Figure 4.2 shows acceleration results obtained using the hard and medium tip impacts. Computational results (Figure 4.3) of FFT response of 'All Al' showed peaks at much higher frequencies (≈ 13,100 and 19,000 Hz) compared to the peaks from the experimental results (≈ 7,400 Hz for the 21 N-m torque case and 9,000 Hz for the 34 N-m torque cases). Therefore, acceleration responses were filtered at cutoff frequency of 20,000 Hz which are higher than one used for experimental results to include higher

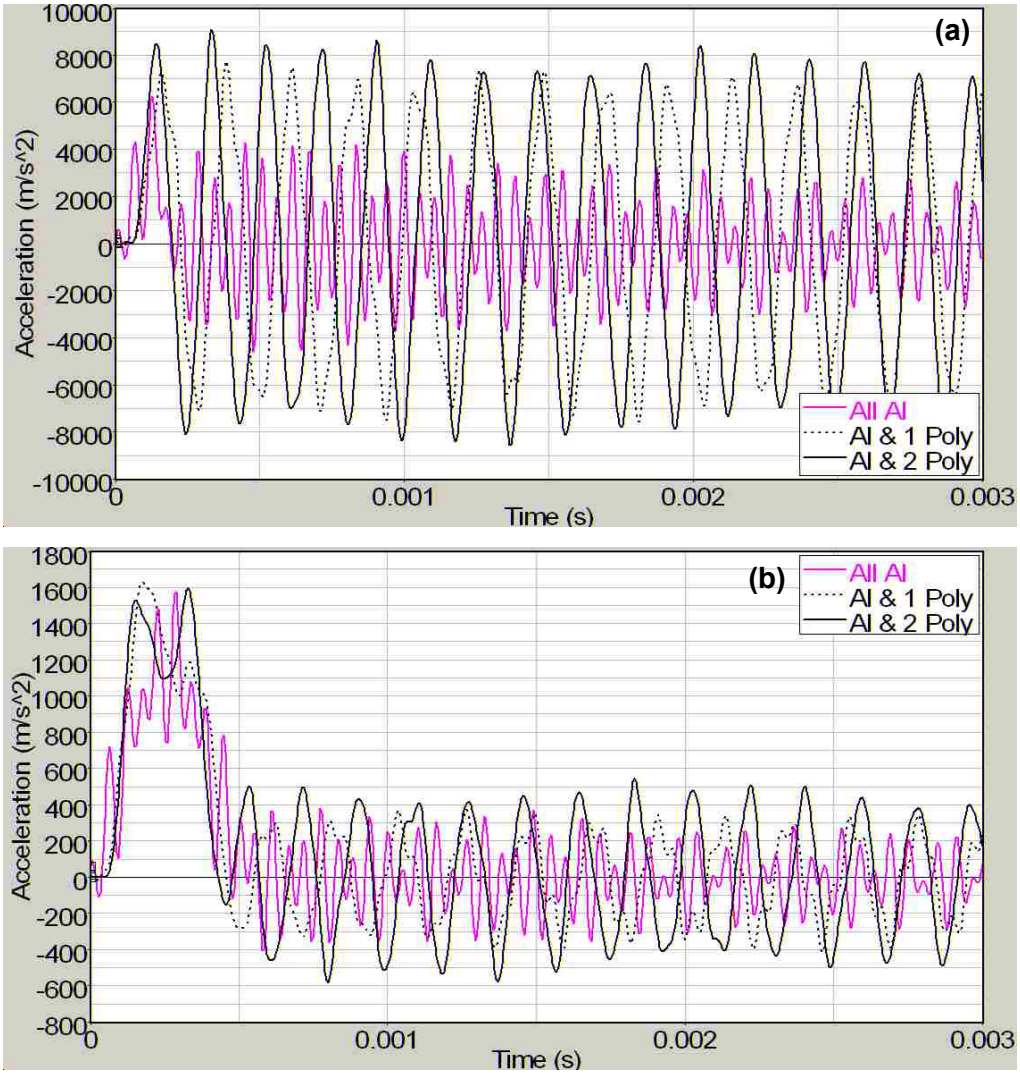

Figure 4.2 Computational results of acceleration responses of projectiles under impact loading using (a) hard and (b) medium tip impacts. 20,000 Hz cutoff frequency is used for low-pass filter.

excitation frequencies observed in the models. On the other hand, computational results of 'Al & 1 Poly' and 'Al & 2 Poly' had slightly lower excitation frequencies (≈ 4,800 and 5,600 Hz, respectively) compared to the experimental results.

Acceleration in 'All Al' had the lowest acceleration for both hard and medium tip impacts. However, the medium tip impact shows that the highest maximum acceleration

was observed in 'Al & 1 Poly', which was not the case for computational results of the hard tip impact and experimental results. Note that the differences in the maximum acceleration obtained from three different layer configurations using medium tip impacts were barely noticeable for both experimental and computational results.

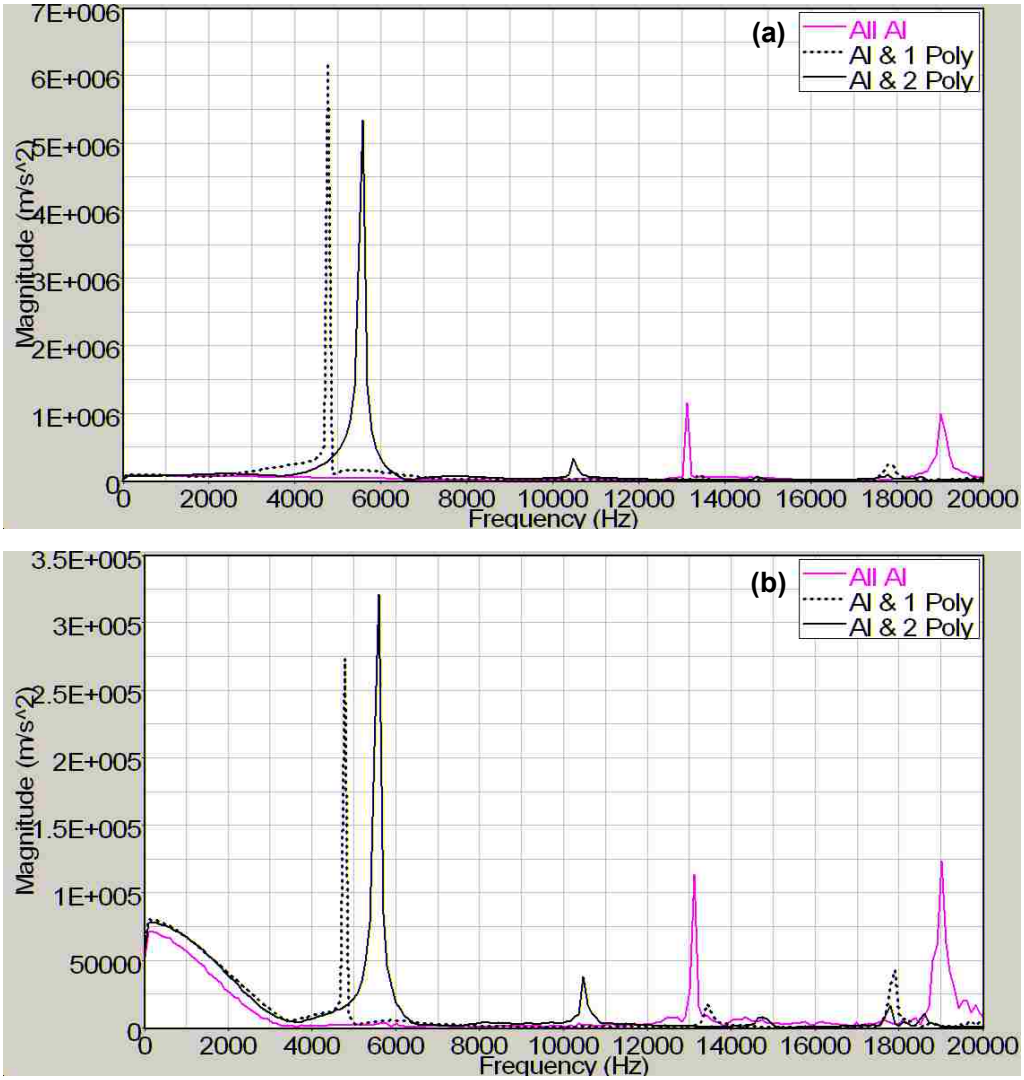

Figure 4.3 Computational results of FFT responses of projectiles under impact loading using (a) hard and (b) medium tip impacts.

4.2.1.2 The Long Bars

Computational results of the long structure are shown in Figures 4.4 and 4.5. As shown in Figure 4.4, both the hard and medium tip impacts showed significantly less accelerations in 'Al-Nylon-Al' case compared to 'Al-Al-Al'.

Similar to experimental result, highest peaks in the FFT response shifted to the lower

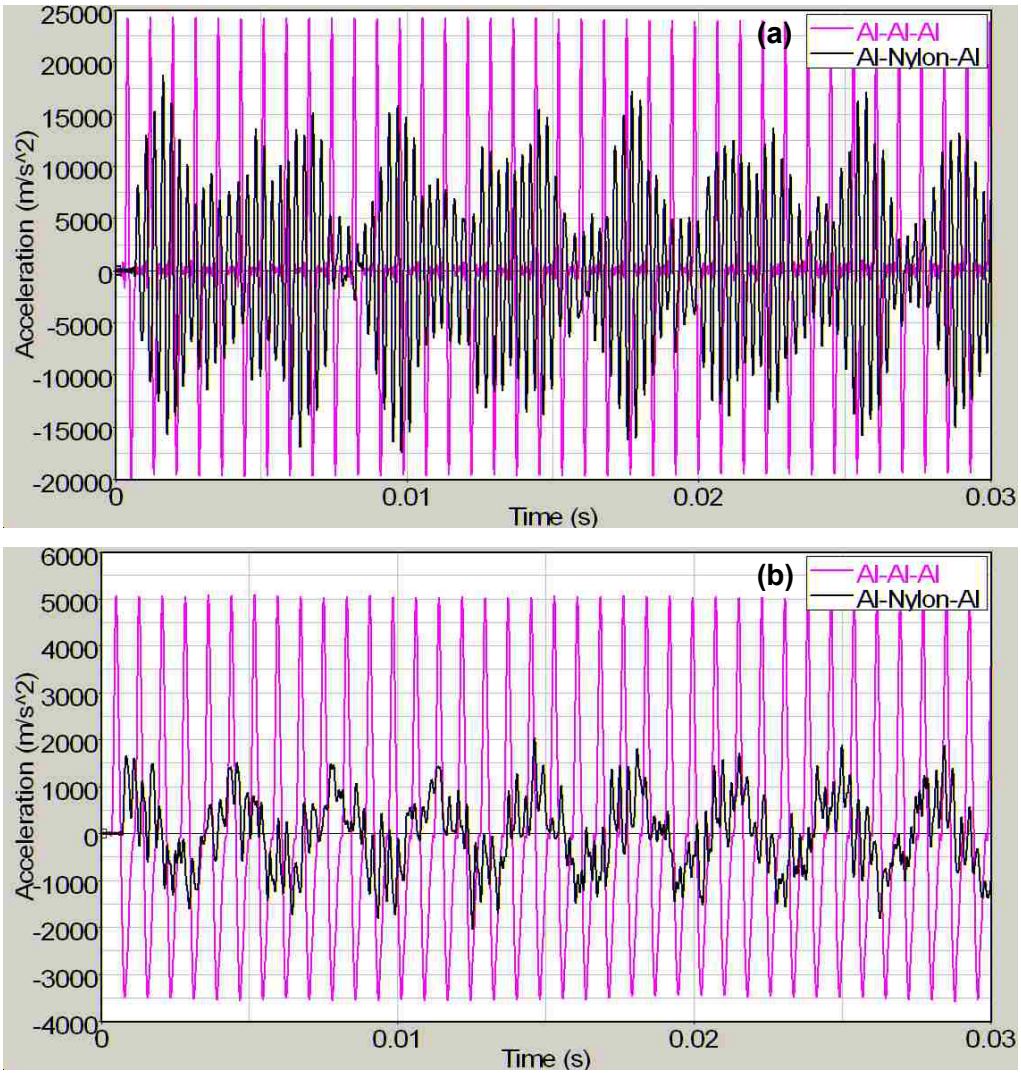

Figure 4.4 Computational results of acceleration responses of long bars under impact loading using (a) hard and (b) medium tip impacts. 10,000 Hz cutoff frequency is used for low-pass filter.

frequencies when impact tip was changed from hard to medium. However, excitation peaks were not exactly the same as experimental results even though differences were not as significant as those observed in short structures. The 'Al-Al-Al' case showed highest peaks at 2,622 and 1,305 Hz for the hard and medium tips, while 'Al-Nylon-Al' showed highest peaks at 3,542 and 298 Hz for hard and medium tips, respectively.

Other than the highest peaks, a number of intermediate peaks are noticeable in FFT

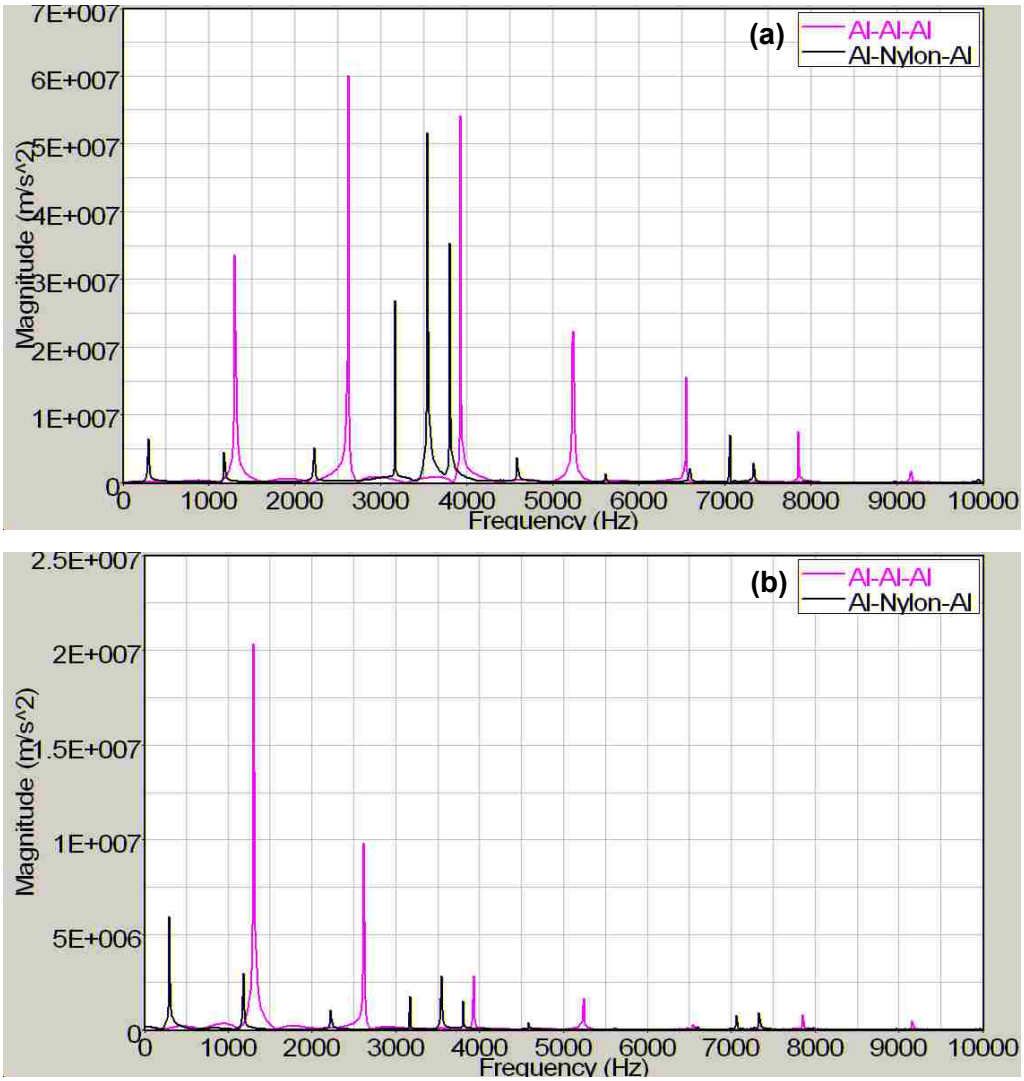

Figure 4.5 Computational results of FFT responses of long bars under impact loading using (a) hard and (b) medium tip impacts.

results up to nearly 10,000 Hz for 'Al-Al-Al' with the hard tip impact. Therefore, the acceleration responses obtained from computational results of the long structure were filtered with the cut-off frequency of 10,000 Hz for all the cases.

4.2.2 Effect of Applied Impact Forces

4.2.2.1 The Projectiles

Acceleration responses were obtained applying three different impact forces to the

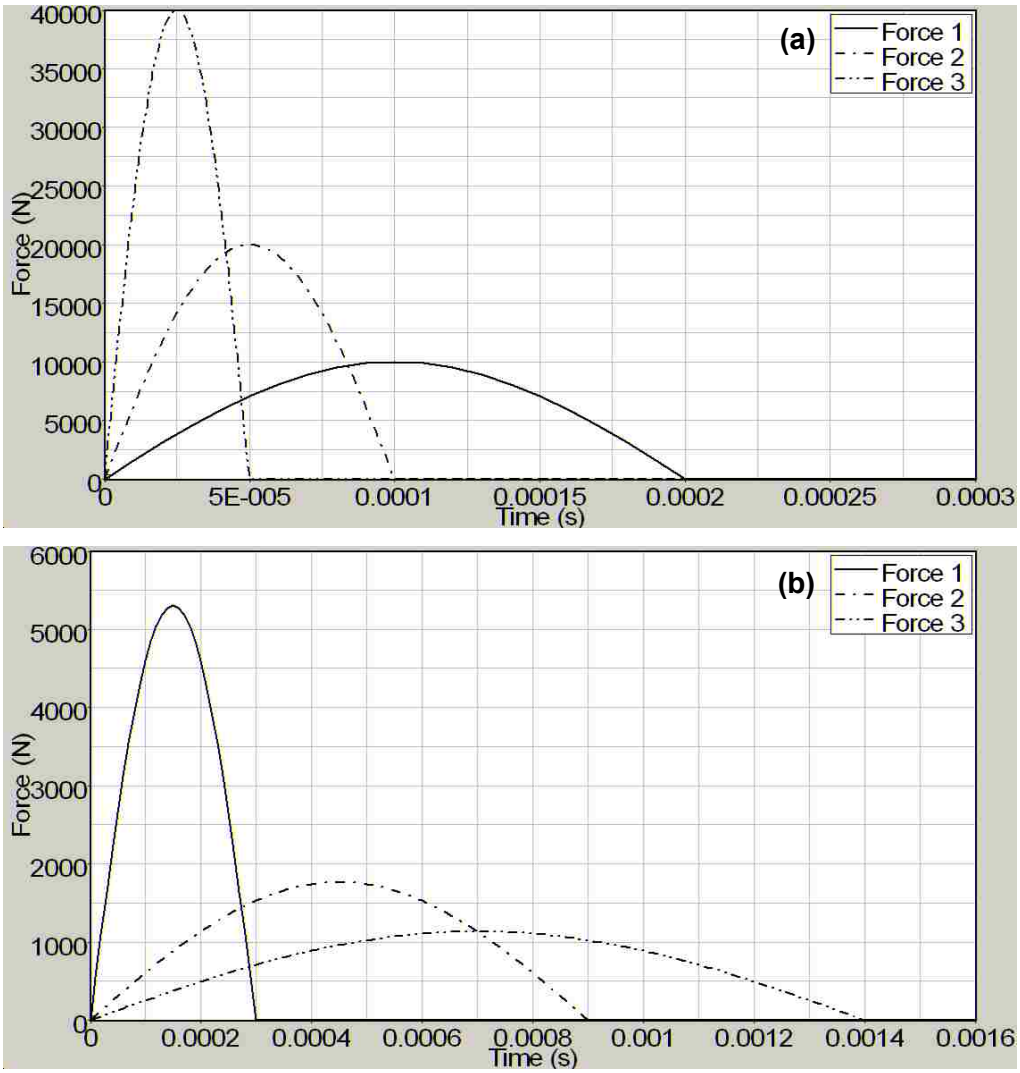

Figure 4.6 Applied impact used for (a) projectiles and (b) long bars to study effect of impact forces.

projectiles and long bars (Figure 4.6) in order to study effect of applied impact on acceleration responses. For the short structure, 'Force 1' has the maximum force of 10,000 N with applied duration of 0.0002 seconds similar to the experimental impact applied using the hard tip. The 'Force 2' has the applied impact duration long enough to interfere with the reflected back wave from the end of 'All Al' structure. The 'Force 3' has the shortest impact duration and the applied impact does not interfere with the reflected back wave from the end of any structure ('All Al', 'Al & 1 Poly' and 'Al & 2 Poly'). Maximum magnitude of 19,996 N for 'Force 2' and 39,992 N for 'Force 3' were calculated based on the impulse of 'Force 1'. All three forces have same impulse.

Whether the reflected wave interferes with the applied force or not, was looked at using material wave speed and length of the structure. Wave speeds of aluminum, polycarbonate and nylon are approximately 5,000 m/s, 1,500 m/s and 1,200 m/s, respectively. Single lap traveling times of 'All Al', 'Al & 1 Poly' and 'Al & 2 Poly' are about 0.00007, 0.0001 and 0.0001 seconds, respectively. Therefore, the impact with duration of 0.0002 seconds (Force 1) interferes with reflected wave in all three configurations while impact duration of 0.00005 seconds (Force 3) does not interfere in any of the cases.

As shown in Figure 4.7a, the acceleration results obtained from 'Force 1' duplicate closely to the experimental result. The lowest maximum acceleration was observed in 'All Al' followed by 'Al & 2 Poly' and 'Al & 1 Poly'. However, acceleration results of 'Force 2' showed that 'All Al' had the highest maximum acceleration followed by 'Al & 1 Poly' although differences in maximum accelerations of all three cases were small. Figure 16c shows acceleration response obtained by applying 'Force 3'. The order of

maximum accelerations was same as the results obtained from 'Force 2'. However, 'Force 3' showed significant differences between 'All Al' and 'Al & 2 Poly' while 'Al & 2 Poly' and 'Al & 1 Poly' showed almost the same maximum acceleration.

Figure 4.8 shows FFT response of three different applied forces. Results from all forces showed peaks at the exact same frequencies; however the magnitude of each peak was different. The highest peak was in 'Al & 1 Poly' closely followed by 'Al & 2 Poly' and significantly lower peak in 'All Al' when "Force 1' was applied to the structures (Figure 4.8a). In the case of 'Force 2', the highest peak was observed in 'All Al' followed by 'Al & 2 Poly' and 'Al & 1 Poly'. However, all the peaks were close to each other. As shown in Figure 4.8c, 'Force 3' showed distinctly higher peak in 'All Al' followed by 'Al & 2 Poly' and 'Al & 1 Poly'. Similar to 'Force 1' and 'Force 2', the difference in the magnitude of the peaks between 'Al & 2 Poly' and 'Al & 1 Poly' was small.

4.2.2.2 The Long Bars

The long bar model is also used to study the effect of applied impacts. Three applied forces, 'Force 1', 'Force 2' and 'Force 3' shown in Figure 4.6b are used to obtain the acceleration responses. 'Force 1' has the maximum force of 5,300 N with applied duration of 0.0003 seconds similar to the experimental impact applied using the hard tip. The 'Force 2' has the applied impact duration long enough to interfere with the reflected back wave from the end of 'Al-Al-Al'. Unlike the force applied to the short structure, 'Force 3' has the longest impact duration and the applied impact interferes with the reflected back wave from the ends of both 'Al-Al-Al' and 'Al-Nylon-Al'. Single lap traveling time of 'Al-Al-Al' is 0.0008 seconds while that of 'Al-Nylon-Al' is 0.0013 seconds. Therefore, the 'Force 3' impact, with impact duration 0.0014 seconds, interferes

with reflected wave for both cases. Magnitudes of 'Force 2' and 'Force 3' are 1,766 N and 1,135 N, respectively, which are calculated to have same impulse as 'Force 1'.

In the case of 'Force 1', acceleration was lower in 'Al-Nylon-Al' than that of 'Al-Al-Al', which is the same as the experimental result (Figure 4.9a). When the duration of impact force was increased such that the applied impact interferes with the reflected back wave from the other end of 'Al-Al-Al' structure but not 'Al-Nylon-Al', the acceleration of 'Al-Al-Al' was barely higher than that of 'Al-Nylon-Al' (Figure 4.9b). When the impact duration was further increased, 'Al-Nylon-Al' showed higher acceleration response than that of 'Al-Al-Al' (Figure 4.9c).

The highest peak in the FFT responses of 'Force 1' appeared at different frequencies compared to other two forces (Figure 4.10). The result of 'Force 1' had highest peaks at approximately 2,700 Hz and 1,350 Hz for 'Al-Al-Al' and 'Al-Nylon-Al', respectively, while 'Force 2' and 'Force 3' showed highest peaks at around 1,350 Hz ('Al-Al-Al') and 300 Hz ('Al-Nylon-Al'). Differences in excitation frequencies were also observed when the impact tip was changed from hard to medium tip in the experimental study. The magnitude of the highest peak was higher in 'Al-Al-Al' compared to 'Al-Nylon-Al' for 'Force 1' and 'Force 2' cases while 'Force 3' was opposite.

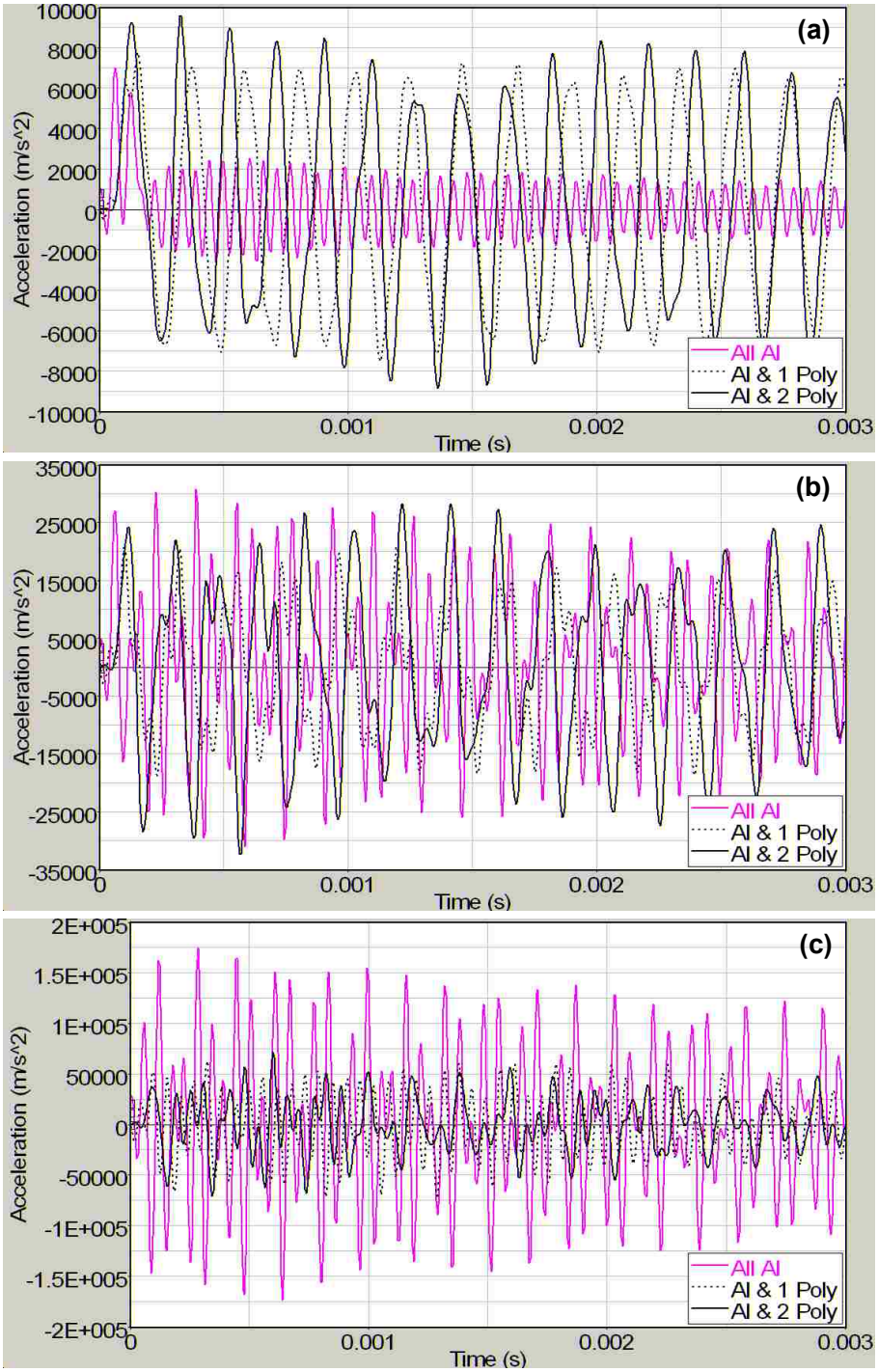

Figure 4.7 Computational results of acceleration responses obtained by applying three different impact forces to projectiles. Accelerations obtained using (a) Force 1; magnitude of 10,000 N with 0.0002 seconds impact duration, (b) Force 2; magnitude of 19,996 N with 0.0001 seconds impact duration and (c) Force 3; magnitude of 39,992 N with 0.00005 seconds impact duration. 20,000 Hz cutoff frequency is used for low-pass filter.

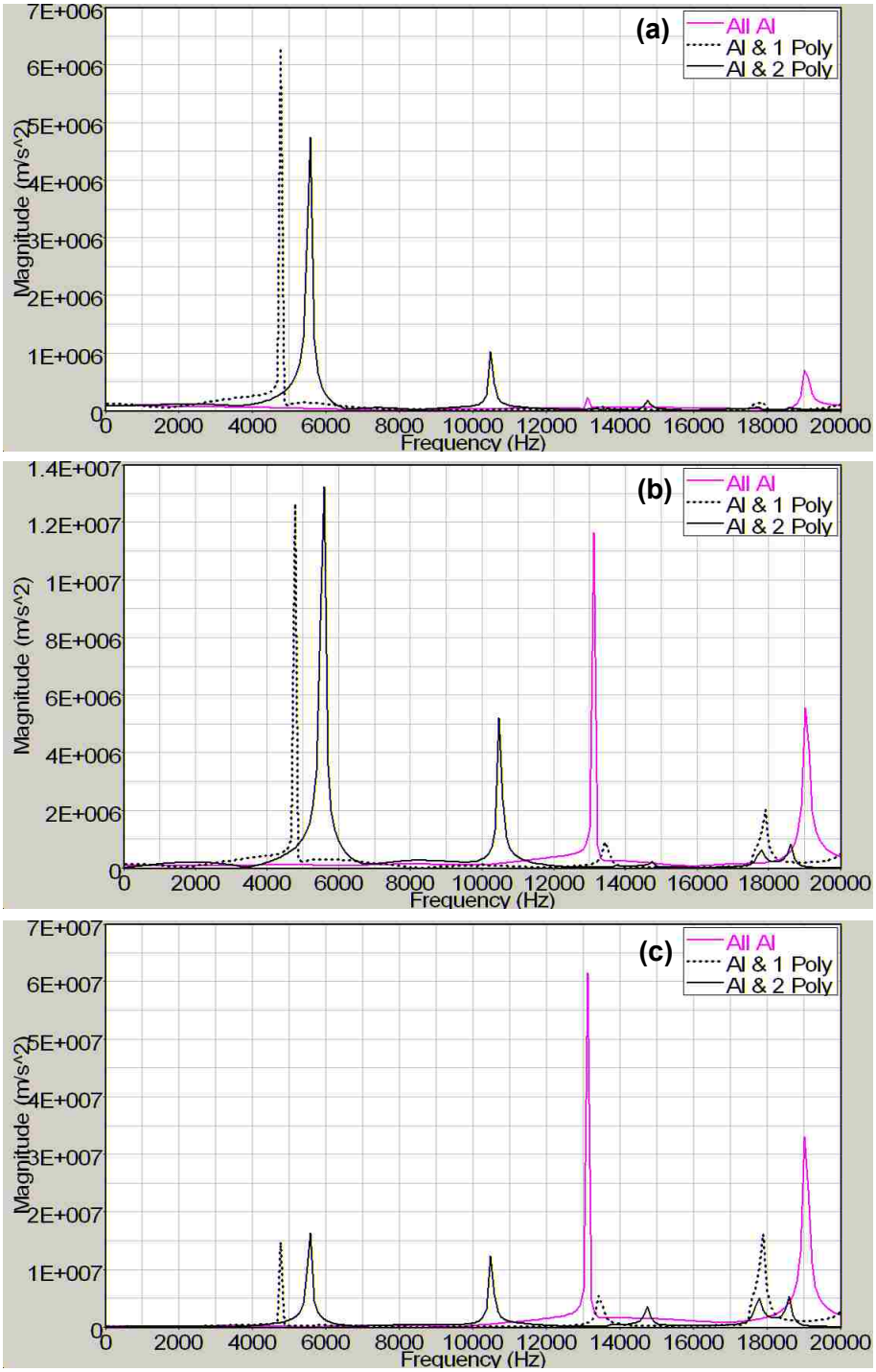

Figure 4.8 Computational results of FFT responses obtained by applying three different impact forces to projectiles. FFT responses obtained using (a) Force 1; magnitude of 10,000 N with 0.0002 seconds impact duration, (b) Force 2; magnitude of 19,996 N with 0.0001 seconds impact duration and (c) Force 3; magnitude of 39,992 N with 0.00005 seconds impact duration.

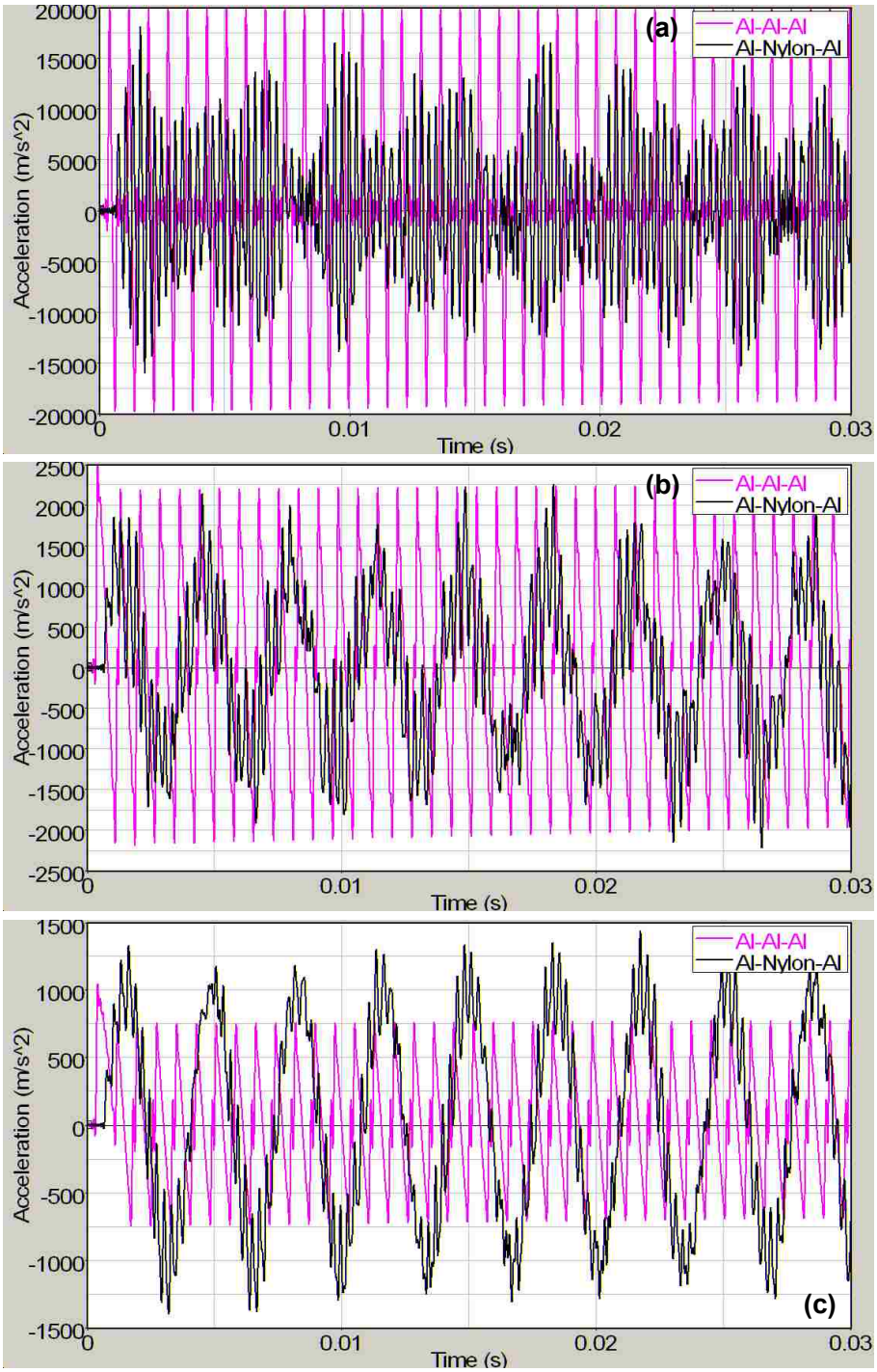

Figure 4.9 Computational results of acceleration responses obtained by applying three different impact forces to long bars. Acceleration responses are obtained using (a) Force 1; magnitude of 5,300 N with 0.0003 seconds impact duration, (b) Force 2; magnitude of 1,766 N with 0.0009 seconds impact duration and (c) Force 3; magnitude of 1,135 N with 0.0014 seconds impact duration. 10,000 Hz cutoff frequency is used for low-pass filter.

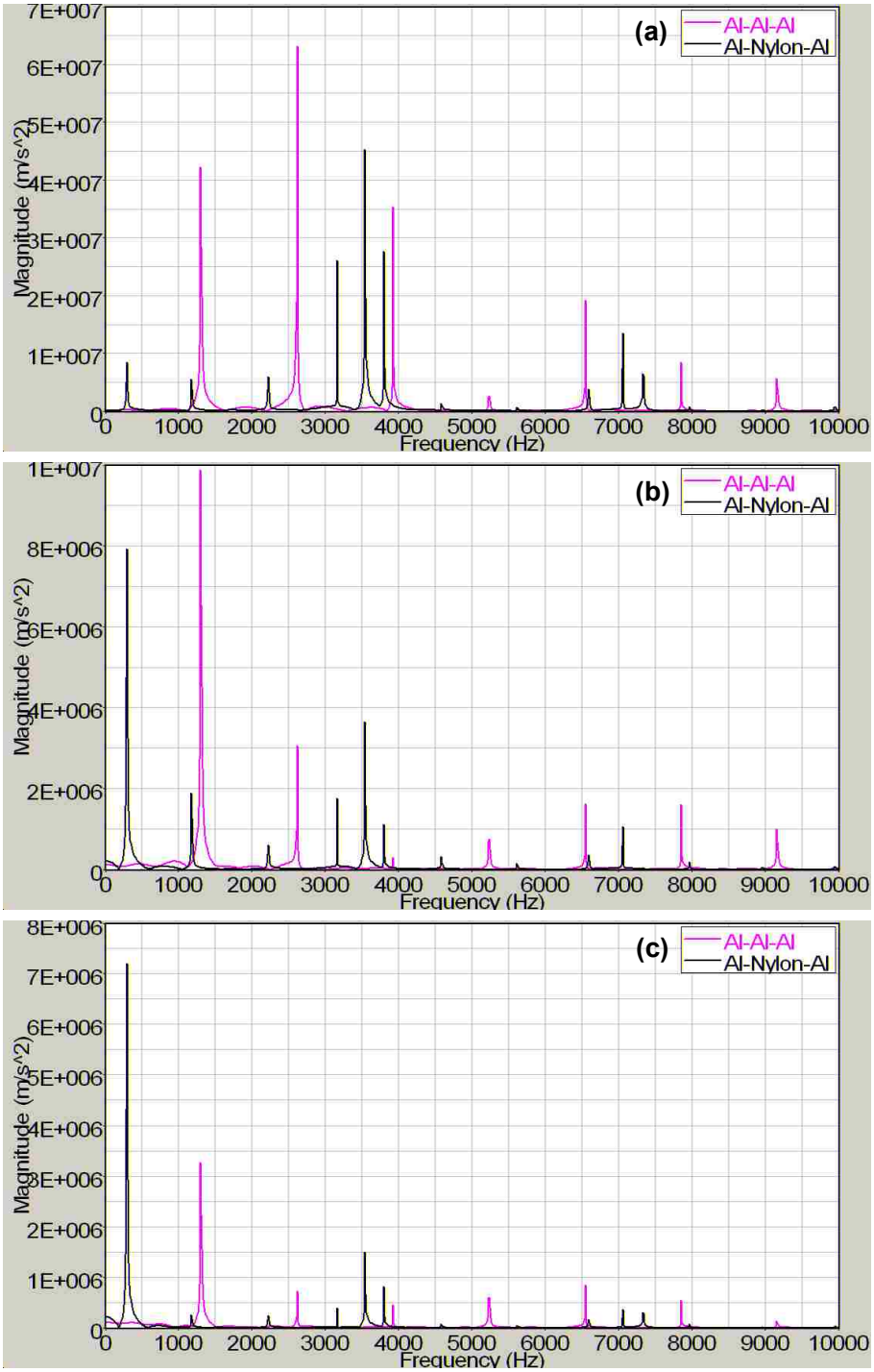

Figure 4.10 Computational results of FFT responses obtained by applying three different impact forces to projectiles. FFT responses are obtained using (a) Force 1; magnitude of 5,300 N with 0.0003 seconds impact duration, (b) Force 2; magnitude of 1,766 N with 0.0009 seconds impact duration and (c) Force 3; magnitude of 1,135 N with 0.0014 seconds impact duration.

4.3 Discussion

The computational results of projectiles and long bars showed similar accelerations compared to the experiments. One noticeable difference was that the experiments show clear damping effect in acceleration response while that was not the case in the simulations. The model used in the study did not include damping as well as bolts connections. The damping was not included in the model because the maximum damping ratio obtained from the experimental results was less than 2%. Therefore, the model does not have any material damping or physical means to reduce vibrations other than impedance mismatch. The other thing that needs to be pointed out was that the excitation frequencies in the short structures were significantly different between the simulation and experimental results, especially for 'All Al' case. This might be contributed by two factors. First, the material properties used in the simulations are reference values obtained from literature since exact values are not available. It is possible that some of the material properties might be slightly different compared to the ones used in the experiment. Especially, Young's modulus and density affect the excitation frequency. The second cause might be from the simplification of the model. Since the structures were modeled as simple one solid structure without bolts and with common nodes at the interface, that might be contributing to the differences in excitation frequencies. As Aoki (2004) reported, natural frequency is lower for the specimen with bolted joints compared to the one without bolted joints. The bolt effect is further demonstrated by the experimental results. When the torque was increased to tighten the bolts to assemble the experimental structures, peak frequencies in FFT response shifted to higher values. This phenomenon was also reported by Augustaitis et al. (2006). This reasoning was also supported by the

results obtained from our long structure data. Components of the long structure were directly fastened by thread rather than using the bolts. FFT response of the computational and experimental results of long structure showed only a slight difference in excitation frequencies.

Three different impact forces are applied in the projectiles and long bars model to verify the hypothesis (when an applied impact force interfere with the propagating wave, impedance mismatch does not help to reduce acceleration). In the experimental condition of the projectiles, the applied impact and the reflected wave interfered for all three cases, 'All Al', 'Al & 1 Poly' and 'Al & 2 Poly'. When the impact duration is reduced such that the applied impact and the propagating wave do not interfere, 'Al & 2 Poly' has the lowest acceleration closely followed by 'Al & 1 Poly'. 'All Al' clearly shows highest acceleration among these three configurations. In contrast to the projectile, the applied impact and the propagating wave did not interfere for both 'Al-Al-Al' and 'Al-Nylon-Al' in the experimental conditions of long bars and the results showed clear reduction in acceleration response of 'Al-Nylon-Al' compared to 'Al-Al-Al'. Therefore, the impact duration is increased to have interference between the applied impact and the propagating wave in the models. Simulation results clearly showed that when the applied impact and the propagating wave interfere, 'Al-Nylon-Al' have higher acceleration than that of 'Al-Al-Al'.

The other noticeable point is, when only one material structure has interference between the applied impact and the propagating wave, the acceleration results of one material and two material structures show almost the same magnitude for both projectile and long bar cases. In other words, a structure made of one material seems to be less

affected by interference between the applied impact and propagating wave. This may be explained by a number of propagating waves in a structure. A number of a propagating wave increases when the propagating wave encountered an interface. Therefore, a possibility of interference between an applied impact and a propagating wave increases. This might be one of the reasons that the difference in acceleration response between 'Al & 2 Poly' and 'Al & 1 Poly' was very small. Additionally, when there is an interface within a structure, a wave reflects back earlier at the interface than the structure made of one material. For instance, single lap travel time of 'All Al' is 0.07×10^{-3} seconds while 'Al & 1 Poly' and 'Al & 2 Poly' are 0.1×10^{-3} seconds. However, an interface between aluminum and polycarbonate for 'Al & 1 Poly' reflects wave at 0.01×10^{-3} seconds and for 'Al & 2 Poly' at 0.005×10^{-3} seconds. Therefore, not only a number of propagating wave increases but also the number of interferences between applied impact and reflected wave since wave can return quicker in 'Al & 1 Poly' or 'Al & 2 Poly' than 'All Al'. The further study is needed to clarify if interferences work toward increasing or attenuating effects in acceleration responses under different configurations.

Bibliography

Altair Engineering, Inc. (2004). Altair HyperWorks 7.0 [computer software]. Troy, Michigan.

Aoki, S. (2004). Dynamic characteristics of structure with bolted joint considering some factors. *ASME Pressure Vessels Piping Div Publ PVP* (2004 ASME/JSME Pressure Vessels and Piping Conference. San Diego, CA), 486, 143-149.

Augustaitis, V. K., Bučinskas, V. and Pauža, V. (2006). Application of Frequency Method for Defining Threaded Joint Tightening Degree. *Solid State Phenomena*, 113, 277-280.

Berman, M. S. (2003). The effect of transient loading discretization on a roatating disk using Lawrence Livermore National Laboratories' Dyna 3-D. *Army Research Laboratory*, ARL-MR-557.

Hallquist, J. O. (Comp.). (2005). LS-DYNA Theory manual. Livermore, California.

Livermore Software Technology Corporation (2003). LS-DYNA Keyword user's manual, Version 970, April.

Livermore Software Technology Corporation (2006). LS-DYNA [computer software]. Livermore, California.

CHAPTER 5

WAVE TRACING

In chapters 2 through 4, acceleration attenuation is studied in the projectiles and long bars. The attenuation seemed to occur when there is no interference between an applied impact and its reflected wave. Therefore, in this chapter, wave propagations in simple layered cylindrical structures are studied using the basic equations of wave propagation in layered media to verify the interference effects and compared with FEA results.

5.1 Method

Solid cylindrical structures with overall length of 203.2 mm and 101.6 mm diameter are used to study wave propagations in the axial direction of the cylinder. Six different configurations (Figure 5.1) are used for two main objectives. The first objective is to study the change in acceleration response in a single material or in two material combinations. Four structural configurations are analyzed which are constructed as follows: (1) all aluminum, (2) all polycarbonate, (3) aluminum at the two ends and polycarbonate at the middle, and (4) polycarbonate at two ends and aluminum at the middle. These configurations are designated: (1) Al, (2) Poly, (3) APA-2, and (4) PAP. Each end plate has 50.8 mm length and the middle plate has 101.6 mm length for both "APA-2" and "PAP" configurations. The second objective is to study the effect of various combinations of segmental lengths and their placement using aluminum, polycarbonate and aluminum. Here, three different layer conditions are used: (i) 25.4 mm aluminum followed by 101.6 mm polycarbonate and 76.2 mm aluminum, (ii) 50.8 mm aluminum, 101.6 mm polycarbonate and 50.8 mm aluminum, and (iii) 76.2 mm

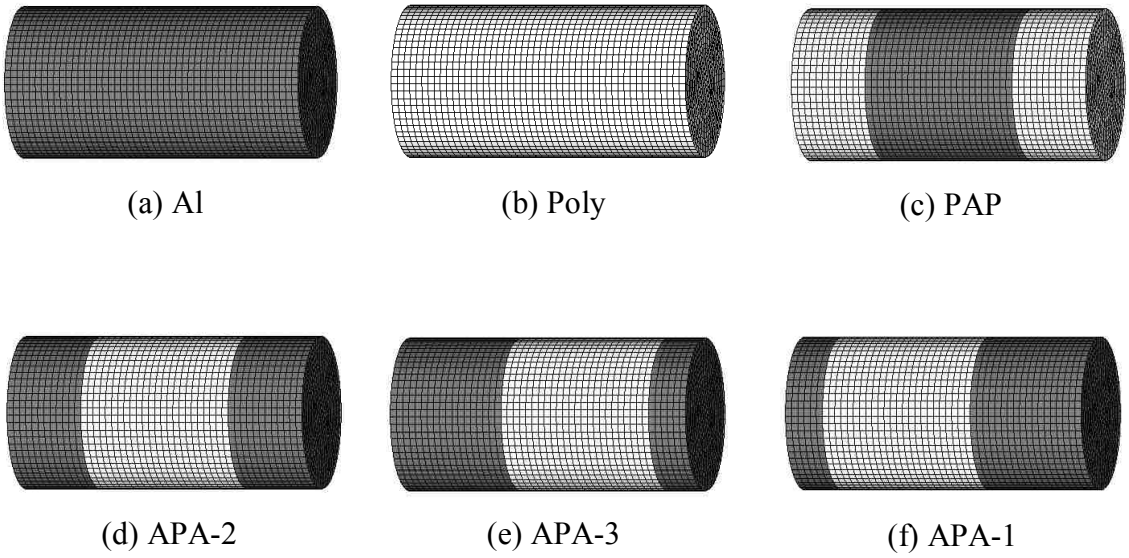

Figure 5.1 Six different configurations used in the study. Overall size of each structure is the same (203.2 mm length with 101.6 mm diameter). Dark and light colors represent aluminum and polycarbonate parts, respectively. An impact is applied at the left end of cylindrical structures made of (a) aluminum only, (b) polycarbonate only, (c) 50.8 mm polycarbonate, 101.6 mm aluminum and 50.8 mm polycarbonate, (d) 50.8 mm aluminum, 101.6 mm polycarbonate and 50.8 mm aluminum, (e) 76.2 mm aluminum, 101.6 mm polycarbonate and 25.4 mm aluminum, and (f) 25.4 mm aluminum, 101.6 mm polycarbonate and 76.2 mm aluminum.

aluminum, 101.6 mm polycarbonate and 25.4 mm aluminum. These configurations, (i), (ii) and (iii) are designated as "APA-1", "APA-2" and "APA-3", respectively. The first layer of the structure is referred to as the impact side. For instance, an impact is applied to the 25.4 mm aluminum layer when the "APA-1" structure is used.

Acceleration responses at the end of cylindrical structures are computed under impact load using the finite element software, LS-DYNA software (Livermore, 2006). The finite element analysis cases are conducted in the same manner as the long bar cases described in chapter 4. The differences are in the structure size, and the magnitude and duration of the impact forces. The cylindrical structure is modeled using 23,424 elements (eight-node solid hexahedron). Two different half sine curves are used to apply impacts; a low

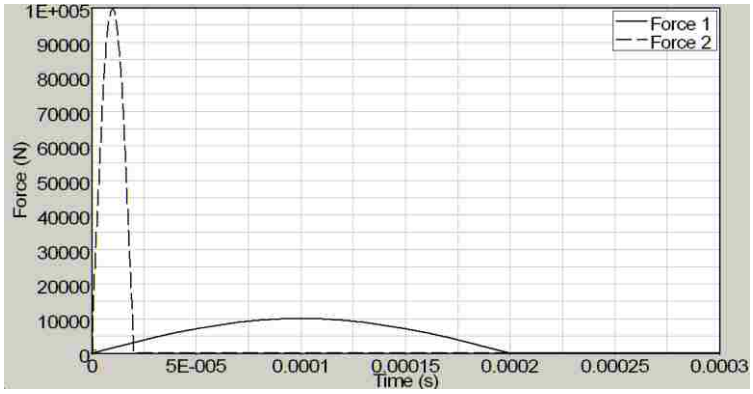

Figure 5.2 Two impact forces of equal $\int_0^{t_1} F(t)dt$ impulses used in the computational study. Force 1 has magnitude of 10,000 N with impact duration of 0.2 x 10^{-3} seconds and Force 2 has magnitude of 100,000 N with impact duration of 0.02 x 10^{-3} seconds.

magnitude force with long period (Force 1) and a high magnitude force with short period (Force 2). Both curves have the same impulse, $\int_0^{t_1} F(t)dt$, as shown in Figure 5.2.

Computational results obtained from finite element analysis are, then, compared with wave propagations obtained using equations given in following sections.

5.1.1 Reflection and Transmission at an Interfaces

Since acceleration at the face of the projectile is of interest, vibration traveling along the projectile is treated as longitudinal wave propagation in a rod. The equation of motion of longitudinal wave propagation can be expressed by Equation 5.1 assuming that plane transverse sections of the cylindrical structure remain plane during the passage of the wave, thus no shear wave effect.

$$\rho \frac{\partial^2 u}{\partial t^2} = E \frac{\partial^2 u}{\partial x^2} \qquad \text{Equation 5.1}$$

Where, ρ and E are the material density and Young's modulus, respectively. u is the displacement in x direction and t represents time. The wave propagates in the structure with the speed of $\sqrt{E/\rho}$. In order Equation 5.1 to be valid, the assumption must be that no transverse or shear waves are generated and the impulse generated waves travel axially while transverse and shear waves are negligible due to concentricity and to the axial nature of the impact force and its short duration. Meanwhile, if the wave encounters an interface, the part of the wave reflects back and the rest passes through the interface. If a wave with amplitude ξ_I in medium 1 encounters a boundary with medium 2, the amplitudes of the reflected and transmitted waves are respectively determined by Equation 1.1 and 1.2 as described in Chapter 1.

5.1.2 Acceleration Response in Undamped Spring-Mass System

In the case of undamped spring-mass system, the motion under a half-sine pulse excitation (Equation 5.2) is expressed as a second order differential equation, Equation 5.3 (Thomson, 1993).

$$\begin{aligned} F(t) &= F_0 \sin\frac{\pi t}{t_1} && \text{for } t < t_1 \\ &= 0 && \text{for } t > t_1 \end{aligned} \qquad \text{Equation 5.2}$$

$$\begin{aligned} \ddot{x} + \omega^2 x &= \frac{F_0}{m}\sin\frac{\pi t}{t_1} && \text{for } t < t_1 \\ &= 0 && \text{for } t > t_1 \end{aligned} \qquad \text{Equation 5.3}$$

The solution of the equation with the initial conditions $x(0) = \dot{x}(0) = 0$ is

$$\begin{aligned} \frac{xK}{F_0} &= \frac{1}{\frac{\tau}{2t_1} - \frac{2t_1}{\tau}}\left[\sin\frac{2\pi t}{\tau} - \left(\frac{2t_1}{\tau}\right)\sin\frac{\pi t}{t_1}\right] && \text{for } t < t_1 \\ &= \frac{1}{\frac{\tau}{2t_1} - \frac{2t_1}{\tau}}\left[\sin\frac{2\pi t}{\tau} + \sin 2\pi\left(\frac{t}{\tau} - \frac{t_1}{\tau}\right)\right] && \text{for } t > t_1 \end{aligned} \qquad \text{Equation 5.4}$$

$$\ddot{x} = \frac{4F_0\pi^2\left(-2t_1\sin\frac{2\pi t}{\tau}+\tau\sin\frac{\pi t}{t_1}\right)}{\tau K\left(\tau^2-4t_1^2\right)} \qquad \text{for } t < t_1$$

$$= \frac{8F_0t_1\pi^2\left(-\sin\frac{2\pi t}{\tau}+\sin\frac{2\pi\left(-t+t_1\right)}{\tau}\right)}{\tau K\left(\tau^2-4t_1^2\right)} \qquad \text{for } t > t_1$$

Equation 5.5

where, x is deformation, ω and τ are the natural frequency and period, F_0 and t_1 are the maximum force and impact duration of the excitation pulse and m is the mass of the system in the case of a cylindrical structure. The stiffness of the system, K is calculated by following equation;

$$K = \sqrt{AE/L} \qquad \text{Equation 5.6}$$

where, A and L are the circular area and length of the cylindrical structure, respectively, and E is the Young's modulus. Acceleration of the system (Equation 5.5) is obtained by differentiating Equation 5.4 twice.

5.2 Results

5.2.1 Finite Element Analysis

5.2.1.1 Effect of Material Combinations

Figure 5.3 shows acceleration responses computed at the end of four different configurations of the cylindrical structures shown in Figure 5.1. Impact force of magnitude of 10,000 N and 0.2 x 10^{-3} seconds impact duration were applied to the cylindrical structures (Force 1 in Figure 5.2). Four different material combinations are "Al", "Poly", "APA-2" and "PAP". The highest magnitude of acceleration response, 90,172 m/s^2, was observed in "Poly" followed by "PAP" (66,647 m/s^2). The other two configurations, "Al" and "APA-2", had 8,898 and 8,727 m/s^2 maximum accelerations

which were approximately ten times lower than the acceleration response of "Poly" and "PAP" shown in Figure 5.3. In this analysis, it is very important to note that a comparison between the acceleration responses of "Al" and "APA2" show that while the maximum acceleration magnitude are similar, the mitigation of high frequencies in "APA2" is quite obvious which is one of the principal objectives of this research, given their damage to electronic components in smart projectiles.

Figure 5.4 shows acceleration responses obtained using the same configurations as Figure 5.3. However, the applied impact is ten times higher in magnitude (100,000 N) with ten times shorter impact duration (0.02 x 10^{-3} seconds) having the same $\int_0^{t_1} F(t)dt$ impulse as the first impact, Force 1. The force is shown as Force 2 in Figure 5.2. The order of maximum acceleration was same as the one obtained using Force 1. However, the noticeable difference between the two impact forces was observed in the maximum accelerations. When Force 2 was used, "Poly" had the highest maximum acceleration of approximately 2.38 x 10^6 m/s^2 while "PAP" and "Al" had approximately twice lower than that of "Poly" (approximately 1.17 x 10^6 m/s^2 for "PAP" and 1.05 x 10^6 m/s^2 for "Al"). Maximum acceleration in "APA-2" was about 0.48 x 10^6 m/s^2, which was approximately five times lower than that of "Poly". It is also important to note that the peak frequencies in "APA2" of 0.48 x 10^6 m/s^2 were reduced to about one forth, 0.12 x 10^6 m/s^2, in 0.75 x 10^{-3} seconds compared to more than 5.0 x 10^{-3} seconds for "Al" showing much faster attenuation of high frequencies and acceleration magnitudes. Again, this is very important factor in the reduction of damage to electronic components in projectiles. While "PAP" does not show reduction of acceleration peaks, it shows the all-

important drastic reduction in the damaging high frequencies, thus allowing the designer of the projectile to tailor the layering according to the design requirement.

5.2.1.2 Effect of Material Length

Material order, aluminum, polycarbonate and aluminum, are used to study acceleration changes based on the material length. Three configurations, "APA-1", "APA-2" and "APA-3" are used to compare the acceleration responses. When Force 1 (10,000 N with 0.02 x 10^{-3} seconds impact duration) was used, accelerations in all three configurations are similar to each other as shown in Figure 5.5. Maximum accelerations of "APA-1", "APA-2" and "APA-3" are 7,629, 8,727, and 7,464 m/s^2, respectively. When Force 2 which is a higher magnitude and a shorter impact duration than Force 1, was applied to the three cylindrical configurations, differences in maximum accelerations were more pronounced. The highest maximum acceleration was observed in "APA-2" (≈ 478,980 m/s^2). The other two configurations had maximum accelerations of 196,540 m/s^2 for "APA-1" and 220,960 m/s^2 for "APA-3", showing an acceleration mitigation of more than 50 % and a much faster attenuation of accelerations.

5.2.2 Wave Propagations

5.2.2.1 Wave Tracing

Simple calculations are carried out using the basic theory described in the preceding section to relate the computational results with wave propagation phenomena. Material wave speeds and impedances of aluminum and polycarbonate were calculated based on the material properties shown in Table 1. The transmission and reflection coefficients from aluminum to polycarbonate layers are calculated as 0.22 and -0.78, respectively, using Equations 5.2 and 5.3. Similarly, coefficients from polycarbonate to aluminum are

1.78 for transmission and 0.78 for reflection. Which coefficients apply to which layer condition are shown in Figure 5.7.

Wave propagations in six different configurations are traced using the coefficients shown above and results are shown in Figures 5.8 to 5.18. The horizontal direction in the figures shows the length of cylindrical structure and vertical direction shows time. A wave starts propagating as the impact is applied on the left side of the structure, and propagating waves are shown as lines in the horizontal direction. The numbers in the figures represent transmitted, reflected or combination of both waves calculated based on the applied impact shown in the left side of figures. Positive values indicate compressive wave and negative tensile. For instance, Figure 5.10 shows the wave tracing of "APA-2". When 1.56×10^3 N force is applied at the left side of the structure, the wave starts propagating in the first aluminum layer and encounters the interface between aluminum and polycarbonate layers. At this point, 22% of propagating wave (0.34×10^3 N) transmits to the second polycarbonate layer and -78% (-1.22×10^3 N) reflects back into the first aluminum layer.

Same as computational study, two half-sine forces, Force 1 and Force 2, are considered, Force 1 as 10,000 N maximum magnitude with impact duration of 0.2×10^{-3} seconds and Force 2 as 100,000 N maximum magnitude with impact duration of 0.02×10^{-3} seconds.

5.2.2.1.1 Effect of Material Combinations

Figures 5.8 and 5.9 are for "Al" and "Poly" cases, respectively, under the action of Force 1. Since waves can propagate much faster in aluminum than in polycarbonate, the propagating waves return to the initiation point (at the point of impact) after about 0.08 x

10^{-3} seconds over a total length of eight inches and start to interfere with the applied impact. For the "Poly" case, waves return to the original point after about 0.2 x 10^{-3} seconds. Therefore the impact will be over by the time a wave reflects back to the impact point, thus there will be no interference. As a result, "Al" experienced the maximum wave amplitude of 16.18 x 10^3 N which is larger than the maximum magnitude of applied impact, 10.0 x 10^3 N, while "Poly" showed the maximum wave amplitude of 10.0 x 10^3 N. Figure 5.10 shows wave tracing of "APA-2" under the action of Force 1. In this case, a propagating wave started reflecting back immediately to the starting point when the wave reached the first interface between aluminum and polycarbonate layers. Since the first aluminum layer is much shorter than the "Al" case, the wave reflects back quickly. As a result, interference between the applied impact and reflected back wave starts early. The reflection coefficient at the interface between aluminum and polycarbonate has a negative sign (polarity changes after reflection). However the reflection coefficient at the free ends also has a negative sign. Therefore, the applied impact and reflected wave have the same polarity resulting in the addition of their amplitudes. Even though the reflected and transmitted waves at the interfaces have lower magnitudes than the original wave, in this case between the reflected wave and the impact wave interference increases the magnitude of the wave. Consequently, the maximum wave reaching the right end significantly increased to 43.34 x 10^3 N. On the other hand, when "PAP" was used with a half-sine curve impact, the maximum wave reaching to the right end decreased to 5.46 x 10^3 N (Figure 5.11). When a polycarbonate layer comes first, reflected wave at the first interference has the same sign as the incident wave. Therefore, when interferences started

between applied impact and reflected wave at the free end, impact and the reflected wave have opposite signs which results in reduction of magnitude of propagating wave.

Wave tracing shown in Figures 5.12 to 5.14 are obtained using Force 2 (100,000 N with 0.02 x 10^{-3} seconds impact duration). Since the impact is applied with much shorter period than that of Force 1, there is no interference between reflected wave and applied impact. Therefore, changes in propagating wave occurs only at the interfaces resulting in slight reduction in the maximum magnitude of the waves reaching the right end of "APA-2" (Figure 5.12) and "PAP" (Figure 5.14). There are no magnitude changes in propagating wave of "Al" and "Poly" (Figure 5.12) since there are no interfaces in those two configurations. The maximum magnitude of wave for "APA-2" was 89.34 x 10^3 N and for "PAP" was 97.00 x 10^3 N.

5.2.2.1.2 Effect of Material Length

Figures 5.14 and 5.15 show wave tracing of "APA-1" and "APA-3", respectively, using a half-sine curve impact with 0.2 x 10^{-3} seconds impact duration. Since the first layer of "APA-1" is shorter than that of "APA-3", the interference between applied impact and reflected wave in "APA-1" starts slightly earlier than in "APA-3". As mentioned earlier, when the reflected wave interferes with an applied impact in the order of aluminum and polycarbonate, two waves show constructive interference and increase magnitude of propagation. Therefore, increasing interference resulted in slightly higher maximum magnitude of wave in "APA-1" (43.21 x 10^3 N) compared to "APA-3" (43.03 x 10^3 N). On the other hand, when Force 2 (shorter impact duration) was applied, "APA-1" showed lower maximum magnitude of wave than that of "APA-3" (Figures 5.17 and 5.18). The maximum magnitude of waves in "APA-1" and "APA-3" were 49.13 x 10^3 N

and 54.42 x 10^3 N, respectively. When wave transmits from polycarbonate to aluminum layer, magnitude of wave increases significantly because of the transmission coefficient. Therefore, it is better to have smaller magnitude of transmitted waves from polycarbonate to aluminum layer in order to reduce waves. On the other hand, longer third layer helps to reduce the reflected wave at the end of the cylinder which interferes with the transmitted wave from polycarbonate to aluminum, causing an increase in the propagating waves by adding up two waves. Since "APA-3" has shorter third layer than "APA-1", "APA-3" has more propagating waves in the third layer because of increase in reflections. As a result, "APA-3" increases the maximum wave.

When "APA-2" was used, the maximum magnitude of wave reached to the end was much higher than that of "APA-1" and "APA-3" when there is no interference between the applied impact and reflected wave. This is caused by the interference between reflected and transmitted waves at the interfaces. At both interfaces (between layers one and two, and two and three), "APA-2" always interfere with other reflected or transmitted waves since waves reach at the same time. However, "APA-1" and "APA-3" do not always interfere at both interfaces. Therefore, "APA-2" has apparently higher maximum magnitude of wave. When there is an interference between the applied impact and reflected wave, "APA-2" showed higher maximum magnitude of wave but it was not as high as the case without interference.

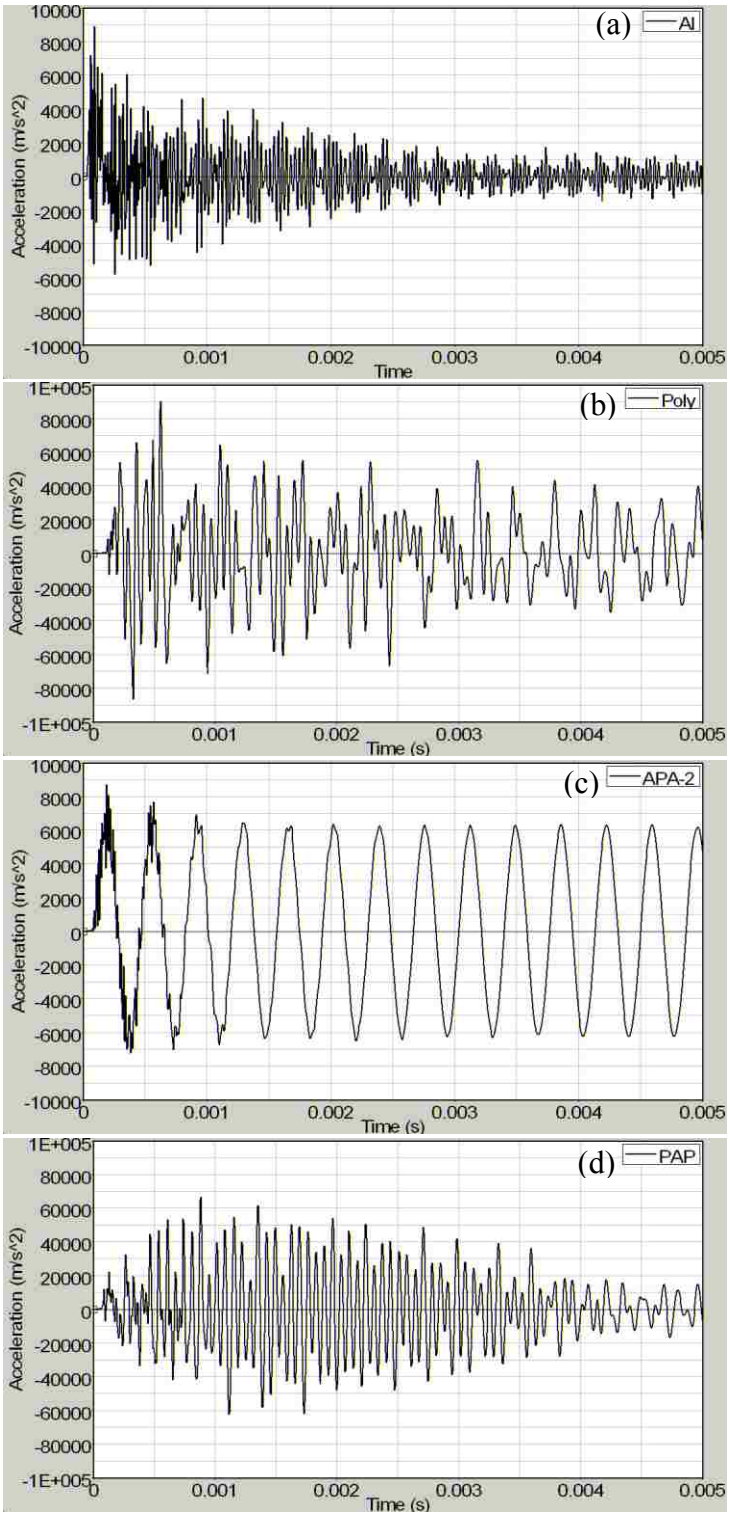

Figure 5.3 Acceleration responses of four different cylindrical configurations using a half-sine impact force magnitude of 10,000 N with impact duration of 0.2 x 10^{-3} seconds. The time acceleration plots are obtained using cylindrical structures made of (a) aluminum, (b) polycarbonate, (c) aluminum ends with polycarbonate at the middle and (d) polycarbonate with aluminum at the middle.

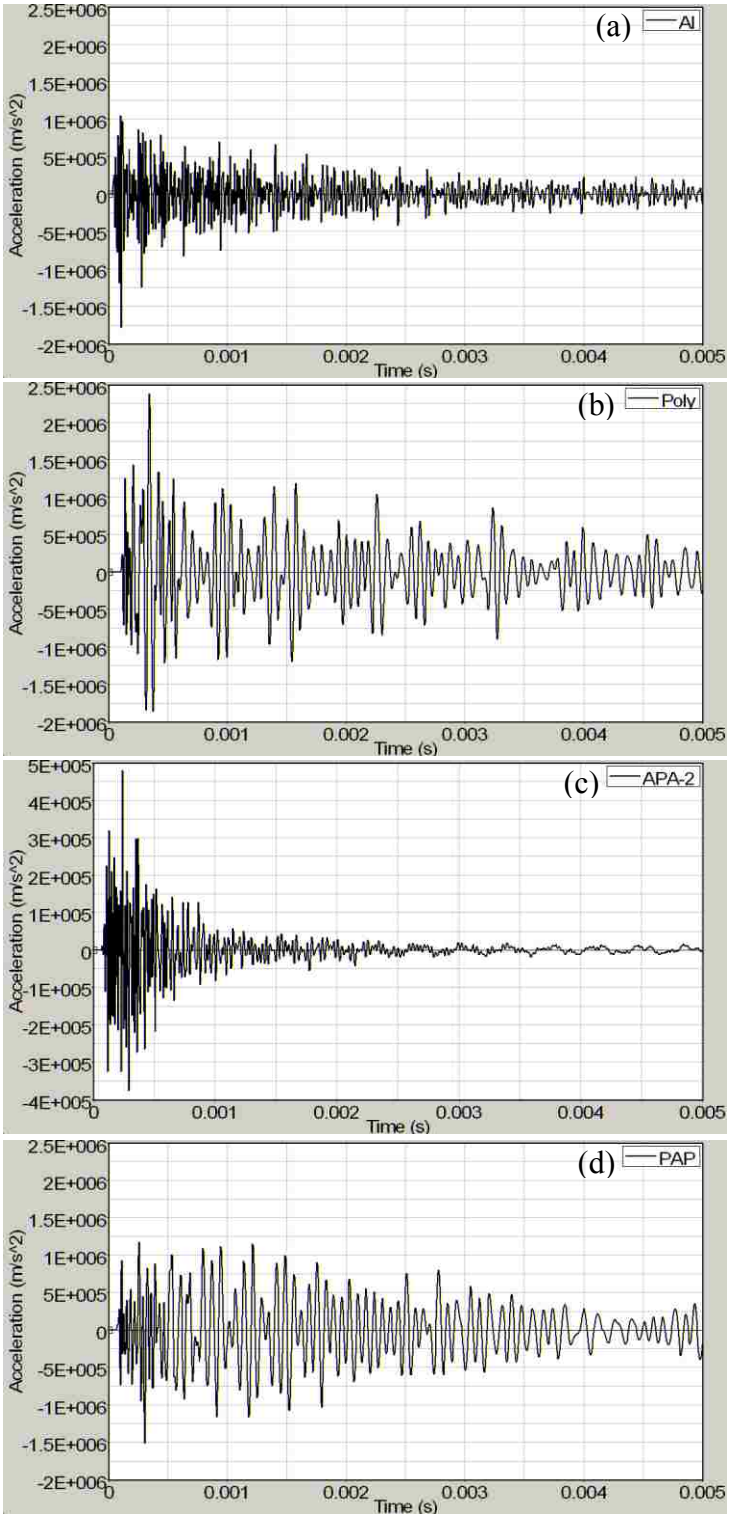

Figure 5.4 Acceleration responses of four different cylindrical configurations using a half-sine impact force magnitude of 100,000 N with impact duration of 0.02 x 10^{-3} seconds. The four acceleration plots are obtained using cylindrical structures made of (a) aluminum, (b) polycarbonate, (c) aluminum ends with polycarbonate at the middle and (d) polycarbonate ends with aluminum at the middle.

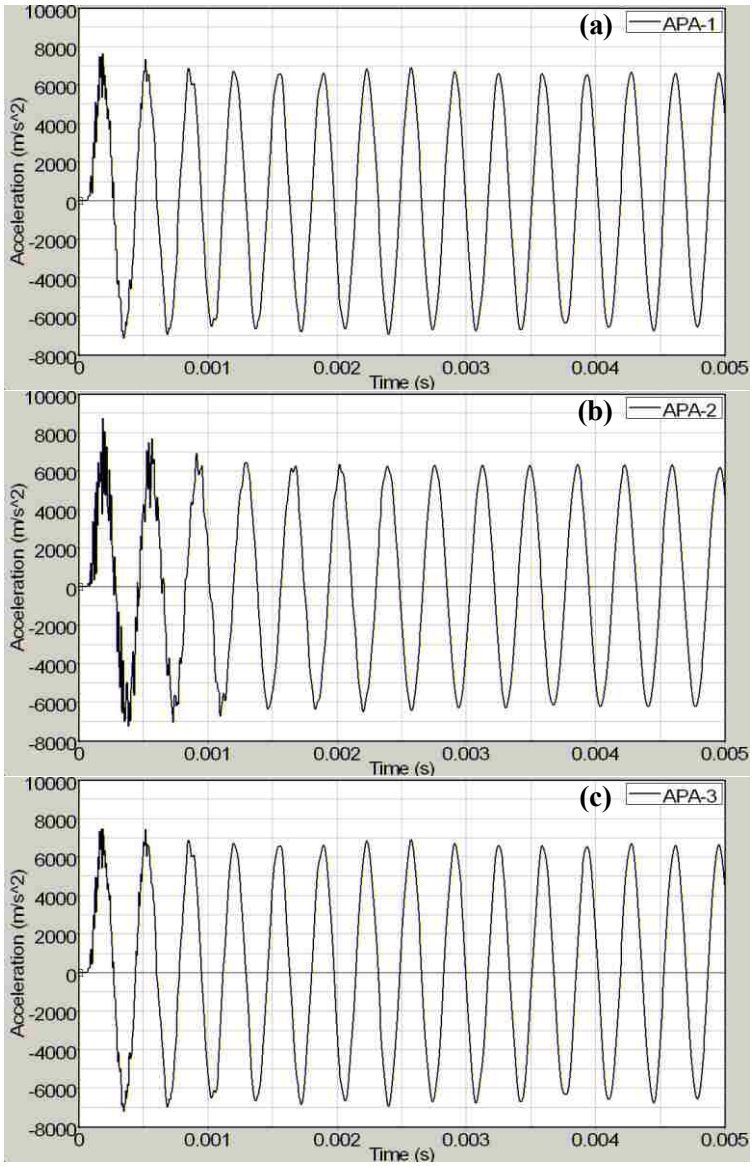

Figure 5.5 Acceleration responses obtained applying a half-sine impact of 10,000 N with 0.2 x 10^{-3} seconds impact duration. The three acceleration plots are obtained using the layered structure made of (a) 25.4 mm aluminum, 101.6 mm polycarbonate and 76.2 mm aluminum, (b) 50.8 mm aluminum, 101.6 mm polycarbonate and 50.8 mm aluminum, and (c) 25.4 mm aluminum, 101.6 mm polycarbonate and 76.2 mm aluminum.

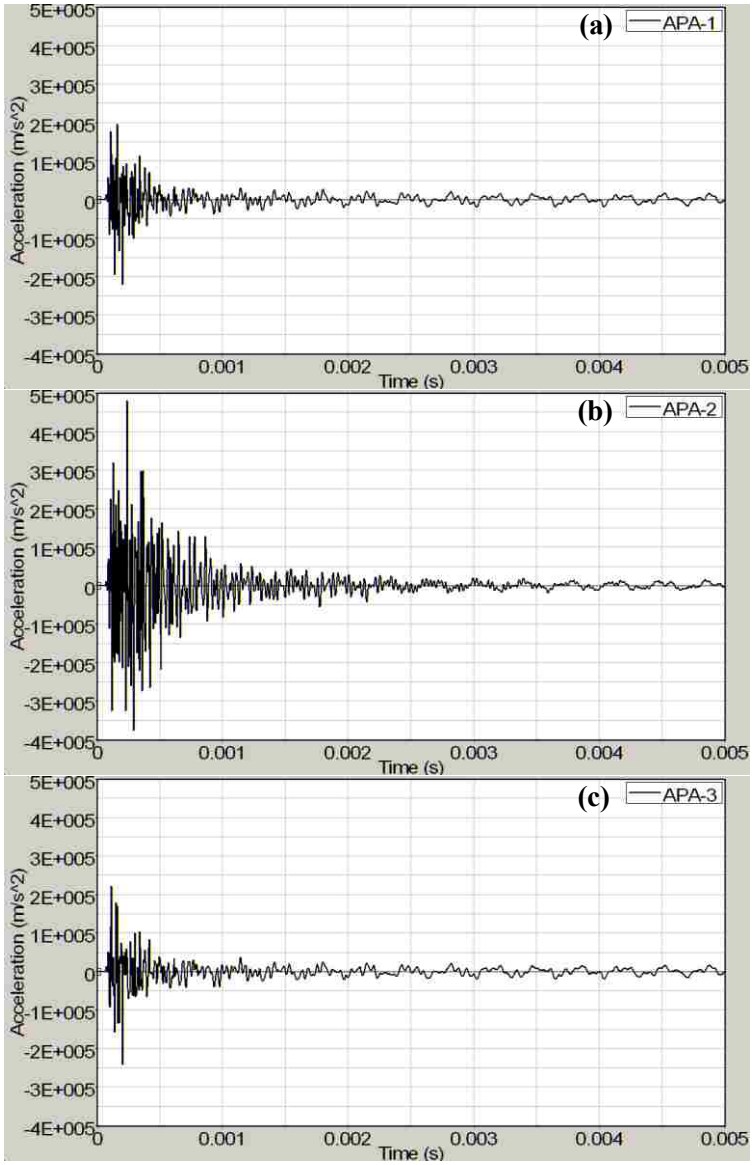

Figure 5.6 Acceleration responses obtained applying a half-sine impact of 100,000 N with 0.02 x 10^{-3} seconds impact duration. The three acceleration plots are obtained using the layered structure mode of (a) 25.4 mm aluminum, 101.6 mm polycarbonate and 76.2 mm aluminum, (b) 50.8 mm aluminum, 101.6 mm polycarbonate and 50.8 mm aluminum, and (c) 25.4 mm aluminum, 101.6 mm polycarbonate and 76.2 mm aluminum.

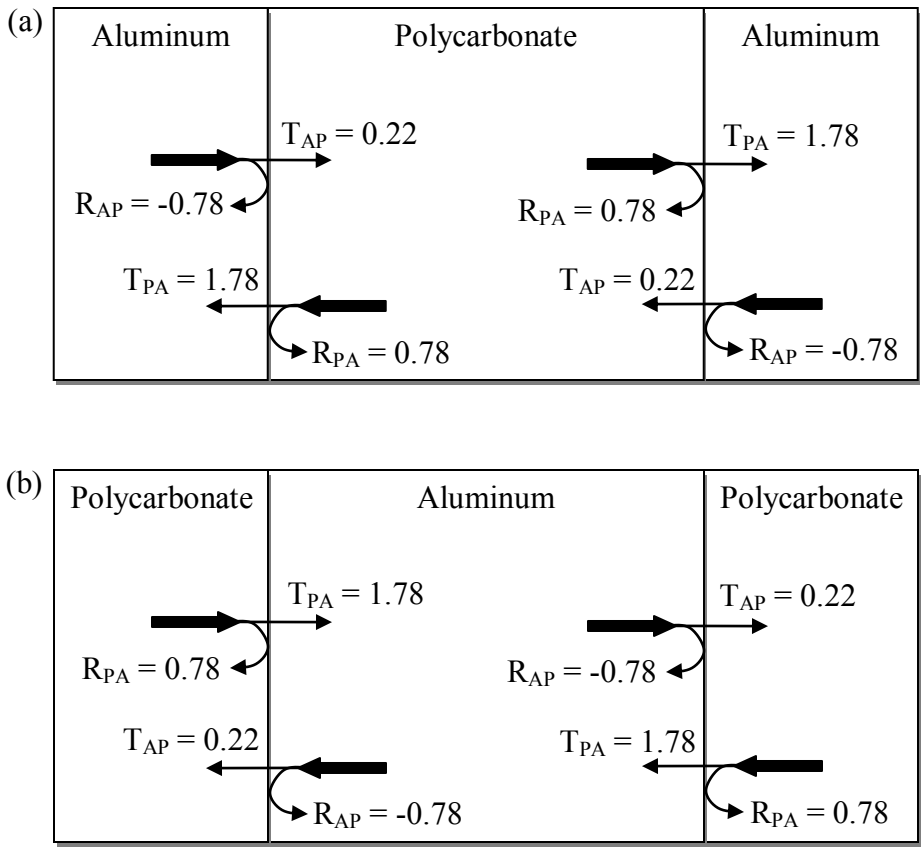

Figure 5.7 Transmission and reflection coefficients for (a) aluminum-polycarbonate-aluminum and (b) polycarbonate-aluminum-polycarbonate layer configurations. T_{AP} and T_{PA} represents transmission coefficient from aluminum to polycarbonate and polycarbonate to aluminum, respectively. Similarly, R_{AP} represents reflection coefficient of wave which propagates aluminum layer and reflects at the interface between aluminum and polycarbonate and R_{PA} is reflection coefficient of the opposite layer condition.

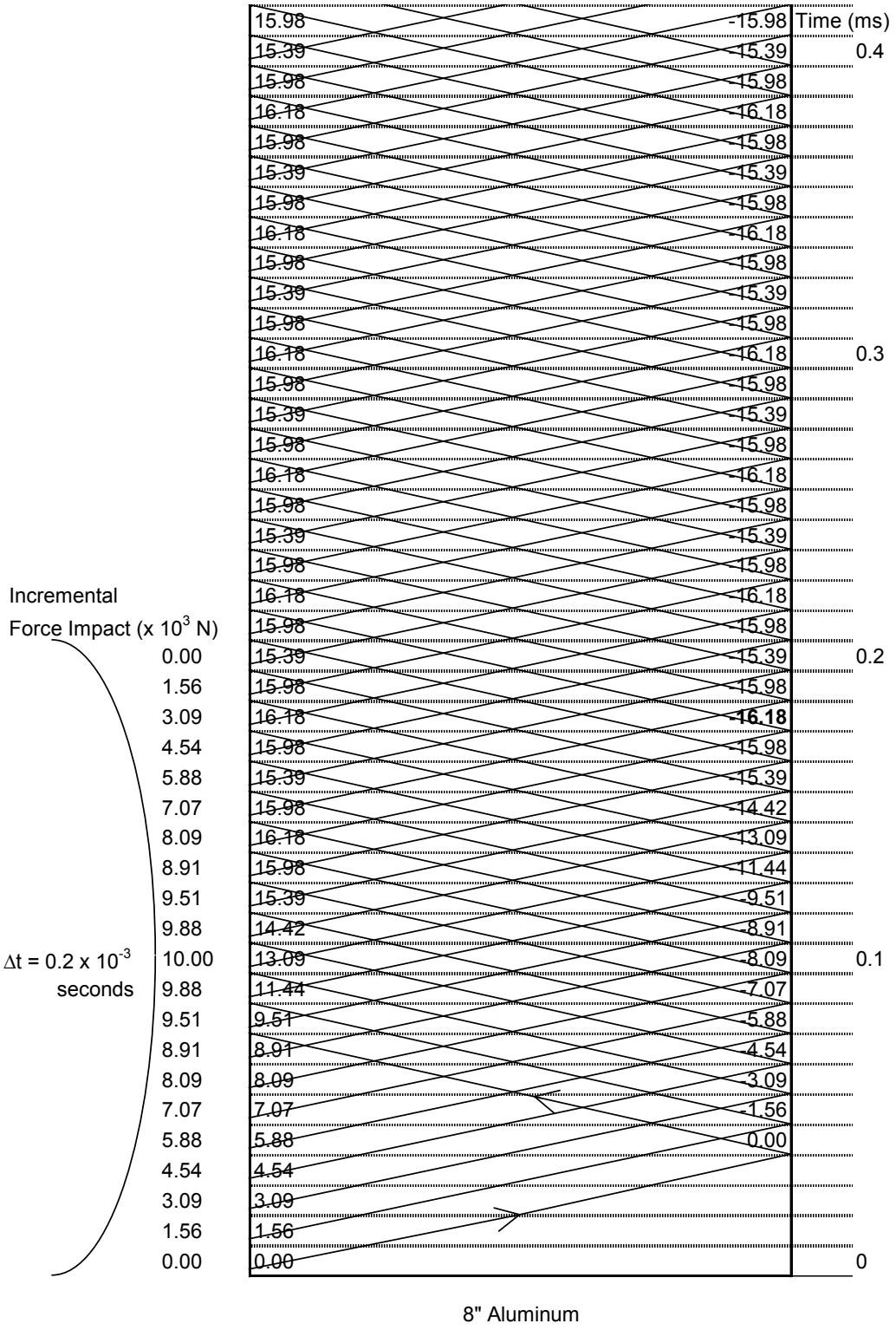

Figure 5.8 Wave tracing of "Al" under a half-sine impact with a maximum magnitude of 10 x 10^3 N and an impact duration of 0.2 x 10^{-3} seconds. Maximum propagated wave at the right end is 16.18 x 10^3 N. Column values represent the magnitude of the propagating wave in kN. Positive values indicate a compressive wave and negative tensile.

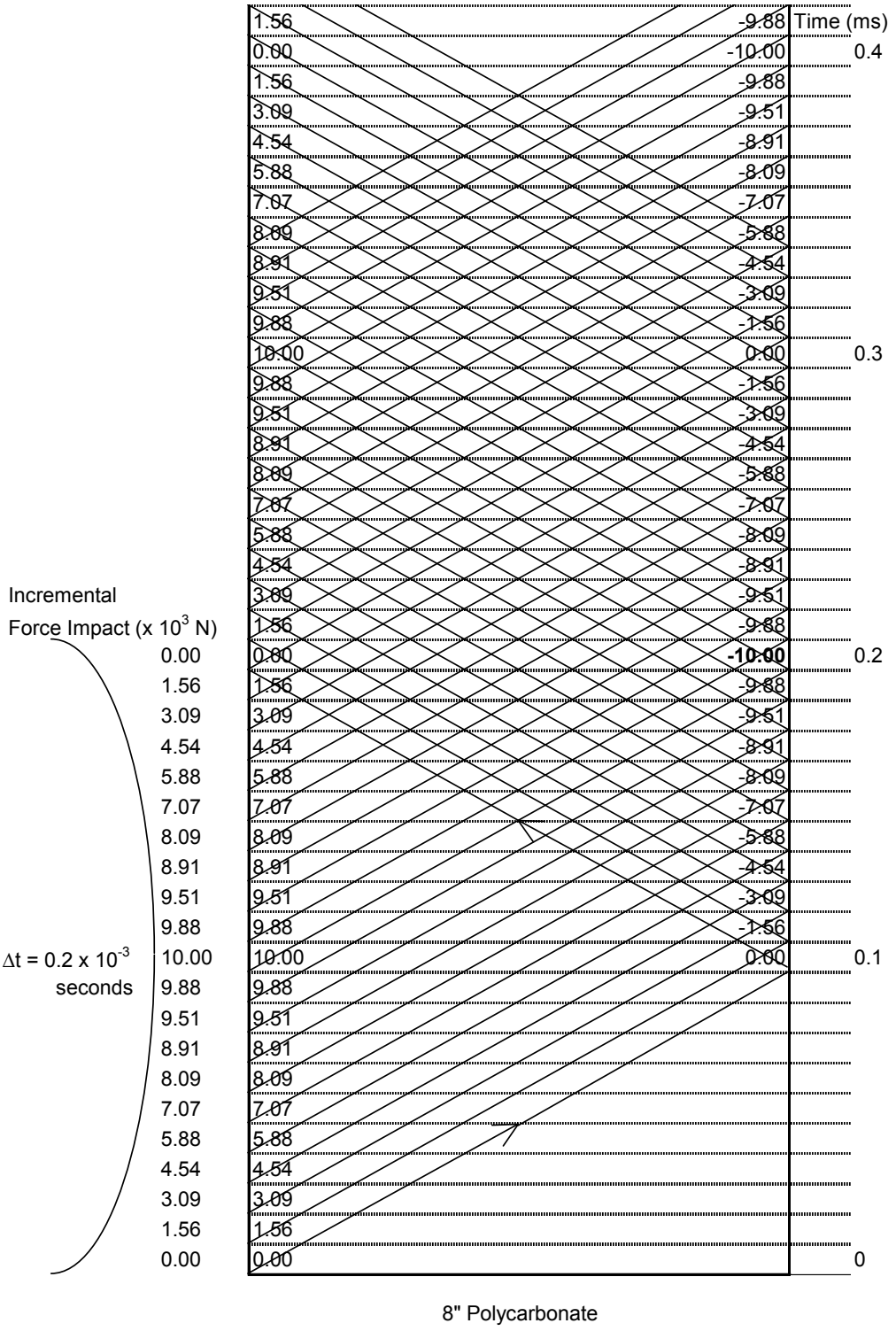

Figure 5.9 Wave tracing of "Poly" under a half-sine impact with a maximum magnitude of 10 x 10^3 N and an impact duration of 0.2 x 10^{-3} seconds. Maximum propagated wave at the right end is 10.00 x 10^3 N. Column values represent the magnitude of the propagating wave in kN. Positive values indicate a compressive wave and negative tensile.

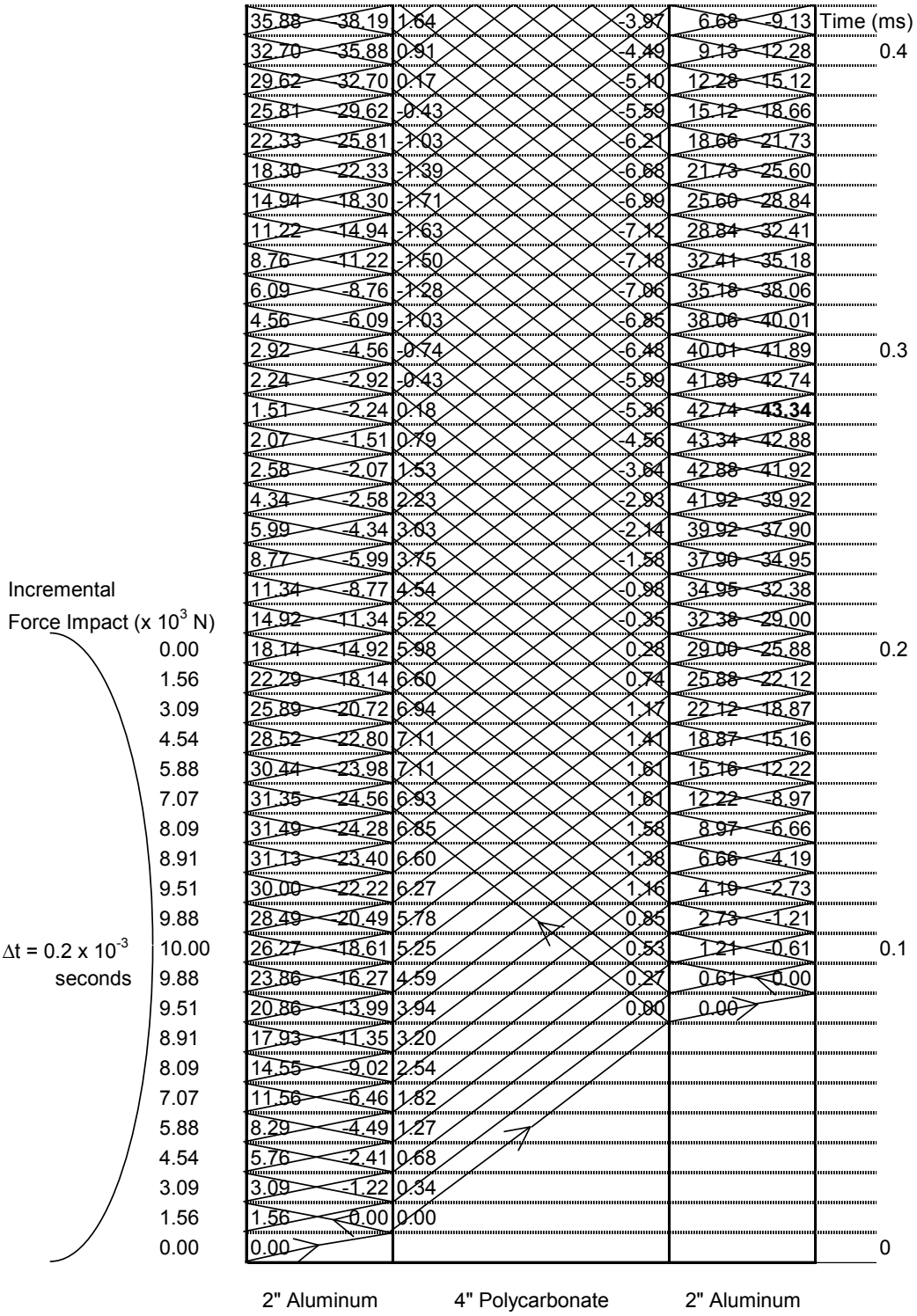

Figure 5.10 Wave tracing of "APA-2" under a half sine impact with a maximum magnitude of 10 x 10^3 N and an impact duration of 0.2 x 10^{-3} seconds. Maximum propagated wave at the right end is 43.34 x 10^3 N. Column values represent the magnitude of the propagating wave in kN. Positive values indicate a compressive wave and negative tensile.

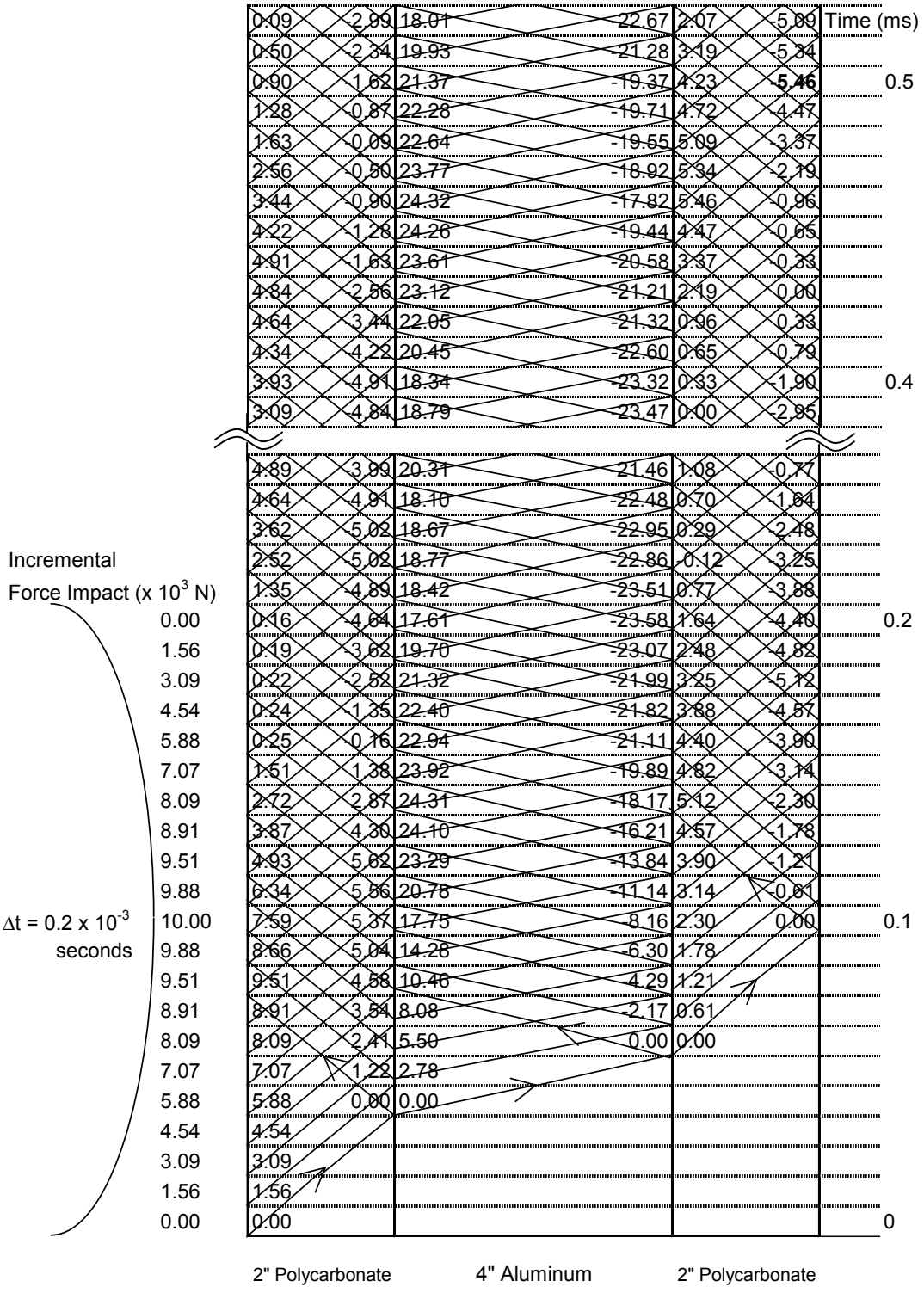

Figure 5.11 Wave tracing of "PAP" under a half sine impact with a maximum magnitude of 10 x 10^3 N and an impact duration of 0.2 x 10^{-3} seconds. Maximum propagated wave at the right end is 5.46 x 10^3 N. Column values represent the magnitude of the propagating wave in kN. Positive values indicate a compressive wave and negative tensile.

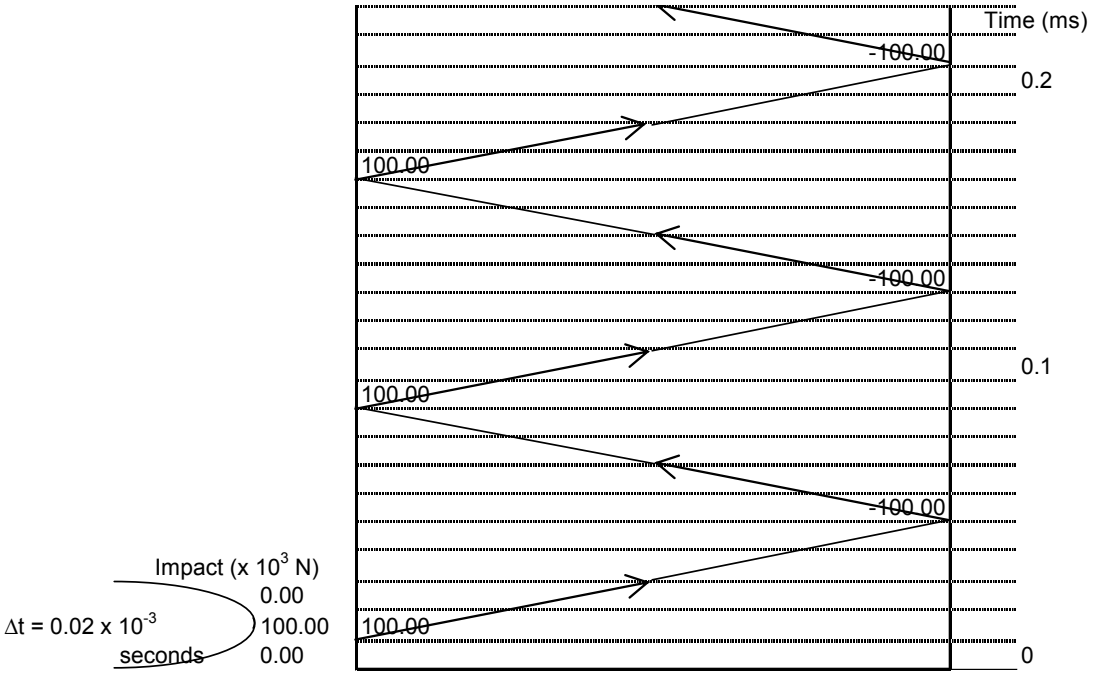

(a) 8" Aluminum

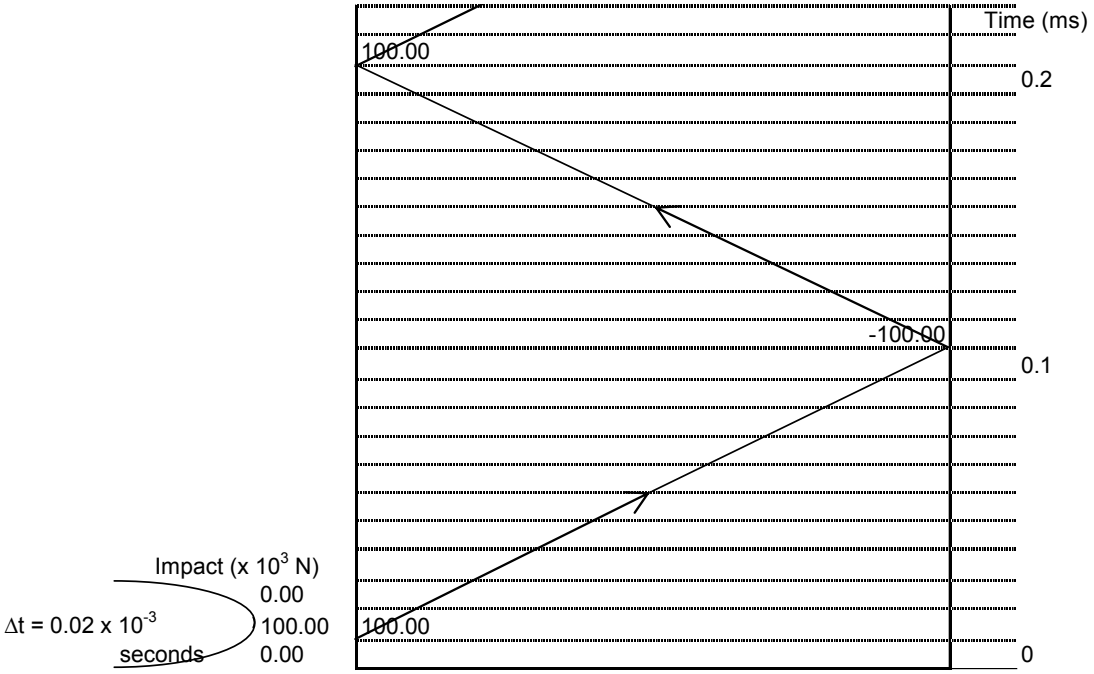

(b) 8" Polycarbonate

Figure 5.12 Wave tracing of (a) "Al" and (b) "Poly" under a half sine impact with a maximum magnitude of 100 x 10^3 N and an impact duration of 0.02 x 10^{-3} seconds. Maximum propagated wave at the right end is 100.00 x 10^3 N for both "Al" and "Poly". Column values represent the magnitude of the propagating wave in kN. Positive values indicate a compressive wave and negative tensile.

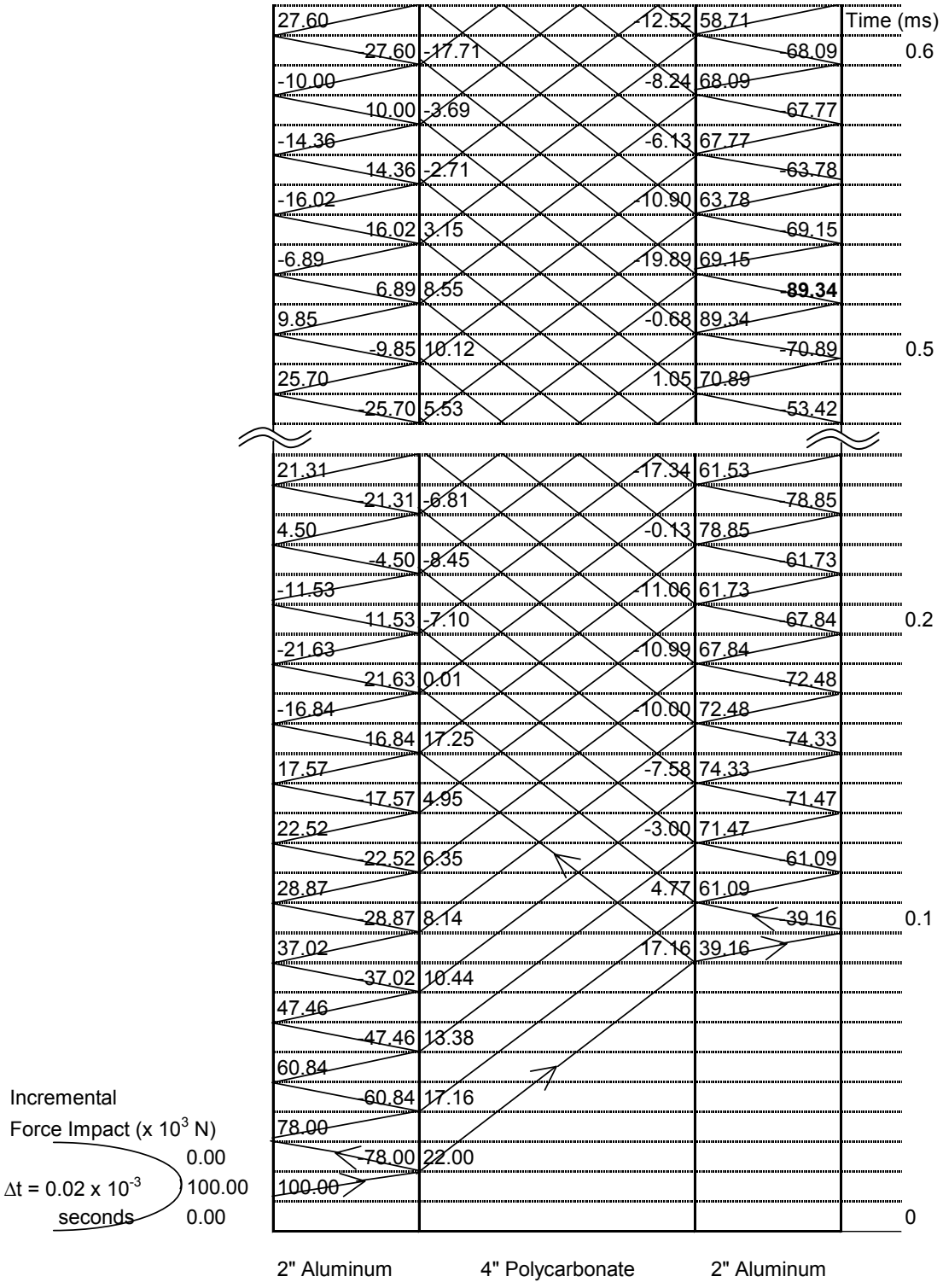

Figure 5.13 Wave tracing of "APA-2" under a half sine impact with a maximum magnitude of 100 x 10^3 N and an impact duration of 0.02 x 10^{-3} seconds. Maximum propagated wave at the right end is 89.34 x 10^3 N. Column values represent the magnitude of the propagating wave in kN. Positive values indicate a compressive wave and negative tensile.

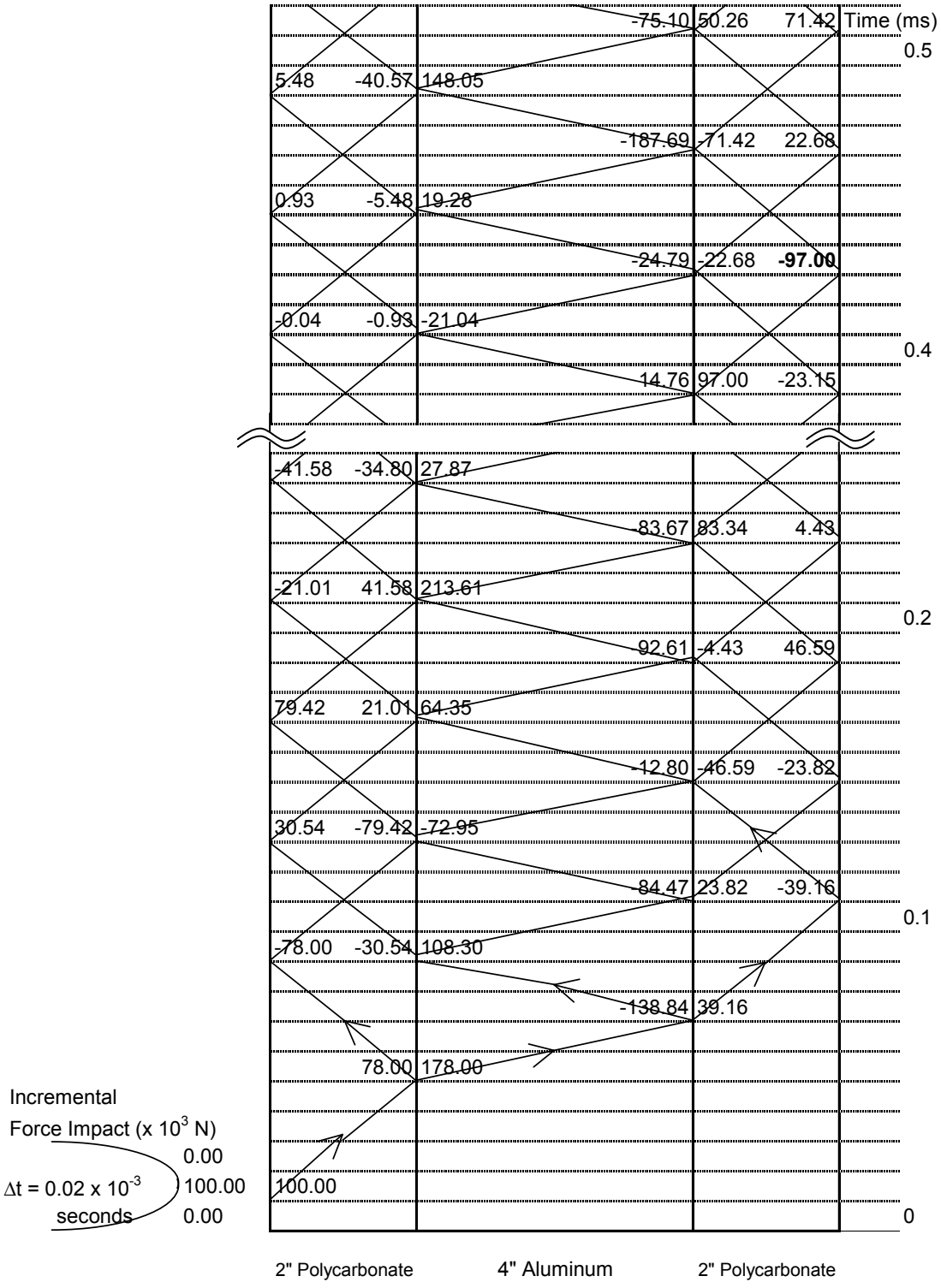

Figure 5.14 Wave tracing of "PAP" under a half sine impact with a maximum magnitude of 100 x 10^3 N and an impact duration of 0.02 x 10^{-3} seconds. Maximum propagated wave at the right end is 97.00 x 10^3 N. Column values represent the magnitude of the propagating wave in kN. Positive values indicate a compressive wave and negative tensile.

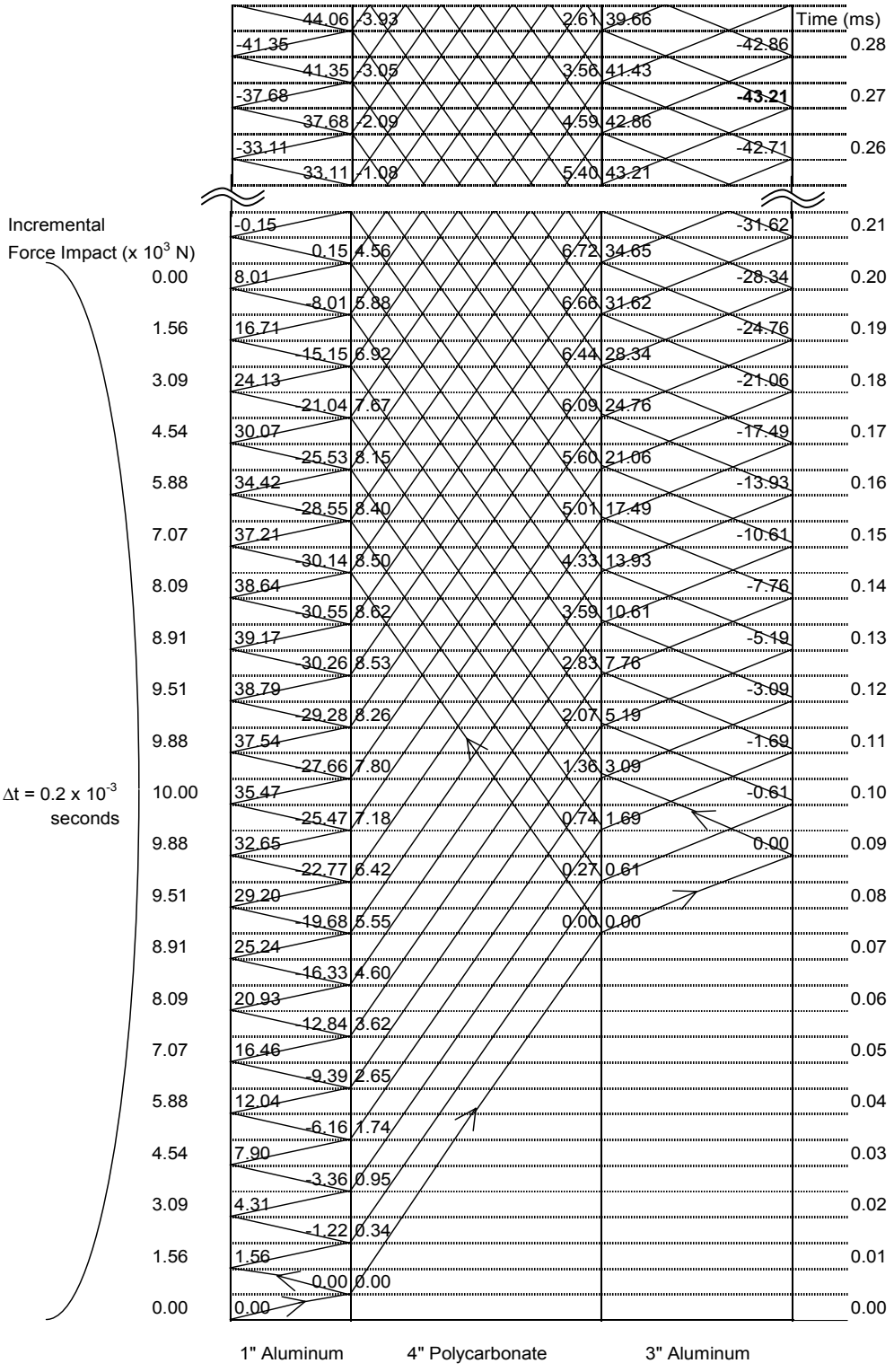

Figure 5.15 Wave tracing of "APA-1" under a half sine impact with a maximum magnitude of 10 x 10^3 N and an impact duration of 0.2 x 10^{-3} seconds. Maximum propagated wave at the right end is 43.21 x 10^3 N. Column values represent the magnitude of the propagating wave in kN. Positive values indicate a compressive wave and negative tensile.

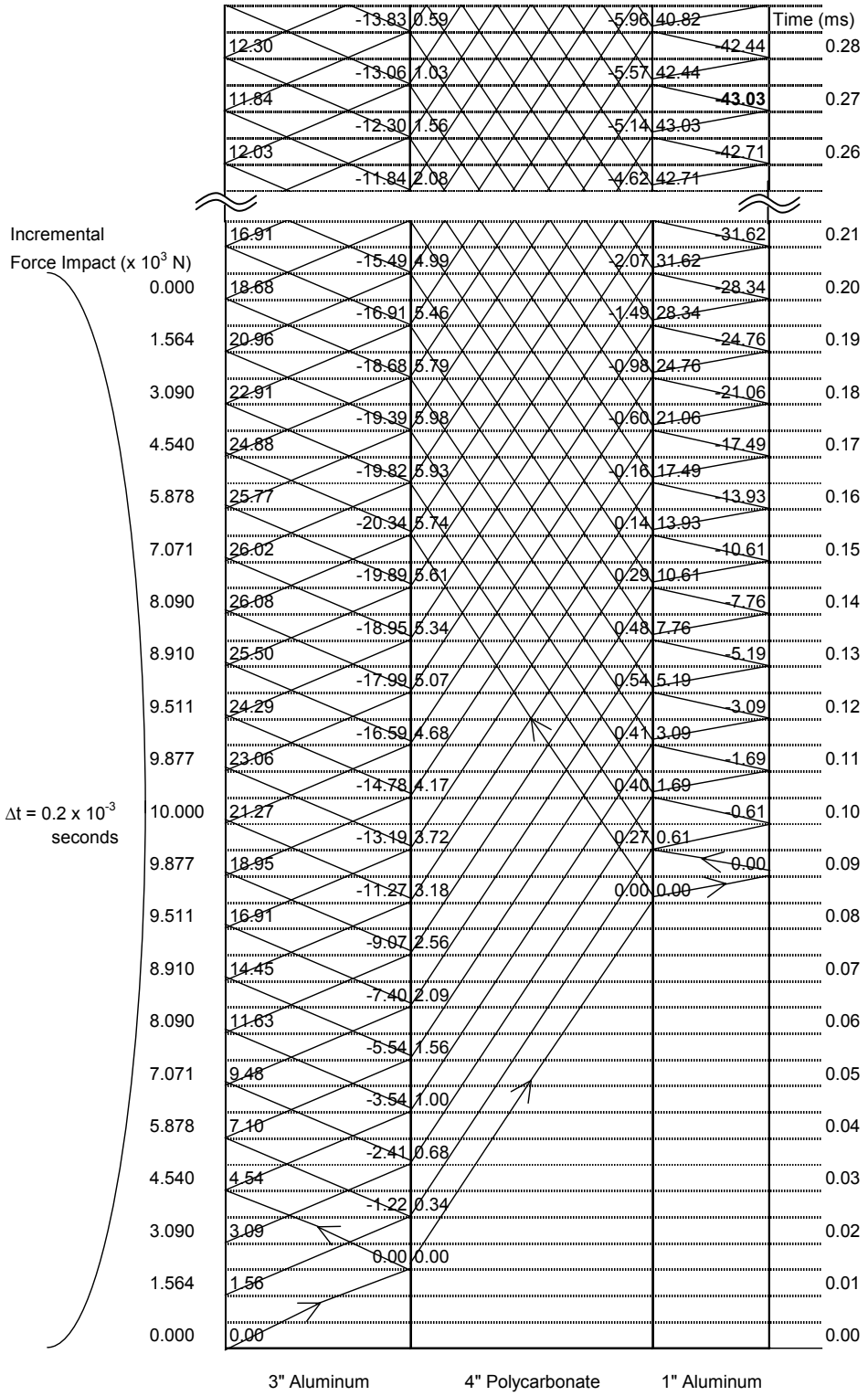

Figure 5.16 Wave tracing of "APA-3" under a half sine impact with a maximum magnitude of 10 x 10^3 N and an impact duration of 0.2 x 10-3 seconds. Maximum propagated wave at the right end is 43.03 x 10^3 N. Column values represent the magnitude of the propagating wave in kN. Positive values indicate a compressive wave and negative tensile.

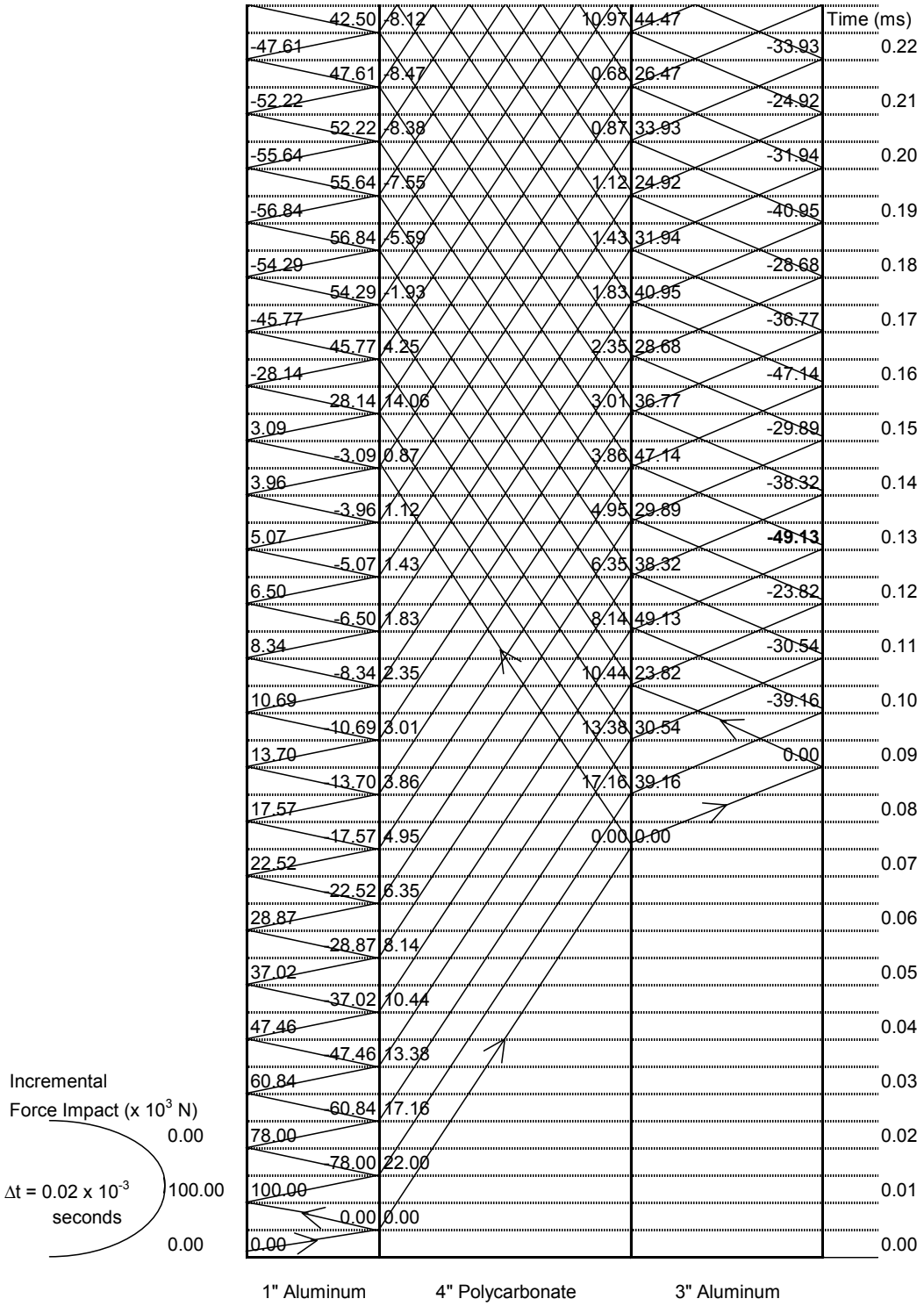

Figure 5.17 Wave tracing of "APA-1" under a half sine impact with a maximum magnitude of 100 x 10^3 N and an impact duration of 0.02 x 10^{-3} seconds. Maximum propagated wave at the right end is 49.13 x 10^3 N. Column values represent the magnitude of the propagating wave in kN. Positive values indicate a compressive wave and negative tensile.

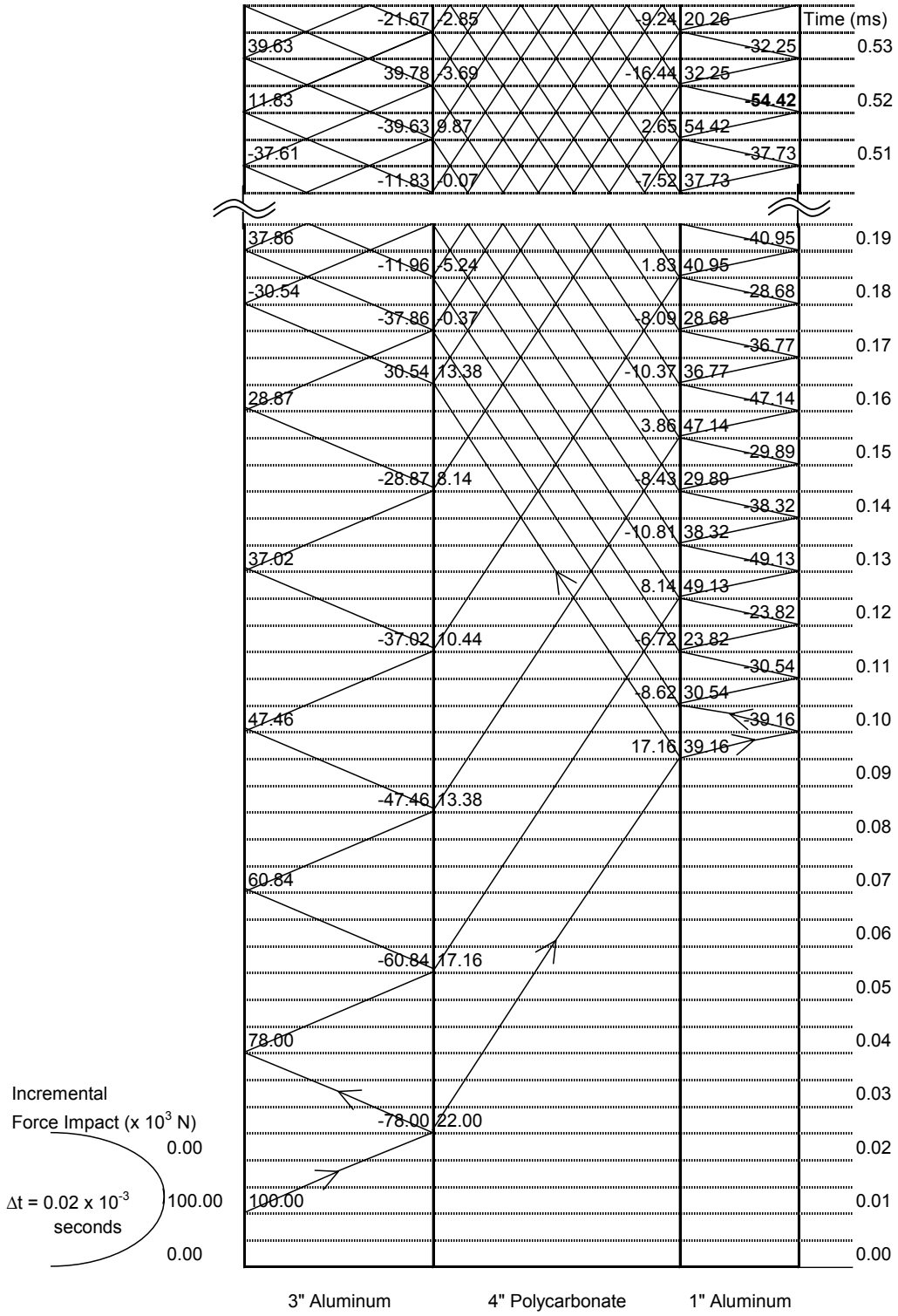

Figure 5.18 Wave tracing of "APA-3" under a half sine impact with a maximum magnitude of 100 x 10^3 N and an impact duration of 0.02 x 10^{-3} seconds. Maximum propagated wave at the right end is 54.42 x 10^3 N. Column values represent the magnitude of the propagating wave in kN. Positive values indicate a compressive wave and negative tensile.

5.2.2.2 Acceleration Response in Undamped Spring-Mass System

Accelerations in the cylindrical structures under a half-sine curve impulse can be calculated using the equation shown above (Equation 5.5). When a half-sine force of 10,000 N at the peak with 0.2 x 10^{-3} seconds impact duration (Force 1) was applied to "Al" and "Poly", Equation 5.5 can be written by substituting the material properties shown in Table 1 as,

Al; $\ddot{x} = 2322\sin(25058t) - 1455\sin(15708t)$ Equation 5.7

Poly; $\ddot{x} = -2702\sin(6813t) + 6231\sin(15708t)$ Equation 5.8

From the above equations, the maximum acceleration in "Poly" was obtained as approximately 4,600 m/s^2, which was nearly twice as high as that of "Al" (≈ 2,700 m/s^2). Similarly, when a half-sine force of 100,000 N at the peak with 0.02 x 10^{-3} seconds impact duration (Force 2) was applied, Equation 5.5 can be written for "Al" and "Poly" as

Al; $\ddot{x} = -3680\sin(25058t) + 23069\sin(157080t)$ Equation 5.9

Poly; $\ddot{x} = -2198\sin(6813t) + 50680\sin(157080t)$ Equation 5.10

From the above equation, the difference in the maximum acceleration was slightly higher than the result obtained using Force 1. The maximum acceleration in "Poly" was about 51,000 m/s^2, while in "Al" it was approximately 22,000 m/s^2. The differences in the acceleration response in the "Al" and "Poly" are due to the differences in their mass densities and Young's moduli.

The accelerations responses from the FEA and the equation of motion are significantly different. This might be caused by the way an impact is applied in a structure. The impact is applied at nine central nodes of the structure in the FEA study,

while the impact is considered to be applied at the full end face of the structure in the equation of motion.

5.3 Discussion

Computational results showed that "APA-2" has the lowest maximum magnitude of acceleration among four different configurations; "Al", "Poly", "PAP" and "APA-2" whether the impact duration is long (0.2×10^{-3} seconds) or short (0.02×10^{-3} seconds). However, this was not the case when waves were traced using reflected and transmitted coefficients (Equations 1.1 and 1.2). When the wave was traced, the order of maximum magnitude of wave reached at the end of the cylindrical structures changed depending on the impact duration. When the impact with long impact duration (0.2×10^{-3} seconds) was used, the highest maximum waves were observed in "APA-2", followed by "Al", "Poly" and "PAP". On the other hand, when the impact was applied with shorter impact duration (0.02×10^{-3} seconds), the highest wave was in "Al" and "Poly" followed by "PAP", and the lowest maximum wave was in "APA-2". This difference may be caused by excluding effect between applied impact and acceleration response based on material. When the equation of motion was used to calculate the acceleration response, the acceleration showed significant differences between aluminum and polycarbonate. Polycarbonate has much higher magnitude of acceleration response than that of aluminum under the same impact condition. For instance, the wave tracing showed 16.18×10^{3} N maximum magnitude in "Al" and 10.00×10^{3} N in "Poly", concluding that "Al" has higher maximum magnitude of wave. However, acceleration from the motion of equation showed approximately twice as much acceleration in "Poly" than "Al". Therefore, the

combined force results obtained from wave tracing and accelerations from the equation of motion for "Poly" ended up having higher maximum acceleration. It is clear that when different materials were used at the impact face, wave tracing might not be useful to study magnitude of wave propagation phenomena.

However, the wave tracing clearly showed the differences within the same material combinations. When the material order of aluminum, polycarbonate and aluminum was used with short impact duration force, the wave tracing showed that the number of interference incidences between reflected and transmitted wave is higher in "APA-2" resulting in increased maximum magnitude of wave. On the other hand, when there is interference between the applied impact and the reflected wave, the interference increases the maximum wave amplitude significantly and the reductions at the material interfaces become almost negligible.

Wave tracing also showed when "PAP" is used, a reflected wave from the first interface reduces magnitude of propagating wave by interfering with the applied impact. However, acceleration magnitude significantly changes depending on materials used in a structure based on their densities and Young's modulus. As shown in the results obtained from the FEA and the equation of motion, "Poly" had much higher magnitude of acceleration then that of "Al" under the same applied impact force. Therefore, when the acceleration response of "PAP" is compared with that of "Al", since "Al" has higher density and Young's modulus, "PAP" showed much higher magnitude of acceleration response. On the other hand, when "PAP" is compared with that of "Poly", "PAP" showed lower magnitude of accelerations even though "Poly" has lower density and Young's modulus. Therefore, in this case, the impedance mismatch seemed to affect the

magnitude of accelerations more compared to the differences in their densities and Young's modulus. Unlike "Al" and "APA" cases where differences in the acceleration responses change depending on the interference between an applied impact and reflected wave, "PAP" always showed lower magnitude of accelerations compared to "Poly". This is because the interference between an applied impact and reflected wave helps to reduce the magnitude of propagating wave in "PAP".

Bibliography

Thomson, W. T. (1993). *Theory of vibration with applications* (4th ed.). New Jersey: A Simon & Schuster Company.

Livermore Software Technology Corporation (2003). LS-DYNA Keyword user's manual, Version 970, April.

CHAPTER 6

THE POTENTIAL APPLICATIONS OF METAL FOAMS IN AIR-GUN FIRED PROJECTILES

Metal foams are a new class of materials with low densities and novel physical, mechanical, thermal, electrical and acoustic properties. Because of their novel properties, especially considerable energy absorbing capacity, metal foams have been considered their applications in absorbing impacts and shocks (Radford et al., 2005). In this chapter, potential usages of metal foams are considered.

6.1 Introduction

Foam, a type of cellular solids, is an assembly of cells with solid edges or faces packed together. Examples of cellular solids are wood, cork, sponge, and coral which are found in nature or man-made foams. Man-made foams can be made of polymers, metals, ceramics and glass. Foams made of metals are called metal foams or metallic foams. Metal foams are a new class of materials with low densities and novel physical, mechanical, thermal, electrical and acoustic properties. The range of properties available to engineers through foaming is as follow; density ranges from 1 to 10^3 kg/m^3 and young's modulus is from 10^{-3} to 10^3 MPa. However, it should be noted that their characterization is still imperfect and their efficient use requires a detailed understanding of their mechanical behavior (Gibson and Ashby, 1997).

6.2 Foaming Process

There are nine processes to metal foams currently, of which five are established commercially. Depending on the manufacturing methods, cell type (closed- or open-cell), cell size and relative density of the foam change (Ashby et al. 2000). Closed-cell is that each cell is sealed off from its neighbors by membrane-like faces. If each cell is open and connected to its neighbors by edges, cell type is open-cell. Commercially five established processes are briefly described below. Detailed processes can be found in Ashby et al. (2000).

Aluminum foam may be produced by bubbling gas through molten Al-SiC or Al-Al_2O_3 alloys. A variety of gases can be used to create bubbles. Air is most commonly used but carbon dioxide, oxygen, inert gases and even water can also be used. Low relative density, closed-cell foams can be produced by carefully controlling the gas-injection process and the cooling rate of the foam. This process is the least costly one to implement and results in foam with cell diameters between 5 and 20 mm and relative densities in the range 0.03 to 0.1.

Aluminum foam can also be formed by stirring a foaming agent (typically titanium hydride, TiH_2) into a molten alloy (typically an aluminum alloy) and controlling the pressure while cooling. The foaming agent releases gas that can lead to a closed-cell foam when the molten alloy has a high melt-viscosity. In order to control the melt-viscosity, calcium is added to melting aluminum. The cell size can be varied from 0.5 to 5 mm by changing the TiH_2 content along with heating and cooling conditions. Foams with relative densities from 0.2 to as low as 0.07 can be manufactured using this process.

Since the process needs expensive calcium and titanium hydride, it is likely to be costlier than gas-injection methods (Ashby et al., 2000).

During the foaming process, instead of adding the foaming agent into molten alloy, the foaming agent can be added into the base metal powder. After consolidating the metal powder with the foaming agent, it is heated into a mushy state during which the foaming agent releases hydrogen and the materials then expand to become foam. Foams thus produced have close-cells with diameters ranging from 1 to 5 mm and relative densities as low as 0.08. Since the metal is foamed in a sealed split mold, the process results in components of the exact shape of the mold.

Another process used to make foam is by using open-cell wax or polymer-foam precursor as a template. First, a ceramic mold is manufactured from the wax or polymer-foam precursor, then, the precursor is burned and the molten metal is infiltrated by applying pressure into the mold. Metal powder slurries can also be used instead of molten metals. The process makes open-cell foams with pore sizes of 1-5 mm and relative densities as low as 0.05. The process can be used to manufacture foams from almost any metal that can be investment casting. Investment casting is one of metal-forming techniques that can make exact intricate shape with minimum machining or surface treatments.

Another way of using open-cell polymer foams is to use them as templates. Metals are deposited onto the polymer foams by chemical vapor decomposition, evaporation or electro-deposition. The chemical vapor decomposition uses a thermally decomposable chemical which containing the base material for foam. The chemical is vaporized and deposited while passing through the templates. After several tens of micrometers of the

metal have been deposited, the polymer is burnt out by heating in air, leaving cell edges with hollow cores. Foams with open pore sizes in the 100-300 μm diameter range and the low relative density of 0.02-0.05 are produced by this process. However, the method is restricted to pure elements such as nickel or titanium because of the difficulty of chemical vapor decomposition or electro-deposition of alloys.

6.3 Properties

The properties of metal foam depend upon the properties of the metal, relative density and cell topology such as open or closed cell, and cell size. Like those of other cellular solids, foams show linear elasticity at low stresses followed by a long collapse plateau region and then a regime of densification in which the stress rises steeply to simulate the stress-strain curve of the solid from which the foam is made. The stress-strain curve of the foam is similar to that of honeycomb since both of them can be considered as a type of cellular solids. Honeycomb is a near-perfect order of a cellular solid while foam is a disordered cellular solid. The elastic collapse stress and the post-collapse behavior depend on whether the foam has open or closed cells (Gibson and Ashby, 1997). According to Ashby et al. (2000) the initial loading curve is not straight and its slope is less than the true modulus, because of premature yielding and/or wall collapse in some cells.

Similarly, Young's modulus and sound velocities vary at three distinct stages of the stress-strain relationships (Lopatnikov et al. 2004). Sound velocities of aluminum foam during the first part of the stress-strain diagram are on the order of 600 – 800 m/s, during the "plateau" and up to the complete densification of the foam, the effective sound

velocity is on the order of 50 – 400 m/s, and after the foam attains the density of the constituent material there is a sudden jump. For aluminum, the longitudinal sound velocity at this stage is approximately 5000 m/s. As mentioned in Chapter 1, longitudinal sound velocity is calculated using Equation 1.1 based on Young's modulus and density of the material. Young's modulus is obtained from the slope of the stress-strain curve. Three distinct stress-strain relationships as mentioned earlier give three distinct Young's moduli. When the stress in foam reaches the yielding stress, the foam starts collapsing and densifying. Since both the Young's modulus and the density of foam change, sound velocity also changes as Lopatnikov et al. (2004) reported.

Foam has a long plateau of the stress-strain curve, arising from cell collapse by buckling, yielding or crushing which allows large energy/absorption at near constant load. Deshpande and Fleck (2000) reported that the high strain rate (up to 5000 s^{-1}) compressive behavior of aluminum-based foams (Alulight closed-cell foam and Duocel open-cell, Appendix) is very similar to their quasi-static behavior. Note that the experiments were conducted under sufficiently small impact velocity (less than 50 m/s) for shock wave effect to be negligible. Ruan et al. (2002) concluded that the plateau stress of aluminum foam (Cymat, Appendix) is insensitive to the strain rate of 0.001 – 10 s^{-1} by conducting the compressive test using an MTS machine. However, contradicting results are also reported by others. Paul and Ramamurty (2000) investigated the strain rate sensitivity of closed-cell aluminum foam under strain rates ranging from 3.33×10^{-5} to 1.6×10^{-1} s^{-1}. Within this range of the strain rates, experimental results of closed-cell aluminum alloy foam (Alporas, Appendix) showed increases in its plastic strength and energy absorption by 31 and 52.5%, respectively. Dannemann and Lankford (2000)

studied the compressive deformation behavior of open- and closed-cell aluminum foams using a split Hopkinson pressure bar system at strain of 400 – 2500 s^{-1}. They found that a strain rate strengthening occurs in closed-cell aluminum (Alporas) foams, especially with higher density (15%). Mukai et al. (2006) also conducted compression tests of closed-cell aluminum foam (Alporas) at high strain rate up to 1300 s^{-1} and reached the same conclusion with Dannemann and Lankford (2000).

Tan et al. (2005) studied the response of Hydro/Cymat (Appendix) foams with two different cell sizes (14 and 4 mm) to dynamic loads and reported that deformation pattern of aluminum foams are related to impact velocity. At a sub-critical velocity the deformation pattern is similar to quasi-static loading, the plastic collapse initiates at the weakest band of cells, almost always in the interior of the specimen. At a super-critical velocity, the impulse generated by impact is so severe that the cells at the impact surface undergo rapid plastic collapse and densify sequentially. Radford et al. (2005) clearly showed this phenomenon using a high-speed photographic sequence.

One of the other interesting properties of foams is sound management. Foamed acoustic tiles are a familiar remedy for a noisy room since open-cell foams absorb sound very well. However, foams do not prevent sound transmission from a neighboring space (Gibson and Ashby, 1997).

6.4 Potential Usage of Metal Foam in Acceleration Mitigation

As mentioned earlier, when the metal foam has not attained the density of the constituent material, the effective sound velocity is at least one order of magnitude lower than that of the constituent material. Our investigations of air-gun fired projectiles,

discussed earlier in this dissertation, revealed that the maximum axial stress at a face of a polycarbonate ring of a projectile is less than 40 MPa, when the impact speed on the honeycomb mitigator is 80 m/s (Figure 6.1).

Lopatnikov et al. (2004) investigated the changes in sound velocity using metal foams whose plateau stresses range from 2 to 8 MPa depending on the densities. Deshpande and Fleck (2000) reported compressive behavior of aluminum foams, Alulight, whose plateau stresses range from 10 to 12 MPa. These aluminum foams have much lower yield stresses than stresses the projectile might experience. However, Alulight (2006) reported aluminum foam with a plateau stress above 22 MPa. Rabiei and O'Neill (2005) developed a composite metal foam made of hollow steel spheres bundled with aluminum

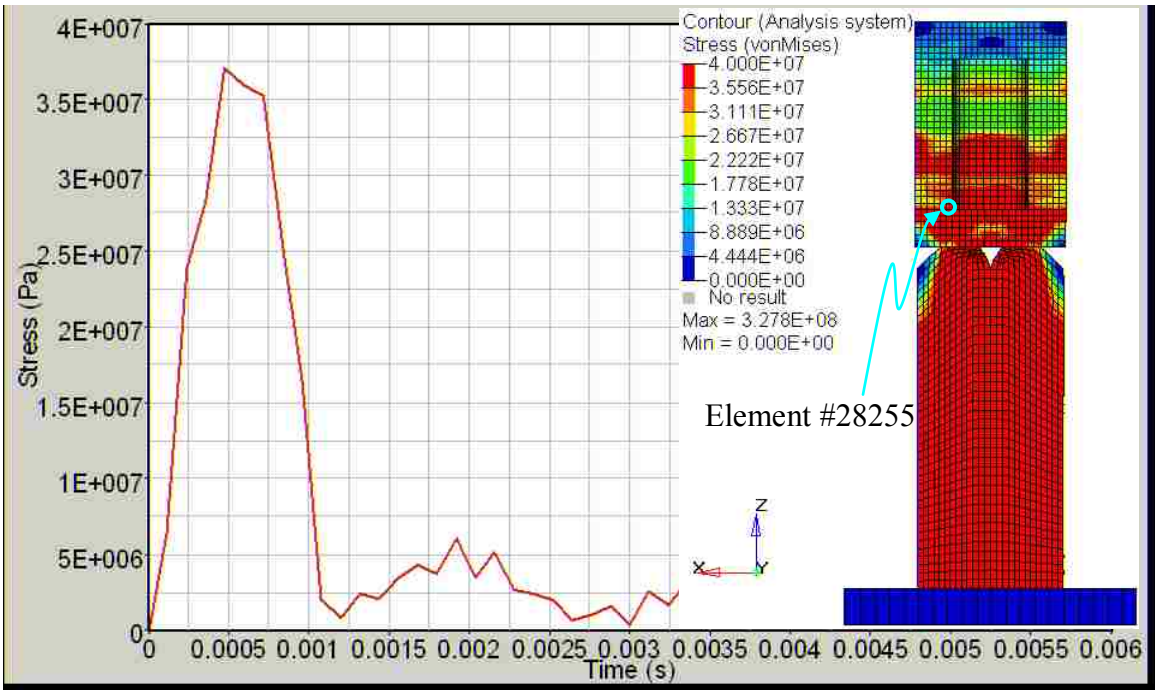

Figure 6.1 Stress curve of the element 28255 of aluminum and polycarbonate projectile fired with 80 m/s impact speed. Left figure shows vonMises stress contour when the element 28255 is at the maximum stress.

356 alloy using a casting process. The new composite metal foam has the average plateau stress of approximately 60 MPa and a densification strain of approximately 0.6. Therefore it is possible that the impact waves pass through a metal foam ring in a projectile before reaching its complete densification state. This implies that metal foams may be used as a lower impedance material in order to mitigate accelerations using the impedance mismatch concept. Since metal foams can also help to damp energy, metal foams might be a good candidate to for use of ring sections in air-gun projectiles to reduce the affect of impact loading and high frequency accelerations.

6.5 Finite Element Analysis of a Projectile using Metal Foam

Utilizing the finite element model described in Chapter 2, finite element analysis of a projectile made of aluminum and metal foam was conducted. Metal foam was used as a substitute of the polycarbonate rings as shown in Figure 6.2.

6.5.1 Modeling of Metal Foam

Metal foam could be defined in the same manner as honeycomb material in LS-DYNA since both of them are considered as a type of cellular solids and their stress-strain curves are similar to each other. As mentioned earlier, the honeycomb mitigator of air-gun test simulations were defined using *MAT_MODIFIED_CRUSHABLE_FOAM since the material card can handle strain-rate effects. However, recent research in metal foams shows contradicting results in strain rate effects as mentioned in the previous section. Some researchers say properties of metal foams are insensitive to the strain rate and some say plastic strength and energy absorption of metal foams increase as strain rate

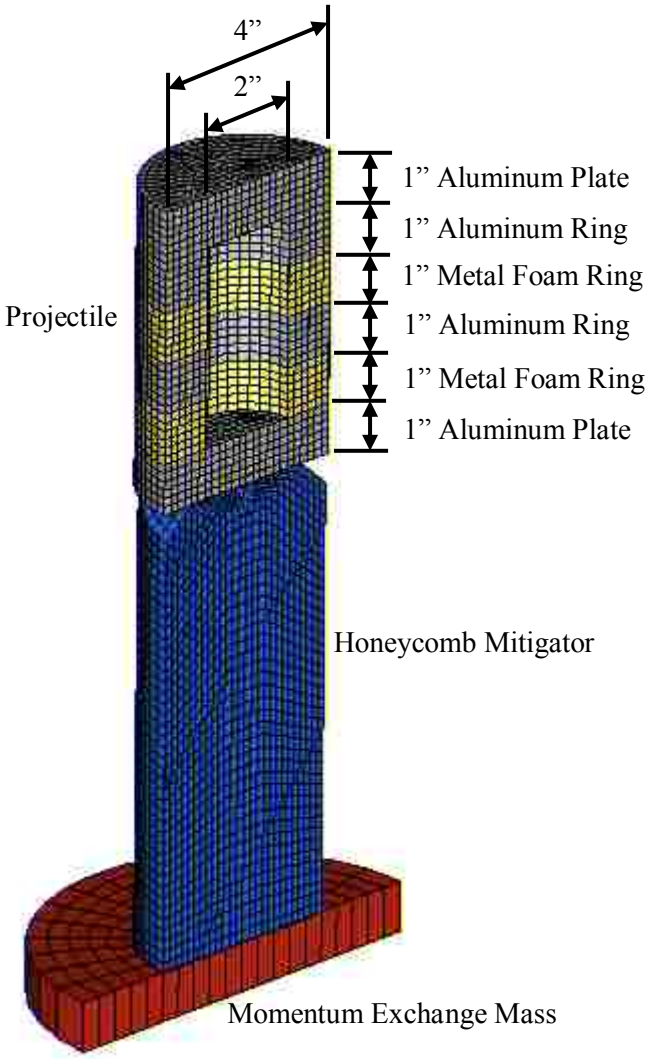

Figure 6.2 Cross sectional view of the air-gun model.

increases. Therefore, in this simulation, *MAT_CRUSHABLE_FOAM was used to define the metal foam considering that the strain rate effects are not significant.

Two types of metal foam, aluminum foam and composite metal foam (steel and aluminum) were used in the finite element analyses. Material properties and stress-strain curves of the aluminum and the composite metal foam were compiled based on Alulight (2006) and Rabiei and O’Neill (2005), respectively. Stress-strain curves used in the FE

model are shown in figures 6.3 and material properties of the metal foams are summarized in table 6.1 along with other materials for comparison purpose.

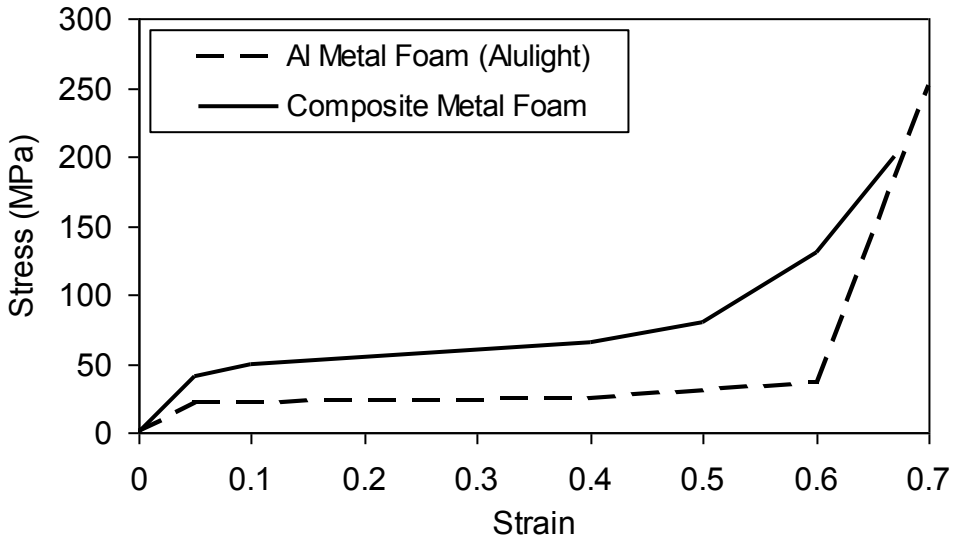

Figure 6.3 The stress-strain curves used for LS-DYNA models.

Table 6.1 Material Properties

	Density ρ (kg/m^3)	Young's Modulus E (GPa)	Wave Speed c (m/s)	Impedance Z (kg/m^{2}s)
Aluminum	2700	70	5092	1.37E+07
Polycarbonate	1200	2.3	1384	1.66E+06
Al Honeycomb	608.7	11.38	4324	2.63E+06
Al Metal Foam (Alulight)	700	0.44	793	5.55E+05
Composite Metal Foam	2400	1.2	707	1.70E+06

Table 6.2 Weight of the projectiles

	Ring Weight (kg)	Total Weight (kg)	Differences[a] (kg)
All Al	0.83	2.78	0.00
Al & Poly	0.37	2.31	0.46
Al & Al MF	0.22	2.16	0.62
Al & Comp. MF	0.74	2.69	0.09
Al & Al HC	0.19	2.13	0.65

[a]Weight differences between All Al projectile and other projectile

6.5.2 Results and Discussion

The results from five different projectile configurations are compared. Five different projectiles are: a projectile made of aluminum (All Al), a projectile made of aluminum and polycarbonate (Al & Poly), a projectile made of aluminum and aluminum metal foam (Al and Al MF), a projectile made of aluminum and composite metal foam (Al and Comp. MF), and a projectile made of aluminum and aluminum honeycomb (Al and Al HC). Each projectile has different weight since each material has different material density as shown in table 6.2. This fact causes the differences in impact forces that are experienced by each projectile. However as shown in figure 6.4, force differences were not significant except for the projectile made of aluminum and aluminum metal foam. When aluminum metal foam was used in the projectile, the foam crushed completely as shown in figure 6.5 and this causes a significant difference in the force curve.

Time history responses of all the projectiles are shown in figure 6.6. Each acceleration result is compared with the projectile made of aluminum. Figure 6.6a is the result from the projectile made of aluminum and polycarbonate which was the same

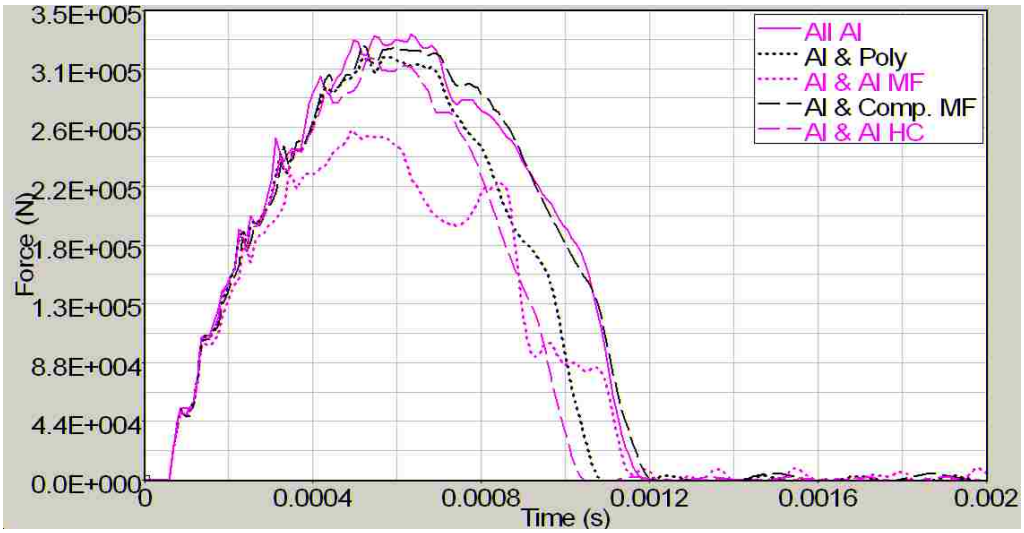

Figure 6.4 Impact force experienced by projectiles under 80 m/s impact speed.

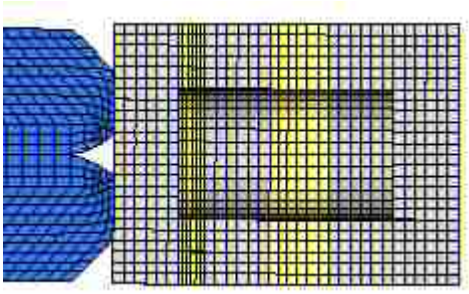

Figure 6.5 Condition of the aluminum and aluminum metal foam projectile at 0.001 seconds.

result discussed in Chapter 2. The result is shown here for easy comparison. Figure 6.6b is the acceleration curve from the projectile made of aluminum and aluminum metal foam. Acceleration shows the maximum peak after 0.001 seconds. This is caused by the complete crushed aluminum metal foam.

Figure 6.5 shows that one layer of aluminum metal foam closed to the impact face is almost completely crushed at 0.001 seconds. Once metal foam crushed completely, metal foam is densified and becomes similar to its constituted material, thus losing their

impedance mismatch mitigation potentials in a layered structure. Therefore the result shows once metal foam is densified, it has less effect of reducing the accelerations. Figure 6.6c is the result from the projectile made of aluminum and the composite metal foam. As shown in figure 6.3, the composite metal foam has much higher crush strength compared to the aluminum metal foam. The result shows that the composite metal foam did not crush by impacting with 80 m/s speed and there were much fewer oscillations in acceleration curve compared to the other projectiles. The maximum acceleration is also the smallest among all five simulated cases. Figure 6.6d shows the acceleration curve from the projectile made of aluminum and aluminum honeycomb. The acceleration curve shows high speed oscillation. Even though aluminum honeycomb has the lowest density among five materials used to build the projectile, impedance is the highest because of its high Young's modulus value as shown in table 6.1.

Figure 6.7 shows FFT responses of all the projectiles. The order of the appearance of the first peak of FFT is as follow; the aluminum and composite metal foam, the aluminum and polycarbonate, the aluminum and aluminum metal foam, the aluminum and aluminum honeycomb, and the aluminum projectiles. This is same order as the material impedance except metal foam. Aluminum metal foam has lower impedance than polycarbonate. However, the projectile made of aluminum and polycarbonate showed lower FFT peak than the one made of aluminum and aluminum metal foam. This can be explained by the crush of the aluminum metal foam, which caused in the increase in its density.

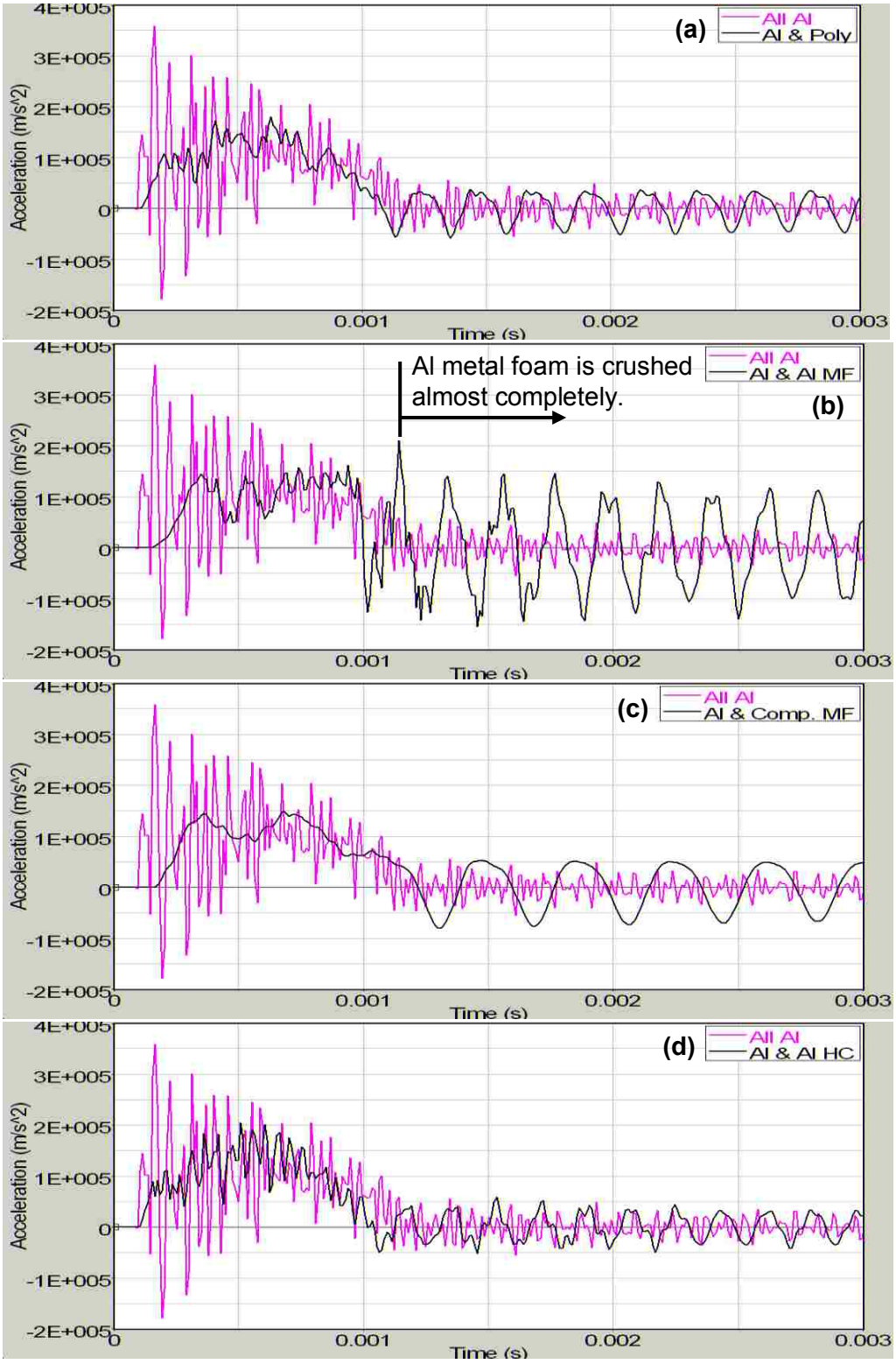

Figure 6.6 Acceleration responses of projectiles made of aluminum (All Al), aluminum and polycarbonate (Al & Poly), aluminum and aluminum metal foam (Al & Al MF), aluminum and composite metal foam (Al & Comp. MF) and aluminum and aluminum honeycomb (Al & Al HC).

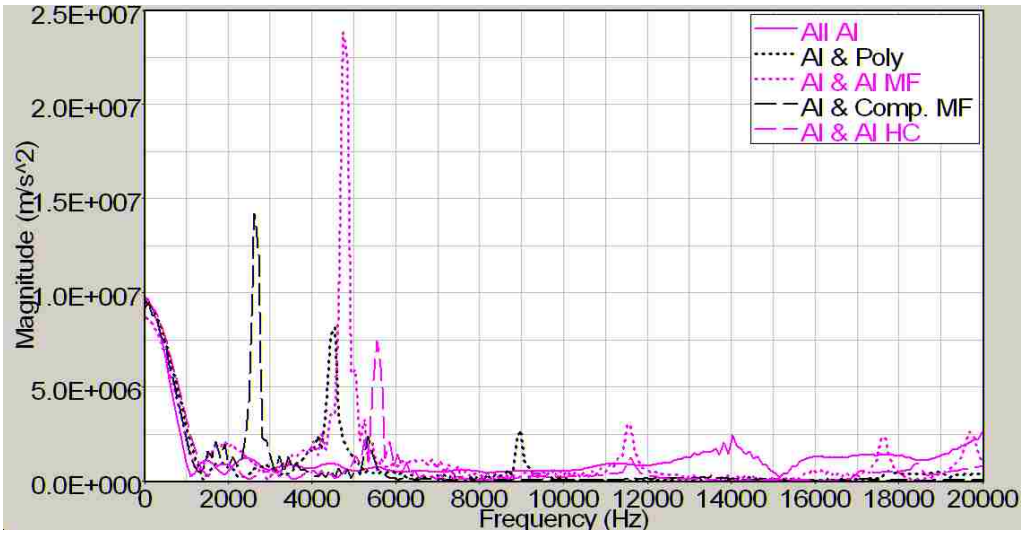

Figure 6.7 FFT response of the projectiles.

6.6 Conclusions

In the air-gun test with 80 m/s impact velocity, the simulation results showed that the most beneficial case of mitigating high frequency acceleration was the projectile made of aluminum and the composite metal foam. As we could see from the acceleration curves and FFT results, metal foam could be used to mitigate the high frequency accelerations if metal foam has much lower impedance than the base metal of the projectile and does not crush.

Bibliography

Alulight International GmbH (2006). Alulight Datasheets. Retrieved November, 20, 2007, from http://www.alulight.com/en/aluminium-foam

Ashby, M. F., Evans, A., Fleck, N. A., Gibson, L. J., Hutchinson, J. W. and Wadley, H. N. G.. (2000). *Metal foams: a design guide*. Oxford: Butterworth-Heinemann.

Dannemann, K. A. and Lankford Jr., James. (2000). High strain rate compression of closed-cell aluminum foams. *Materials Science and Engineering A*, 293, 157-164.

Deshpande, V. S. and Fleck, N. A. (2000). High strain rate compressive behaviour of aluminium alloy foams. *International Journal of Impact Engineering*, 24, 277-298.

Gibson, L. J. and Ashby, M. F. (1997). *Cellular solids: structure and properties* (2nd ed.). Cambridge: Cambridge University Press.

Lopatnikov, S. L., Gama, B. A., Haque, M. J., Krauthauser, C. and Gillespie Jr., J. W. (2004). High-velocity plate impact of metal foams. *International Journal of Impact Engineering*, 30, 421-445.

Mukai, T., Miyoshi, T., Nakano, S., Somekawa, H. and Higashi, K. (2006). Compressive response of a closed-cell aluminum foam at high strain rate. *Scripta Materialia*, 54, 533-537.

Paul, A. and Ramamurty, U. (2000). Strain rate sensitivity of a closed-cell aluminum foam. *Materials Science and Engineering*, A281, 1-7.

Rabiei, A. and O'Neill, A. T. (2005). A study on processing of a composite metal foam via casting. *Materials Science and Engineering A*, 404, 159-164.

Radford, D. D., Deshpande, V. S. and Fleck, N. A. (2005). The use of metal foam projectiles to simulate shock loading on a structure. *International Journal of Impact Engineering*, 31, 1152-1171.

Ruan, D., Lu, G., Chen, F. L. and Siores, E. (2002). Compressive behaviour of aluminium foams at low and medium strain rates. *Composite Structures*, 57, 331-336.

Tan, P. J., Reid, S. R., Harrigan, J. J., Li, S. and Zon, Z. (2005). Dynamic compressive strength properties of aluminum foams. Part I – experimental data and observations. *Journal of the Mechanics and Physics of Solids*, 53, 2174-2205.

CHAPTER 7

Civil Engineering Applications

Accelerations could be reduced using material impedance mismatch as we discussed in the preceding chapters. When there is no interference between an applied impact and reflected wave in a structure, effect of material impedance mismatch was significant to reduce accelerations. In other words, large structures, where waves propagate long distances before reflecting back from interfaces or the end of the structure, may be more appropriate to implement the concept of impedance mismatch to reduce acceleration responses. Therefore, mitigation of acceleration waves in structures such as buildings and bridges is considered using impedance mismatch at junctions between materials (such as steel, concrete, wood or plastic) that would exist on the path of the wave. This chapter presents numerical results of acceleration response in materially inhomogeneous and segmented long bars.

7.1 Method

7.1.1 Wave Propagation in Steel, Concrete and Wood

The same experimental long bar model discussed in chapter 4 is utilized to evaluate the shock propagation behavior of other material combinations such as steel, concrete and wood. In this study, the impact force applied in the simulations is identical to the impact force obtained from the experiments as shown in Figure 7.1. The parametric variations made to the models are the length of each segment in the rod and the material properties of the segments.

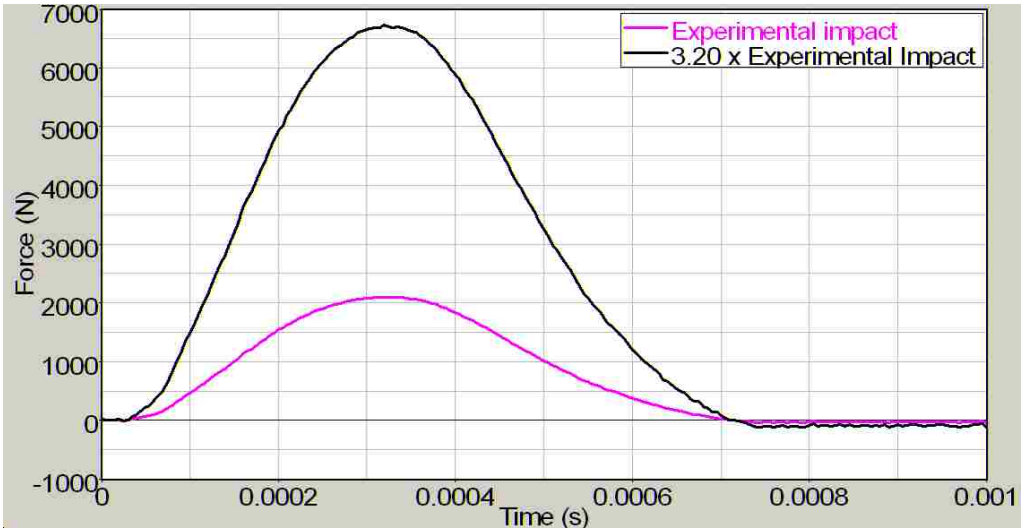

Figure 7.1 Experimentally obtained impact curve (Experimental impact) and scaled up impact curve matching the intensity of blast loading (2.69 x Experimental Impact).

First, the segmented rod simulations are conducted to evaluate the mitigation of wave propagations in the steel or the concrete structures by adding a different material. Configurations shown in Figure 7.2a and 7.2c are used to run the simulations. If steel is used for material 1, then material 2 is modeled as concrete, and vice versa. The length of material 2 in Figure 7.2c is chosen based on the ratio of a column width to a beam length, generally used in buildings.

Next, wood is inserted at the middle of either the steel or concrete rods as shown in Figure 7.2d. Generally, a soft material such as rubber can be a good damping material. Therefore, the effect of wood, which is soft compared to other common construction materials, is considered as an acceleration damper. Material properties of wood used in the simulation (Table 7.1) are selected based on the material properties of western white pine in the fiber directions as reported by Green et al. (1999). The wave propagation in

this study is considered only in axial directions. Therefore, wood is modeled as an isotropic material even though wood is an orthotropic material.

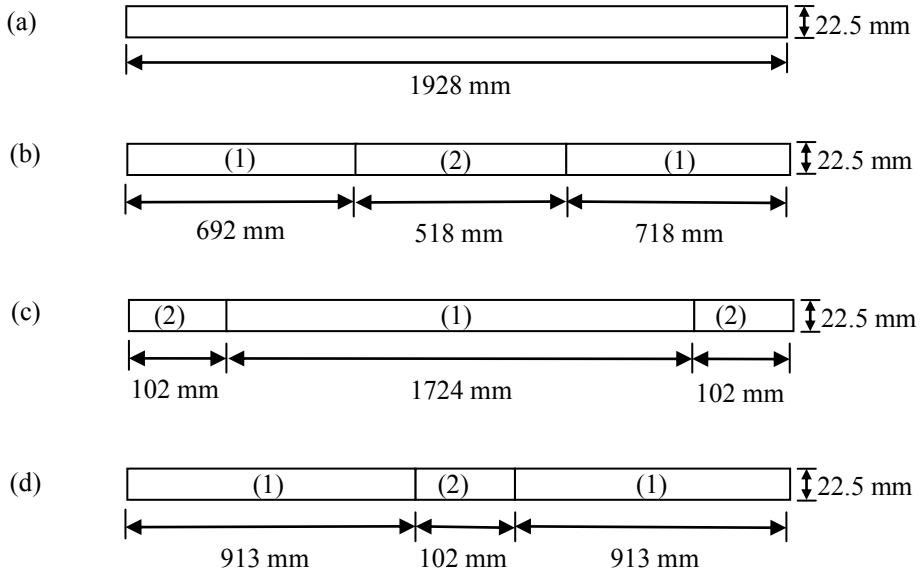

Figure 7.2 Four different configurations used in the simulations. The different numbers in parenthesis.

Table 7.1 Material Properties

	Density ρ (kg/m^3)	Young's Modulus E (GPa)	Poisson's Ratio μ	Yield Strength σ_y (MPa)	Wave Speed c (m/s)	Impedance Z (kg/m^{2}s)
Steel	7849	200	0.30	344.7	5048	3.96E+07
Concrete	2323	21.7	0.20	21.6	3056	7.10E+06
Wood	380	10.1	0.33	34.7	5155	1.96E+06

7.1.2 Comparison between the Experimental and Blast Loading

As reported by Longinow & Mniszewski (1996), the peak blast load caused by the World Trade Center Bomb at a distance of 1.52 m to building walls is approximately 16.9 MPa. The applied peak impact force obtained from the experiment is about 2,100 N which corresponds to 5.28 MPa based on the applied impact surface area of 397.6 mm^2. Therefore, the ratio of the peak pressure caused by the World Trade Center blast to the peak of the pressure caused by load curve (impulse) used in our experimental investigations is 3.20. The ratio was used in this research to augment the peaks of the experimental impulse load curve shown in Figure 7.1. The two load curves were applied to a model of configuration type b shown in Figure 7.2. In this model, material 1 is steel and material 2 is concrete

7.2 Results and Discussion

7.2.1 Wave Propagation in Steel, Concrete and Wood

When 102 mm length steel segments are placed at both ends of the concrete as shown in Figure 7.2c, significant reduction of acceleration responses are observed as shown in Figure 7.3. However, when the material order is reversed, acceleration increased compared to the rod made of one material (Figure 7.4). As shown in Table7.1, impedance of steel is higher than that of concrete. Thus, when a wave travels from a material with higher impedance to a material with lower impedance and again goes back to a material with higher impedance, the mitigation effect is observed. When a wave travels in materials with opposite placement order, no acceleration mitigation effect is observed but on the contrary the accelerations increase.

Note that when the accelerations obtained from the rod made of concrete only are compared with the ones obtained from a rod made of steel only, the rod made of steel only shows significantly less than the one made of concrete. However, the importance of this study is to obtain the design which can reduce accelerations compared to an original one material structure.

The mitigation effects are also seen in the frequency domain responses obtained from the acceleration response using FFT as shown in Figures 7.5 and 7.6. When 102 mm length steel segments are added to the end of the concrete rod, the magnitudes of peaks are significantly reduced and peaks at higher frequencies are suppressed (Figure 7.5). On the other hand, when 102 mm length concrete segments are added to the ends of the steel rod, increases in magnitudes are clearly seen in Figure 7.6. Also, strong peaks are observed in higher frequencies when concrete is added in the middle segment compared to the rod made of steel only (Figure 7.6).

As shown in Figures 7.7 and 7.8, inserting a wood segment in between two concrete or steel segments did not reduce accelerations significantly even though the impedance of wood is lower than that of steel and concrete. Wood has much lower stiffness compared to steel and concrete. However the wave speed of materials is calculated as the square root of Young's modulus divided by density. Since wood has much lower density, the wave speed of wood is 5155 m/s which is the highest among the considered materials in this study (Table 7.1). Therefore, inserting wood at the middle of a steel rod does not produce any acceleration mitigation effects. The case of a concrete rod inserting wood in the middle of the rod forces the waves to propagate from materials with lower wave speed to higher speed and back to a lower wave speed, which is found to increase the

response as discussed earlier in this paper. The mitigation effect might be observed when the wood segments are placed at the end of concrete rod. However, such condition represents a wood frame with concrete beam or slabs, which is not structurally practical.

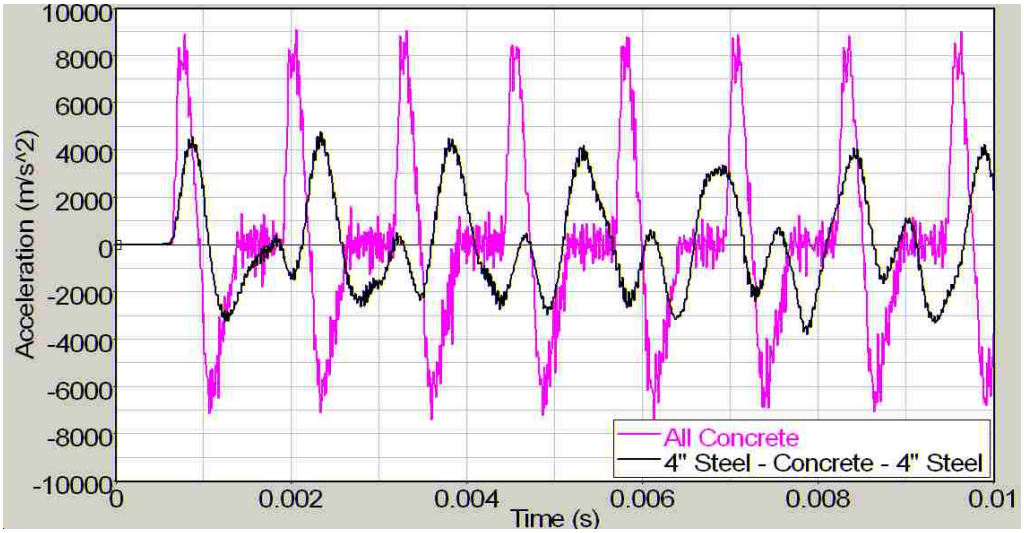

Figure 7.3 Acceleration response of segmented rods made of concrete only (All Concrete) and of steel and concrete (4" Steel – Concrete – 4" Steel), obtained from FEA without damping.

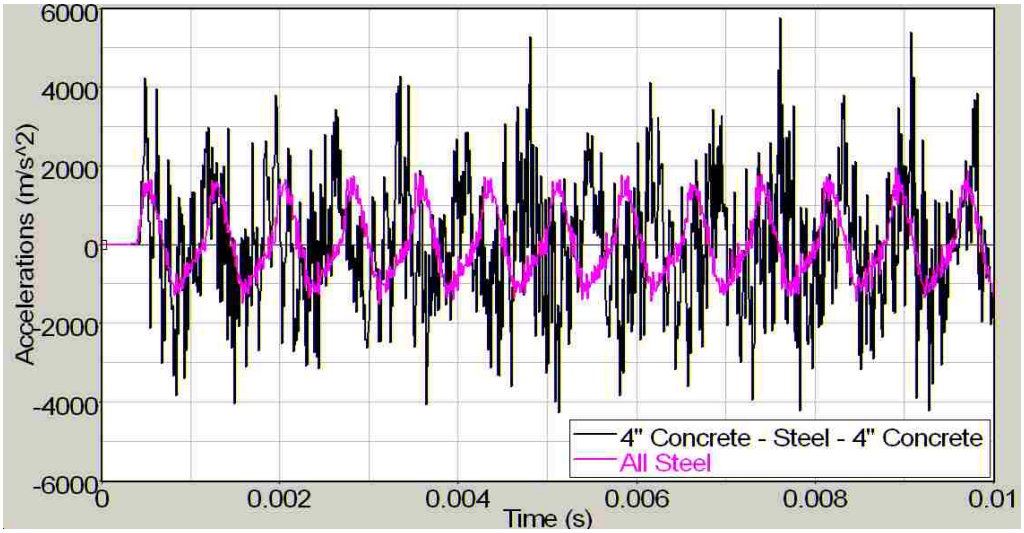

Figure 7.4 Acceleration response of segmented rods made of steel only (All steel) and of concrete and steel (4" Concrete – Steel – 4" Concrete), obtained from FEA without damping.

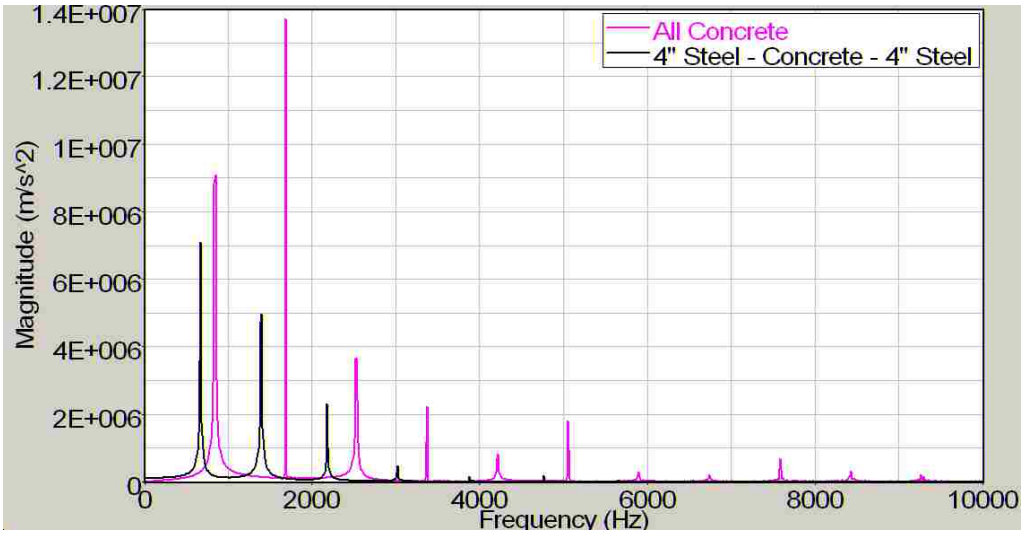

Figure 7.5 Frequency domain response spectra obtained from the acceleration responses using FFT for segmented rods made of concrete (All Concrete) and of steel and concrete (4" Steel – Concrete – 4" Steel), obtained from FEA without damping.

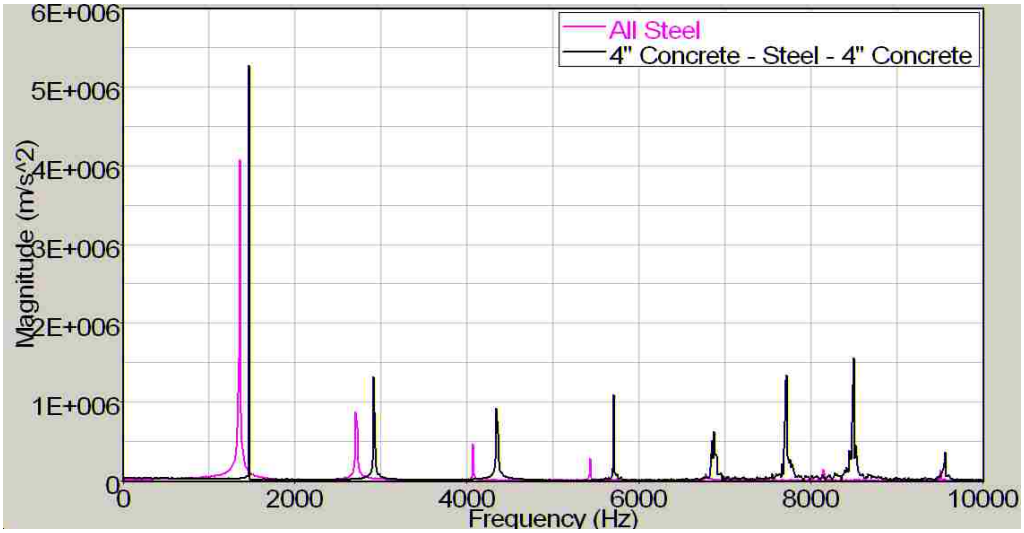

Figure 7.6 Frequency domain response spectra obtained from the acceleration responses using FFT for segmented rods made of steel (All Steel) and of concrete and steel (4" Concrete – Steel – 4" Concrete), obtained from FEA without damping.

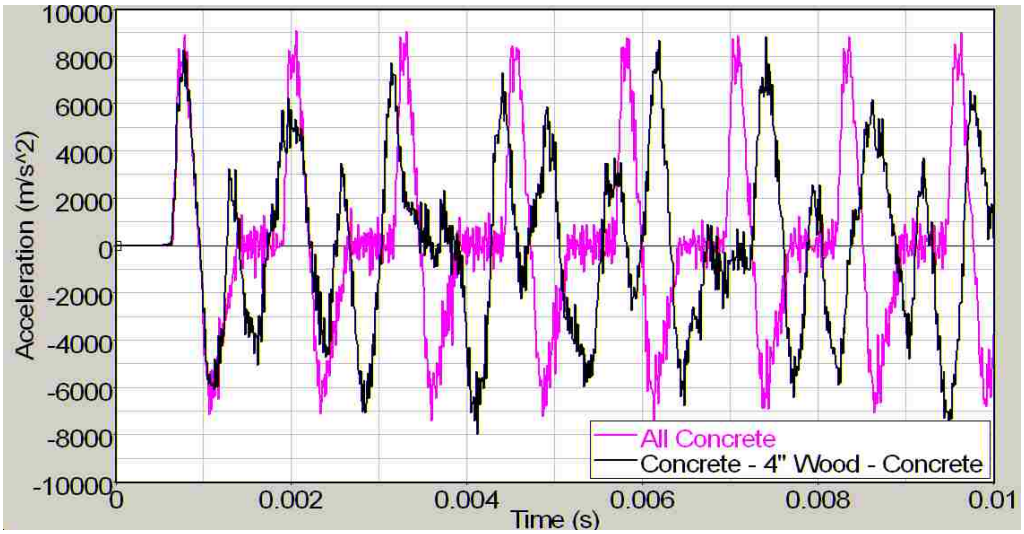

Figure 7.7 Acceleration response of segmented rods made of concrete only (All Concrete) and of concrete and wood (Concrete – 4" Wood – Concrete), obtained from FEA without damping.

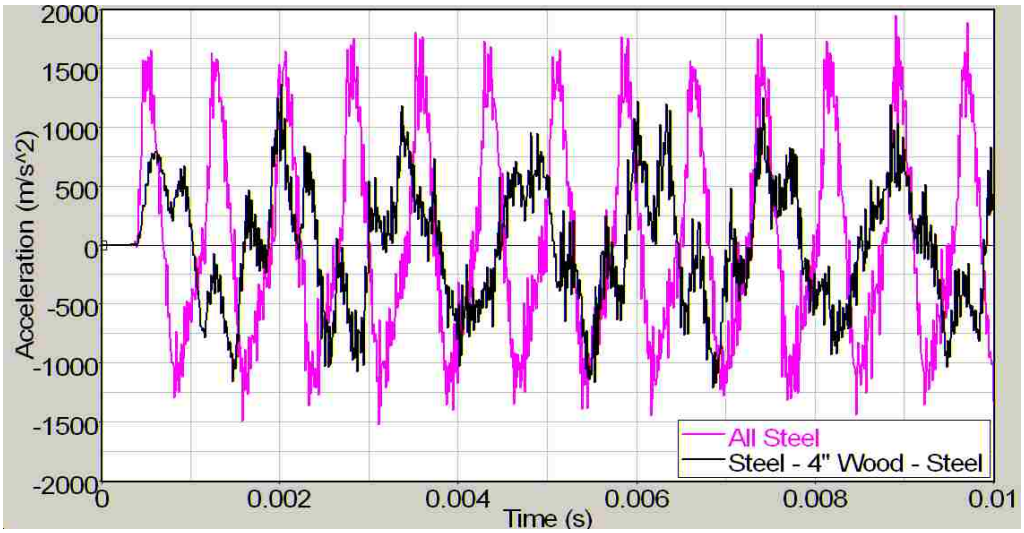

Figure 7.8 Acceleration response of segmented rods made of steel only (All Steel) and of steel and wood (Steel – 4" Wood – Steel), obtained from FEA without damping.

7.2.2 Comparison between the Experimental and Blast Loading

Figure 7.9 shows the acceleration responses obtained from two different impacts using a rod made of two 102 mm steel segments and a concrete segment. Two impact forces are used in the analysis; an impact obtained from the experiment and an impact scaled up from the experimental impact to match the intensity of blast loading obtained from Longinow and Mniszewski (1996). The maximum acceleration obtained using the experimental impact was 4,931 m/s^2 while the one using the scale up impact was 15,786 m/s^2. The ratio of accelerations from the experimental and scaled up impacts is approximately 3.2, which is same with the factor, 3.20, used to scale up the impacts. Thus the acceleration response increases linearly with the increase in the impulse load curve.

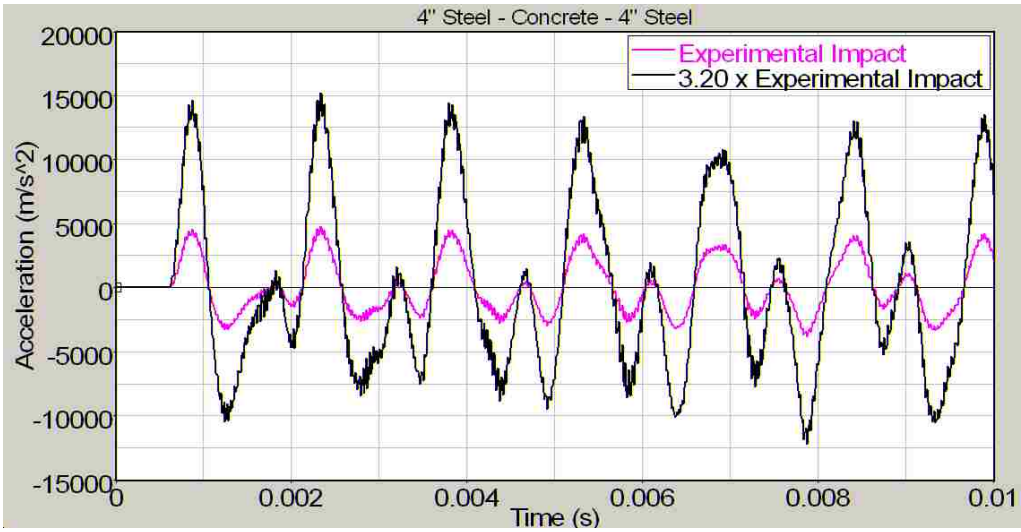

Figure 7.9 Acceleration response of a segmented rod made of steel and concrete using the experimental impulse load and an impulse whose magnitude is scaled by a factor of 2.69, obtained from FEA without damping.

7.3 Conclusion

The mitigation of accelerations in wave propagation is observed when short steel segments are added at the ends of the concrete segment. However, a material combination in the opposite order increases the accelerations in shock wave propagation. Based on these results, there is a possibility to reduce accelerations in a building using the impedance mismatch. For instance, by adding steel cover or joints at the end of concrete beam, the shock wave propagates from steel to concrete and again back to steel thus reducing its intensity.

Wood has lower Young's modulus among the common construction materials. However, its density is very low giving it a high wave speed propagation. Therefore, wood is not a practical material to use in hybrid structures for acceleration mitigation purposes.

Bibliography

Green, D. W., Winandy, J. E. & Kretschmann, D. E. (1999). Chapter 4: Mechanical properties of wood, *Wood handbook, wood as an engineering material*. Madison: U.S. Department of agriculture, forest service, forest products laboratory. Retrieved November 19, 2008, from http://www.fpl.fs.fed.us/documnts/fplgtr/fplgtr113.

Longinow, A. & Mniszewski, K. R. (1996). Protecting buildings against vehicle bomb attacks. *Practice periodical on structural design and construction* 1, 51-54.

CHAPTER 8

CONCLUSIONS

8.1 Conclusions

Mitigation of accelerations in axial direction of structures was studied using impedance mismatch concept. The studies were conducted computationally using FEA and experimentally. Results were then compared with the equations of wave propagation.

The simulation of an air-gun model in a projectile showed that mitigation of acceleration occurs when a polycarbonate layer is inserted between aluminum layers. When this material order was reversed (i.e., aluminum layer inserted between polycarbonate layers) acceleration responses were increased. When a low impedance material is inserted between high impedance materials, impedance mismatch was effective in mitigating accelerations. Excitation frequency was also lowered by using this material order (a low impedance material is inserted between high impedance materials) compared to a structure made of a high impedance material only.

Similar results were observed experimentally when long bars are used. However, when a projectile was used, acceleration increased in a projectile with a polycarbonate layer between aluminum layers unlike the air-gun model results. These results were confirmed using the FEA of experimental conditions. Based on the results, we hypothesized that interference between an applied impact and reflected wave might impede mitigation of accelerations. The hypothesis was examined using the FEA under experimental conditions using various applied impact forces. The hypothesis was also explained using equation of wave propagations. Based on the results, we concluded that it is beneficial to use the combination of high, low and high impedance materials to

attenuate wave propagation using impedance mismatch when an applied impact is short or a structure is long such that there is no interference between an applied impact and its reflected wave. If the combination of low, high and low impedance materials (e.g. polycarbonate, aluminum and polycarbonate) is compared with a structure made of a low impedance material (e.g., polycarbonate), then the combination helps to reduce wave propagation using impedance mismatch without considering the interference.

If a structure needs to have less accelerations than the structure made of aluminum only under any impact conditions, higher impedance material (than aluminum) should be inserted in between aluminum layers such as brass or steel. However, higher impedance material means higher density and/or higher Young's modulus. This might cause increase in excitation frequencies. Therefore, if interference might occur between applied impact and reflected waves, inserting a high impedance material between low impedance materials might work to reduce magnitude of acceleration but excitation frequency needs to be considered carefully.

One possible choice for low impedance material might be metal foam. As seen in the result from the air-gun simulations, inserting a metal foam layer between higher impedance materials reduced the high frequency accelerations when metal foam did not get crushed.

Impedance mismatch could be expanded to many other applications. One possibility is to use in hybrid structures. As shown in Chapter 8, when the steel was added at the end of concrete, magnitude of acceleration responses and excitation frequencies reduced.

8.2 Future Recommendations

It is recommended that future research focus on the impact surface interactions. In our study, the discrepancy in the acceleration response was observed between the hammer impact tests and the air-gun test simulations. The projectile did not show any mitigation in high frequency accelerations under the force from the impact hammer. However, the projectile of air-gun simulations by FEA showed mitigations in high frequency accelerations. The projectile experiences an impact force by crushing the honeycomb mitigator under air-gun simulations. Honeycomb is much softer than the tips of the impact hammer. Also, the impact area of the honeycomb mitigator is broader than that of the impact hammer. When the impact hammer was used with the long bars, a softer tip (the medium tip) showed better mitigations in acceleration responses compared to the hard tip in the long bars. Since the long bars have much smaller diameter compared to the projectile, the relative area between the impact hammer and the long bars are close to that of the projectile with honeycomb case. These results indicate an effect of relative hardness and stiffness of the impacting surface on the impacted object. This may explain the discrepancy between the impact hammer and the honeycomb mitigator results and might help to understand the impedance mismatch concept further.

Acceleration responses using impedance mismatch showed significant reduction when there is no interference between an applied impact and a reflected wave. If a structure is large, the possibility of interferences reduces. Therefore, it might be more suitable to implement impedance mismatch concept into larger hybrid buildings.

Throughout this study, materials are considered within the elastic region. However, research should be expanded to non-linear range to allow parts of projectiles, long bars or structures to yield out of elastic ranges.

APPENDIX

DIFFERENT TYPES OF METAL FOAM

Description of metal foams used in the referred papers.

A1. Alulight

Alulight is a closed-cell foam, originally manufactured at the Department of Powder Metallurgy of the Slovak Academy of Sciences. The composition of the cell wall material is Al-Mg0.6-Si0.3, the relative density varies from 0.16 to 0.40 and the average cell size is approximately 1mm.

A2. Duocel

The open-cell Duocel foam comprises an A16101-T6 alloy with a relative density of 0.070 and an average cell size of 1.2 mm.

A3. Cymat

Cymat is a closed-cell aluminum foam supplied by the CYMAT Corporation. The relative density rages from 0.05 to 0.20 and cell sizes change with their densities.

A4. Alporas

Alporas is a closed-cell aluminum alloy foam supplied by Shinko Wire Company Ltd., Japan. Al_4Ca and $TiAl_3$ are the precipitates in the foam. Paul and Ramamurty (2000) used a foam with a relative density in the range of 0.08 to 0.1 and average cell sizes between 4 and 5 mm. Dannemann and Lankford Jr. (2000) used a foam with relative densities of 0.074 and 0.15 and cell sizes between 4 and 7 mm. Mukai et al. (2006) used a foam with relative densities of 0.155 and 0.106 and average cell diameters between 2.37 and 3.74 mm.

A5. Hydro/Cymat

Hydro/Cymat foam is aluminum foam manufactured after the merger of Norsk Hydro and Cymat companies. Tan et al. (2005) used two different foams whose average cell sizes are approximately 4 and 14 mm with non-uniform density distribution.

Bibliography

Dannemann, K. A. and Lankford Jr., James. (2000). High strain rate compression of closed-cell aluminum foams. *Materials Science and Engineering A*, 293, 157-164.

Mukai, T., Miyoshi, T., Nakano, S., Somekawa, H. and Higashi, K. (2006). Compressive response of a closed-cell aluminum foam at high strain rate. *Scripta Materialia*, 54, 533-537.

Paul, A. and Ramamurty, U. (2000). Strain rate sensitivity of a closed-cell aluminum foam. *Materials Science and Engineering*, A281, 1-7.

Tan, P. J., Reid, S. R., Harrigan, J. J., Li, S. and Zon, Z. (2005). Dynamic compressive strength properties of aluminum foams. Part I – experimental data and observations. *Journal of the Mechanics and Physics of Solids*, 53, 2174-2205.

BIBLIOGRAPHY

Abrate, S. (1991). Impact on laminated composites materials, *Applied Mechanics Reviews*, 44, 155-190.

Abrate, S. (1994). Impact on laminated composites: Recent advances. *Applied Mechanics Reviews*, 47, 517-544.

Altair Engineering, Inc. (2004). Altair HyperWorks 7.0 [computer software]. Troy, Michigan.

Alulight International GmbH (2006). Alulight Datasheets. Retrieved November, 20, 2007, from http://www.alulight.com/en/aluminium-foam

Aoki, S. (2004). Dynamic characteristics of structure with bolted joint considering some factors. *ASME Pressure Vessels Piping Div Publ PVP* (2004 ASME/JSME Pressure Vessels and Piping Conference. San Diego, CA), 486, 143-149.

Arduino, P., Miller, G. and Ogunrinde, A. (2000). An Introduction to the theory of wave propagation in layer media, basic concepts. Retrieved at April 16, 2008 from http://gmiller.ce.washington.edu/DrLayer/theory/T-Basic-Concepts.html.

Ashby, M. F., Evans, A., Fleck, N. A., Gibson, L. J., Hutchinson, J. W. and Wadley, H. N. G.. (2000). *Metal foams: a design guide*. Oxford: Butterworth-Heinemann.

Augustaitis, V. K., Bučinskas, V. and Pauža, V. (2006). Application of Frequency Method for Defining Threaded Joint Tightening Degree. *Solid State Phenomena*, 113, 277-280.

Barker, L. M. (1971). A model for stress wave propagation in composite materials. *Journal of Composite Materials*, 5, 140-162.

Baz, A. (2006). UM-GUI: Mitigator/Bird Analysis [computer software]. University of Maryland.

Beddoe, B. (1965). Propagation of elastic stress waves in a necked rod. *Journal of Sound and Vibration*, 2, 150-166.

Berman, M. S. (2003). The effect of transient loading discretization on a roatating disk using Lawrence Livermore National Laboratories' Dyna 3-D. *Army Research Laboratory*, ARL-MR-557.

Bert, C. W. (1985). Research on dynamic behavior of composite and sandwich plates – IV. *The Shock and Vibration Digest*, 17, 3-15.

Blackstock, D. T. (2000). *Fundamentals of physical acoustics*. New York: John Wiley & Sons, Inc.

Bouland, A. and Chowdhury, M. R. (2005). Analytical Simulation and Verification of Air Gun Impact Testing. *Army Research Laboratory*, ARL-TR-3559.

Brigham, E. O. (1974). *The fast Fourier transform*. Englewood Cliffs: Prentice-Hall, Inc.

Chandra, N., Chen, X., and Rajendra, A. M. (2002). The effect of material heterogeneity on the shock response of layered systems in plate impact tests. *Journal of Composites, Technology and Research*, 24, 232-238.

Chen, P. J. and Gurtin, M. E. (1973). On the propagation of one-dimensional acceleration waves in laminated composites. *Journal of Applied Mechanics*, 40, 1055-1060.

Chiu, S. S. (1970). Difference method for multiple reflection of elastic stress waves. *Journal of Computational Physics*, 6, 17-28.

Chowdhury, M. R. and Tabiei, A. (2003). Development of an air gun simulation model using LS-DYNA. *Army Research Laboratory*, ARL-TR-3016.

Chung, D. D. L. (2001). Review: Materials for vibration damping. *Journal of Materials Science*, 36, 5733-5737.

Dannemann, K. A. and Lankford Jr., James. (2000). High strain rate compression of closed-cell aluminum foams. *Materials Science and Engineering A*, 293, 157-164.

Deshpande, V. S. and Fleck, N. A. (2000). High strain rate compressive behaviour of aluminium alloy foams. *International Journal of Impact Engineering*, 24, 277-298.

Fraser, J. W. and Gureghian, R. S. (1993). Controlling shock and vibration in electronic products. *Mechanical Engineering*, 115, 82-84.

Frost, G. W. and Costello, M. F. (2004). Control authority of a projectile equipped with an internal unbalanced part. *Army Research Laboratory*, ARL-CR-555.

Gibson, L. J. and Ashby, M. F. (1997). *Cellular solids: structure and properties* (2nd ed.). Cambridge: Cambridge University Press.

Green, D. W., Winandy, J. E. & Kretschmann, D. E. (1999). Chapter 4: Mechanical properties of wood, *Wood handbook, wood as an engineering material*. Madison: U.S. Department of agriculture, forest service, forest products laboratory. Retrieved November 19, 2008, from http://www.fpl.fs.fed.us/documnts/fplgtr/fplgtr113.

Guan, X. C., Dong, X., Guo, P. and Ou, J. P. (2006). Vibration control and magnetostrictive composite materials. *Proceedings of SPIE – the international society for optical engineering*, 6169, 61690Q1-61690Q9.

Hallquist, J. O. (Comp.). (2006). LS-DYNA Theory manual. Livermore, California.

Han, C. and Sun, C. T. (2001). Attenuation of stress wave propagation in periodically layered elastic media. *Journal of Sound and Vibration*, 243, 747-761.

Harrison, H. R. and Nettleton, T. (1997). *Advanced engineering dynamics*. New York: John Wiley & Sons, Inc.

Hexcel Corporation (1999). HexWebHoneycomb Attributes and Properties. Retrieved November, 29, 2007, from http://www.hexcel.com/Products/Downloads/Brochures

Karpanan, K. (2005). Finite Element Analysis of a projectile during gun launch. Thesis, University of Nevada, Las Vegas.

Kolsky, H. (1963). *Stress waves in solids*. New York: Dover Publications, Inc.

Li, Y., Ramesh, K. T. and Chin, E. S. C. (2001). Dynamic characterization of layered and graded structures under impulsive loading. *International Journal of Solids and Structures*, 38, 6045-6061.

Livermore Software Technology Corporation (2006). LS-DYNA [computer software]. Livermore, California.

Livermore Software Technology Corporation (2003). *LS-DYNA Keyword user's manual*, Version 970, Livermore, California.

Longinow, A. & Mniszewski, K. R. (1996). Protecting buildings against vehicle bomb attacks. *Practice periodical on structural design and construction* 1, 51-54.

Lopatnikov, S. L., Gama, B. A., Haque, M. J., Krauthauser, C. and Gillespie Jr., J. W. (2004). High-velocity plate impact of metal foams. *International Journal of Impact Engineering*, 30, 421-445.

Lu, W. and Hinnerichs, T. (2001). Crush of high density aluminum honeycombs. *Proceedings of 2001 ASME International Mechanical Engineering Congress and Exposition*, AMD-Vol. 251, New York, NY, 203-211.

Lundergan, C. D. and Drumheller, D. S. (1971). Propagation of stress waves in a laminated plate composite. *Journal of Applied Physics*, 42, 669-675.

Mukai, T., Miyoshi, T., Nakano, S., Somekawa, H. and Higashi, K. (2006). Compressive response of a closed-cell aluminum foam at high strain rate. *Scripta Materialia*, 54, 533-537.

Mukunoki, I. and Ting, T. C. T. (1980). Transient wave propagation normal to the layering of a finite layered medium. *International Journal of Solids and Structures*, 16, 239-251.

Osiński, Z. (Eds.). (1998). *Damping of vibrations*. Rotterdam, Netherlands: A. A. Balkema.

Oved, Y., Luttwak, G. E. and Rosenberg, Z. (1978). Shock wave propagation in layered composites. *Journal of Composite Materials*, 12, 84-96.

Paul, A. and Ramamurty, U. (2000). Strain rate sensitivity of a closed-cell aluminum foam. *Materials Science and Engineering*, A281, 1-7.

Rabiei, A. and O'Neill, A. T. (2005). A study on processing of a composite metal foam via casting. *Materials Science and Engineering A*, 404, 159-164.

Radford, D. D., Deshpande, V. S. and Fleck, N. A. (2005). The use of metal foam projectiles to simulate shock loading on a structure. *International Journal of Impact Engineering*, 31, 1152-1171.

Ramirez, R. W. (1985). *The FFT, fundamentals and concepts*. Englewood Cliffs, New Jersey: Tektronix, Inc.

Rao, M. D. (2003). Recent applications of viscoelastic damping for noise control in automobiles and commercial airplanes. *Journal of Sound and Vibration*, 262, 457-474.

Ruan, D., Lu, G., Chen, F. L. and Siores, E. (2002). Compressive behaviour of aluminium foams at low and medium strain rates. *Composite Structures*, 57, 331-336.

Solaroli, G., Gu, Z., Baz, A. and Ruzzene, M. (2003). Wave propagation in periodic stiffened shells: spectral finite element modeling and experiments. *Journal of Vibration and Control*, 9, 1057-1081.

Song, G., Sethi, V. and Li, H. N. (2006). Vibration control of civil structures using piezoceramic smart materials: A review. *Engineering Structures*, 28, 1513-1524.

Steinberg, D. S. (2000). *Vibration analysis for electronic equipment* (3rd ed.). New York: John Wiley & Sons, Inc.

Stronge, W. J. (2000). *Impact Mechanics*. New York: Cambridge University Press.

Szymanski, E. A. (2004). Acquiring Data for the Development of a Finite Element Model of an Airgun Launch Environment. *Army Research Laboratory*, ARL-MR-581.

Tan, P. J., Reid, S. R., Harrigan, J. J., Li, S. and Zon, Z. (2005). Dynamic compressive strength properties of aluminum foams. Part I – experimental data and observations. *Journal of the Mechanics and Physics of Solids*, 53, 2174-2205.

Tasdemirci, A., Hall, I. W. and Gama, B. A. (2004). Stress wave propagation effects in two- and three-layered composite materials. *Journal of Composite Materials*, 38, 995-1009.

Tasdemirci, A. and Hall, I. W. (2007). The effects of plastic deformation on stress wave propagation in multi-layer materials. *International Journal of Impact Engineering*, 34, 1797-1813.

Ting, T. C. T. and Mukunoki, I. (1979). A theory of viscoelastic analogy for wave propagation normal to the layering of a layered medium. *Journal of Applied Mechanics*, 46, 329-336.

Tomlinson, G. R. (2001). SD2000 state of the art review: damping. In D. J. Ewins & D. J. Inman (Eds.), *Structural dynamics @ 2000: current status and future directions* (pp. 369-388). England: Research Studies Press LTD.

Toso, M. and Baz, A. (2004). Wave propagation in periodic shells with tapered wall thickness and changing material properties. *Shock and Vibration*, 11, 411-432.

Veprik, A. M. and Babitsky, V. I. (2000). Vibration protection of sensitive electronic equipment from harsh harmonic vibration. *Journal of Sound and Vibration*, 238, 19-30.

Wasley, R. J. (1973). *Stress wave propagation in solids, an introduction*. New York: Marcel Dekker, Inc.

Wilson, M. J., Hall, R. A. and Ilg, M. (2004). ONBORD (On-board Navigation of Ballistic ORDnance): Gun-launched munitions flight controller. *Army Research Laboratory*, ARL-TR-3210.

Wu, E. and Jiang, W. (1997). Axial crush of metallic honeycombs. *International Journal of Impact Engineering*, 19, 439-456.

Zhuang, S., Ravichandran, G. and Grady, D. E. (2003). An experimental investigation of shock wave propagation in periodically layered composites. *Journal of the Mechanics and Physics of Solids*, 51, 245-265.

VITA

Graduate College
University of Nevada, Las Vegas

Sachiko Sueki

Degrees:

Bachelor of Science, Civil Engineering, 1998
Nihon University, Chiba, Japan

Master of Science, Civil Engineering, 2003
Arizona State University, Arizona

Journal Publications:

Sueki, S., Ladknay, S. G. and O'Toole, B. J. Experimental and computational study of acceleration response in layered cylindrical structures considering impedance mismatch effect (submitted in shock and vibration).

Sueki, S., Ladknay, S. G. and O'Toole, B. J. Wave Propagation in Layered Cylindrical Structures Using Finite Element and Wave Tracing (under preparation).

Refereed Publications:

Sueki, S., Ladkany, S. G., O'Toole, B. J. and Karpanan, K. (2007). Mitigation of high "g" impact vibrations in a projectile using material wave speed mismatch, In G. Kawall, S. Yu and D. Naylor (Eds.), *Proceedings of the 21st Canadian Congress of Applied Mechanics* (pp.776-777), Ontario, Canada: the CanCamCentral Committee.

Ladkany, S. G. and Sueki, S. (2009). Mitigation high acceleration shock waves in hybrid structures, In N. Ghafoori (Ed.), Proceedings of ISEC-5 (pp.333-338), Las Vegas, NV.

Conference Publications:

Sueki, S., Ladkany, S. G., Karpanan, K. and O'Toole, B. J. (2007). Material Wave Speed Mismatch for High-g Acceleration Mitigation, 78th Shock and Vibration Symposium, November, Philadelphia, PA.

Dissertation Title: Mitigation of Impact Vibrations Using Impedance Mismatch in Cylindrical Structures

Dissertation Examination Committee:

Chairperson, Samaan G. Ladkany, Ph. D.
Co-Chairperson, Brendan J. O'Toole, Ph. D.
Committee Member, Barbara Luke, Ph. D.

Committee Member, Aly Said, Ph. D.
Graduate Faculty Representative, Douglas Reynolds, Ph. D.